PETROGRAPHY AND GEOCHEMISTRY OF HYDROTHERMALLY ALTERED VOLCANIC ROCKS METAMORPHOSED AT GRANULITE-FACIES CONDITIONS: AN EXAMPLE FROM THE CENTRAL GRENVILLE PROVINCE

by

© Marisa Ann Hindemith, B.Sc.

A thesis submitted to the

School of Graduate Studies

in partial fulfillment of the requirements for the degree of

Master of Science

Department of Earth Sciences

Memorial University of Newfoundland

May 2014

St. John's Newfoundland

ABSTRACT

A layered bimodal sequence (LBS) was recently recognized in the Canyon domain in the central Grenville Province, and inferred to be the extrusive products of rift-related magmatism at ~1.25 Ga. The LBS consists of alternating felsic and mafic rocks with, locally, pre-metamorphic hydrothermally altered zones (HAZ), and were metamorphosed to mid-*P* granulite-facies conditions during the Grenvillian orogeny (~1 Ga). In the HAZ, characteristic felsic rocks are pink and white gneisses, grading into varieties of aluminous gneisses and garnetites. This thesis is a petrographic and geochemical study of these rocks, and provides new insights on the protoliths, the hydrothermal alteration, and the subsequent metamorphic overprint.

The most informative microstructures were observed in the aluminous gneisses, as for instance: (a) relics of bipyramidal quartz phenocrysts indicative of a volcanic precursor; (b) aluminous nodules, seams of sillimanite, and concordant quartz veins representing relict former pathways of hydrothermal fluid; and (c) quartz-K-feldspar-plagioclase-garnet-sillimanite-biotite mineral assemblages with textural evidence of partial melting, and consistent with a mid-*P* granulite-facies metamorphic overprint. In addition, slightly elevated contents of Mn in garnet, Zn in spinel, and Ba in biotite and K-feldspar in some rocks are consistent with hydrothermal fluid activity.

Geochemical data placed the following constraints on the protoliths: (a) in terms of immobile elements, the chemical protoliths are characterized as rhyolite/dacite to basalt/andesite, and most likely formed in an arc to rifted arc setting; (b) alteration indices (>50) and evidence in most rocks showing K-metasomatism and Na-depletion attest to hydrothermal alteration; and (c) the overall increase in contents of Al, K (with the

exception of the garnetites), immobile and trace elements suggests seafloor alteration, most common to VMS environments.

ACKNOWLEDGEMENTS

This project from the start to the final achievement of a completed thesis involved a long process of critical literature review, sample preparation, data collection, and the organization of the results prior to and while writing, over a time managed two-year period. The accomplishment of the finished draft required skills of both an independent working habit, and the guidance, constructive criticism, and support from certain individuals whom I would like to acknowledge for their help with the production of this final thesis.

First and foremost, I would like to thank my supervisor Dr. Aphrodite Indares for the much-appreciated opportunity this project granted to me, her invested time in assistance and guidance, and for the provision of additional NSERC funding towards travel expenses for data collection, short courses, and conferences. I would also like to thank my committee advisor Dr. Steve Piercey for his advice and suggestions, and editorial comments following in review of the thesis. In addition, I would like to thank Dr. Toby Rivers in the department for his academic guidance during the initial stages of the project, and editorial suggestions to earlier versions of some chapters in the thesis. Many thanks to Michael Shaffer and Robert Marr for their technical assistance during my data collection, and to the Graduate Studies (SGS) at Memorial University for providing me with annual financial support during my degree. Lastly, I would like to recognize the support of my family, close friends, and colleagues in the department for their encouragement and support of my goals and success, which gave me the focus needed in order to put the very best I could into this project, with the resulting satisfaction of a well-deserved and completed M.Sc. degree in geology.

Table of Contents

ABSTRACT ii

ACKNOWLEDGEMENTS iv

List of Tables vii

List of Figures viii

Chapter 1: INTRODUCTION 1-1
1.1 Rationale and aim of thesis 1-1
1.2 Structure of thesis 1-3

Chapter 2: VMS ENVIRONMENTS 2-1
2.1 General background 2-1
2.1.1 Geochemistry of VMS environments 2-2
2.2 Alteration zones 2-3
2.3 The effects of metamorphism in argillic-style hydrothermally altered zones 2-5
2.3.1 Metamorphic mineral assemblages in alteration zones 2-5
2.3.2 The effects of partial melting in granulite-facies VMS environments 2-6
2.4 Identification of former hydrothermally altered VMS environments in metamorphic terranes 2-7
2.4.1 La Romaine Supracrustal Belt, Grenville Province, Canada 2-8
2.4.2 Broken Hill, New South Wales, Australia 2-9

Chapter 3: GEOLOGICAL SETTING 3-1
3.1 The Grenville Province 3-1
3.2 The Manicouagan area 3-2
3.2.1 The Canyon domain 3-3
3.3 The layered bimodal sequence (LBS) 3-4
3.3.1 Hydrothermally altered zones (HAZ) of the LBS 3-5

Chapter 4: ANALYTICAL METHODS 4-1
4.1 Introduction 4-1
4.2 Optical microscopy 4-1
4.3 Scanning electron microscope – Mineral liberation analysis (SEM-MLA) 4-2
4.4 Mineral analysis by electron probe micro-analyzer (EPMA) 4-3
4.4.1 Recalculations of Mineral Analyses 4-3
4.5 Whole-rock analysis 4-4

Chapter 5: PETROGRAPHY 5-1
5.1 Introduction 5-1
5.2 Aluminous gneisses 5-1
5.2.1 Nodular Gneisses 5-1
5.2.2 Homogeneous Gneisses 5-3
5.3 White gneisses 5-4
5.4 Pink gneisses 5-6
5.5 Garnetites 5-7
5.6 Textural interpretation 5-7

5.6.1 Relict textures diagnostic of the protolith 5-8
5.6.2 Pre-metamorphic hydrothermal alteration 5-8
5.6.3 Metamorphism and partial melting 5-10

Chapter 6: MINERAL CHEMISTRY 6-1
6.1 Introduction 6-1
6.2 Garnet 6-1
6.3 Biotite 6-3
6.4 Spinel 6-3
6.5 Feldspars 6-4
6.5.1 K-feldspar 6-4
6.5.2 Plagioclase 6-5
6.6 Discussion 6-6

Chapter 7: GEOCHEMISTRY 7-1
7.1 Introduction 7-1
7.2 Major and minor/trace element composition 7-1
7.3 Protoliths 7-2
7.4 Alteration 7-3
7.4.1 Feldspar Alteration 7-3
7.4.2 Hydrothermal Alteration 7-4
7.5 Summary 7-5

Chapter 8: DISCUSSION AND CONCLUSIONS 8-1
8.1 Discussion 8-1
8.1.1 Insights from Petrography 8-1
8.1.2 Insights from Mineral Chemistry 8-2
8.1.3 Insights from Geochemistry 8-3
8.2 Conclusions 8-5

Bibliography 10

APPENDICES 20

Appendix A: EPMA analyses 20

Appendix B: SEM-MLA maps 20

Appendix C: Whole-rock analyses 20

List of Tables

Table 2.1: The lithological classification and tectonic settings of VMS deposits 2-13

Table 2.2: Geochemical signatures of mafic and felsic rocks from VMS deposits 2-14

Table 2.3: Mineral assemblages of unmetamorphosed, greenschist-, and granulite-grade alteration zones in association with VMS environments 2-14

Table 5.1: Mineral modes aquired by SEM-MLA imaging 5-12

Table 6.1: Compositional ranges of garnet in terms of Sps, Alm, Prp, And, Grs, and X(Fe^{2+}). 6-7

Table 6.2: Average compositions of garnet in terms of Sps, Alm, Prp, And, Grs, and X(Fe^{2+}). 6-7

Table 6.3: Compositional ranges of biotite in terms of X(Mg) ratios, Ti and Al^{VI}, Ba, F and Cl. 6-8

Table 6.4: Compositional ranges and averages of spinel in terms of Spl, X(Hc), Gah and X(Mag). 6-8

Table 6.5: Compositional ranges and averages of K-feldspar in terms of Or, Ab, An, Ba, and Sr. 6-9

Table 6.6: Compositional ranges, averages and zoning trends of plagioclase in terms of Or, Ab, An, Ba, and Sr. 6-10

Table 7.1: Normalized major oxides using Fe as FeO* and including ratios of X(Mg) 7-7

Table 7.2: Normalized molecular proportions (%) of major oxides using Fe as FeO* . 7-8

Table 7.3: Trace elements (in terms of ppm) 7-9

Table 7.4: Alteration Index (AI) 7-11

List of Figures

Figure 2.1: Chondrite-normalized rare-earth element (REE) patterns for felsic rocks from post-Archean VMS environments 2-15

Figure 2.2: A P-T petrogenetic grid for pelitic rocks at upper amphibolite- and granulite-facies conditions 2-16

Figure 3.1: Extension of the Grenville Province in North America 3-7

Figure 3.2: Simplified map of the Grenville Province in Canada 3-7

Figure 3.3: Simplified map of the Manicouagan area 3-8

Figure 3.4: Main rock types from the hydrothermally altered zones of the LBS 3-9

Figure 5.1: SEM-MLA mineral maps of gneisses with aluminous nodules in a quartzofeldspathic matrix 5-14

Figure 5.2: Photomicrographs of gniesses with aluminous nodules in a quartzofeldspathic matrix 5-15

Figure 5.3: SEM-MLA mineral maps of gniesses with aluminous nodules in a K-feldspar matrix 5-16

Figure 5.4: Photomicrographs of gniesses with aluminous nodules in a K-feldspar matrix 5-17

Figure 5.5: SEM-MLA mineral maps of homogeneous aluminous gneisses 5-18

Figure 5.6: Photomicrographs of homogeneous aluminous gneisses 5-19

Figure 5.7: SEM-MLA mineral maps of white gneisses 355a-11, 206a-04 and 355b1-11 5-20

Figure 5.8: SEM-MLA mineral maps of white gneisses 2163d2-11, 448-11 and A1-10-90A2 5-21

Figure 5.9: Photomicrographs of white gneisses 5-22

Figure 5.10: SEM-MLA mineral maps of pink gneisses 339b1-11 and 339b2-11 5-23

Figure 5.11: Photomicrographs of pink gneisses 339b1-11 and 339b2-11 5-24

Figure 5.12: SEM-MLA mineral maps of pink gneisses 319-1-11 and 216e-11 5-25

Figure 5.13: Photomicrographs of pink gneisses 319-1-11 and 216e-11 5-26

Figure 5.14: SEM-MLA mineral maps of garnetites 355c1-11, 355-2a-04 and 355c2-11 5-27

Figure 5.15: SEM-MLA mineral maps of garnetites 355c3-11 and 355cx-11 5-28

Figure 5.16: Photomicrographs of garnetites 5-29

Figure 5.17: Relict textures diagnostic of the protolith 5-30

Figure 5.18: Features diagnostic of pre-metamorphic hydrothermal alteration 5-31

Figure 5.19: Textures related to granulite-facies metamorphism and partial melting in the aluminous gneisses 5-32

Figure 6.1: Zoning profiles of garnets from aluminous gneisses in terms of Alm, Prp, Ca and X(Fe^{2+}) 6-11

Figure 6.2: Zoning profiles of garnet from white gneisses in terms of Alm, Prp, Ca and X(Fe^{2+}) 6-12

Figure 6.3: Zoning profiles of garnet from garnetites in terms of Alm, Prp, Ca and X(Fe^{2+}) 6-13

Figure 6.4: Ternary composition plots of garnet 6-14

Figure 6.5: Ti vs. X(Mg) composition plots of biotite 6-15

Figure 6.6: Ti vs. Al^{VI} composition plots of biotite 6-16

Figure 6.7: Ternary composition plots of spinel 6-17

Figure 6.8: Ternary Or-An-Ab composition plots of K-feldspar and plagioclase 6-18

Figure 7.1: Harker plots of major oxides plotted against SiO_2 7-12

Figure 7.2: Harker plots of major oxides plotted against X(Mg) 7-13

Figure 7.3: Ternary plots of molecular proportions of major oxides 7-14

Figure 7.4: Protoliths based on ratios of Nb/Y-Zr/TiO_2 7-15

Figure 7.5: Ratios of Nb-Zr 7-15

Figure 7.6: Y-Nb, Yb-Ta, Y+Nb-Rb and Yb+Ta-Rb ratios 7-16

Figure 7.7: Extended primitive mantle (PM) plots 7-17

Figure 7.8: Chondrite-normalized plots 7-18

Figure 7.9: Ternary AFM and A'KF diagrmas modeling alteration of the metamorphic mineral assemblage 7-19

Figure 7.10: Ternary plots of feldspar alteration 7-20

Figure 7.11: Hydrothermal alteration showing gains or losses in mobile and immobile elements 7-21

Chapter 1: INTRODUCTION

1.1 RATIONALE AND AIM OF THESIS

Volcanic-plutonic belts formed in marine settings represent first-order hosts for volcanogenic massive sulfide (VMS) deposits (Franklin *et al.* 1981; Galley 1993; Ohmoto 1996; Sillitoe *et al.* 1996; Corbett and Leach 1998; Hedenquist *et al.* 2000; Sillitoe 2000, 2003; Large *et al.* 2001; Bonnet *et al.* 2005; Bonnet and Corriveau 2007). Diagnostic features of VMS environments include the chemical, mineralogical, and textural zonations developed during metasomatic changes due to fluid-rock interaction in a submarine volcanic setting (Lydon 1988; Galley 1993, 1995; Large *et al.* 2001). Alteration types (i.e. chloritic, sericitic, argillic) are useful as exploration vectors for the detection of hydrothermally altered zones in VMS environments (Allard 1978; Gauthier *et al.* 1985; Allard and Carpenter 1988; Galley 1993; Thompson *et al.* 1997; Spry *et al.* 2000; Bonnet *et al.* 2005; Bonnet and Corriveau 2007).

During metamorphism, recrystallization driven by the changes in pressure and temperature lead to the formation of new mineral assemblages, and in the case of granulite-facies conditions, can lead to partial melting (Spear *et al.* 1999). In high-grade metamorphic terranes, these features tend to obliterate evidence of primary textures. However, a number of studies have documented that metamorphosed, hydrothermally altered VMS environments preserve, to some extent, relict features and the evidence of chemical changes the protolith has undergone prior to metamorphism (Trägårdh, 1991; Hannington *et al.* 2003; Roberts *et al.* 2003; Blein *et al*. 2004; Stanton 2004).

The Grenville Province consists of Archean to Mesoproterozoic rocks that were formed during the accretionary growth of Laurentia, and were subsequently involved in a

continental collision during the Grenvillian orogeny, *ca.* 1.09 to 0.98 Ga (Rivers 2008, 2009). In the Manicouagan area of the central Grenville Province, a recently identified ~1.25 Ga layered bimodal sequence (LBS) is inferred to represent the remnants of an ancient volcanic belt (Indares and Moukhsil 2013), evidence of which is preserved despite a Grenvillian mid-*P* granulite-facies overprint (Dunning and Indares 2010).

The LBS mainly consists of alternating layers of felsic and mafic rocks. The felsic rocks locally grade into aluminous or felsic layers with aluminous nodules, and layers of garnetite. Such lithologies can be derived from hydrothermally altered volcanic rocks (Bonnet and Corriveau 2007). The aim of the thesis is to characterize felsic and aluminous rocks inferred to represent metamorphosed equivalents of hydrothermally altered volcanic units and document:

(a) the composition and types of protoliths;

(b) the tectonic environment of formation;

(c) the degree and type of alteration(s); and

(d) the extent of the metamorphic overprint.

This is accomplished by means of a detailed petrological and geochemical investigation involving:

(i) examination of microstructures by optical microscopy and SEM-MLA mapping of polished thin sections;

(ii) documentation of mineral chemistry; and

(iii) acquisition of bulk rock major and trace element data and interpretation within the framework of relevant geochemical diagrams.

1.2 STRUCTURE OF THESIS

The thesis is organized into eight chapters. **Chapter 1**, the introductory chapter, includes the rationale aim (Section 1.1), and structure of the thesis (Section 1.2).

Chapter 2 discusses the general background of VMS environments and zones of hydrothermal alteration (Sections 2.1 to 2.5), the effects of metamorphism on hydrothermally altered zones (Section 2.6), the identification of former VMS settings in metamorphic terranes (Section 2.7), and concludes with examples of highly metamorphosed hydrothermally altered VMS environments (Section 2.8).

Chapter 3 provides a geological outline of the Grenville Province (Section 3.1), and the study area (Section 3.2), with emphasis on the layered bimodal sequence (LBS; Section 3.3).

Chapter 4 describes the analytical methods used for the study: optical microscopy (Section 4.2); scanning electron microscopy with imaging using mineral liberation analysis software (Section 4.3); mineral analysis by microprobe (Section 4.4); and whole-rock lithogeochemical analysis by fusion of whole-rock powders, followed by inductively-coupled plasma optical emission mass spectrometry (Section 4.5).

Chapter 5 focuses on the petrography of the investigated rock types from the hydrothermally altered zones (HAZ) of the LBS (aluminous gneiss: Section 5.2; white gneiss: Section 5.3; pink gneiss: Section 5.4; and garnetites: Section 5.5). This chapter concludes with a discussion of inherited features of the protoliths, features attributed to pre-metamorphic hydrothermal alteration, and textures related to the metamorphic overprint (Section 5.6).

Chapter 6 focuses on the mineral chemistry of garnet (Section 6.2), biotite (Section 6.3), spinel (Section 6.4), and feldspars (Section 6.5) from the rock types discussed in Chapter 5, and is concluded by a brief summary (Section 6.6).

Chapter 7 covers the whole-rock lithogeochemistry in terms of major and trace elements (Section 7.2), and discusses the implications of the data in terms of the type of protoliths, tectonic setting, and alteration (Sections 7.3-7.4).

The discussion (Section 8.1) and conclusions (Section 8.2) of the study are covered in **Chapter 8**, and are followed by the bibliography and appendices.

Chapter 2: VMS ENVIRONMENTS

2.1 GENERAL BACKGROUND

Volcanogenic (Franklin *et al.* 2005), also referred to as volcanic-associated (Franklin *et al.* 1981, 1995) and volcanic-hosted (Large *et al.* 2001b) massive sulfide deposits, are important global sources of Zn, Pb, Cu, Ag, and Au (Franklin *et al.* 2005; Galley *et al.* 2007; Gibson *et al.* 2007; Piercey 2010). Volcanogenic massive sulfide (VMS) deposits are the stratabound and/ or stratiform accumulations of polymetallic massive sulfides that form syngenetically at or near the seafloor in submarine volcanic environments (Lydon 1984; Galley *et al.* 2007; Gibson *et al.* 2007). The main and most exemplary components of these deposits generally consist of: (a) a massive to tabular shaped sulfide lens (>60% sulfide minerals); and (b) an underlying stockwork zone located within an envelope of altered footwall volcanic and/ or sedimentary rocks (Lydon 1984, 1988; Franklin *et al.* 2005; Galley *et al.* 2007; Gibson *et al.* 2007).

Volcanogenic massive sulfide deposits are classified in terms of their base metal content (Zn, Pb, Cu), their type-locality, and/ or their host-rock lithology (Franklin *et al.* 1981; Large 1992; Galley *et al.* 2007). According to the lithological classification first suggested by Barrie and Hannington (1999), and later modified by Franklin *et al.* (2005) and Galley *et al.* (2007), the host rock associations of VMS deposits have been divided into six groups: (i) mafic; (ii) bimodal-mafic; (iii) pelitic-mafic; (iv) bimodal-felsic; (v) siliciclastic-felsic; (vi) hybrid bimodal-felsic (Table 2.1).

Volcanogenic massive sulfide environments are most commonly developed in extensional tectonic settings, which include oceanic seafloor spreading centers, and submarine volcanic arc and backarc environments (Franklin *et al.* 1981; Barrie and

Hannington 1999; Large *et al.* 2001; Franklin *et al.* 2005; Gibson *et al.* 2007; Hannington 2009; Hannington *et al.* 2011). VMS deposits in these settings are localized within volcanic centers where high heat flow and cross-stratal permeability are focused (Franklin *et al.* 2005; Hannington *et al.* 2009).

Volcanogenic massive sulfide deposits are the product of convective hydrothermal systems formed at or near the seafloor through the focused discharge of hot, reduced, and metal-rich 'black smoker' vent fluids that mix with the cold, oxidized, and sulfate-bearing (in some cases) ambient seawater (Franklin *et al.* 1981; Lydon 1984, 1988; Hannington *et al.* 1995; Large *et al.* 2001a; Franklin *et al.* 2005; Galley *et al.* 2007). The generation of fluid circulation at spreading centers requires the presence of a heat source (i.e. magma intrusion), a permeable medium, and a fluid (seawater) that saturates the crust in order to generate and sustain a long-lived convective hydrothermal system (Hannington *et al.* 1995, 2005, 2011; Gibson *et al.* 2007; Tivey 2007; Hannington 2009).

Such a system leads to the formation of:

(a) a massive sulfide deposit at or near the seafloor;

(b) footwall and hanging wall (less common) alteration zones by the interaction of near surface strata with high-*T* ascending hydrothermal fluids and ambient seawater; and

(c) distal products (e.g. exhalites), which represent the hydrothermal contribution to background sedimentation.

2.1.1 Geochemistry of VMS environments

The primary geochemical signatures of the host rocks are critical for the understanding of the thermal, tectonic, and petrological history of VMS environments (Piercey 2009, 2010).

Juvenile VMS environments typically consist of mafic, bimodal-mafic, and mafic-siliciclastic sequences with minimal continental influence (Galley *et al.* 2007; Piercey 2009, 2010). Felsic rocks in such environments are derived from the melting of hydrated mafic crust, whereas mafic rocks are sourced from the asthenosphere (Piercey 2009, 2010). Siliciclastic-felsic and bimodal-felsic sequences are formed in evolved VMS environments, whereas felsic rocks form by the melting of continental crust or continental crust-derived rocks, and mafic rocks are sourced from the lithosphere or asthenosphere (Galley *et al.* 2007; Piercey 2009, 2010).

In post-Archean belts, juvenile felsic rocks generally have a similar trace element signature to mafic rocks, and are of tholeiitic to boninitic affinity, with low HFSE and low to flat REE contents (Fig. 2.1a; Piercey 2009, 2010, 2011). In contrast, more evolved felsic rocks have elevated HFSE and REE contents, within-plate (A-type), and peralkaline to calc-alkaline affinities (Fig. 2.1b; Piercey 2009, 2010). Characteristic geochemical signatures of mafic and felsic rocks from different groups of VMS deposits are summarized in Table 2.2.

2.2 ALTERATION ZONES

Alteration zones in VMS deposits are developed within the footwall stratigraphy, and result from a series of metasomatic fluid-rock interactions (Galley 1993). Chemical changes in the convective hydrothermal fluids involve the drawdown of seawater during recharge towards the heat source and eventual upflow into an upper recharge zone of semi-conformable alteration, which results in the remobilization of mobile elements and/or zone refinement (Galley 1993; Galley *et al.* 1995; Large *et al.* 2001; Galley *et al.* 2007). The alteration zones involve:

(a) regional (semi-conformable) alteration induced by the downwelling of fluid flow during hydrothermal recharge, and the leaching of elements and/ or metals from the permeable footwall; and

(b) discordant or pipe-like alteration with a zonation consisting of a K-rich outer zone characterized by sericite, and a Mg-rich inner zone characterized by Mg-chlorite (±quartz) proximal to the upflow of the convecting hydrothermal fluid (Lydon 1984; Stephens *et al.* 1984; Galley 1993; Galley *et al.* 2007; Piercey 2009).

Typical geochemical changes of the protoliths in alteration zones include the following: (a) variable enrichment in K_2O, with highest concentrations in the sericite-rich outer zone, and strong depletion in Na_2O; (b) Cao depletion towards the interior of the alteration zone; (c) MnO and Fe_2O_3 increase in the Mg-enriched inner zone; (d) immobile element ratios Ti/Zr-Nb/Y decreasing and Ba and Sr contents increasing towards the center of the alteration system (Large *et al.* 1992).

The majority of VMS environments are dominated by chlorite to sericite alteration zones produced by water-rock interaction under low-sulfidation conditions (Riverin and Hodgson 1980; Franklin *et al.* 1981; Lydon 1984, 1988; Sillitoe *et al.* 1996). These alteration zones are typically enriched in Si, Al, K, and Fe or Mg, and characterized by the mineral assemblage sericite, quartz, and chlorite (Table 2.3; Bonnet and Corriveau 2007).

High-sulfidation conditions result in argillic and advanced argillic alteration types, which result from the rise of highly acidic magmatic volatiles condensed into the circulating seawater (Sillitoe *et al.* 1996). These conditions are capable of extreme 'leaching' and the oxidation of SO_2 or H_2S in order to produce sulfuric acid, and are most diagnostic of shallow water epithermal-type VMS hybrid environments (Sillitoe *et al.*

1996; Galley *et al.* 2007; Shanks 2012). Argillic alteration zones are most enriched in Si and Al, and to a lesser extent K, Fe, Mg, Na and Ca, and are characterized by the mineral assemblage kaolinite, alunite, dickite, pyrophyllite, quartz, illite, smectite and sericite (Table 2.3; Bonnet and Corriveau 2007). Such hydrothermal alteration commonly leads to residual gains in Al, and, typically, Al-rich mineral assemblages in felsic rocks (e.g. sericite, Al-silicate; Galley 1993, 1995; Galley *et al.* 1995; Sillitoe *et al.* 1996; Spear *et al.* 1999; Hannington *et al.* 2003). The focus of this study deals with rocks that have been locally, hydrothermally altered to degrees of sericitic and argillic conditions prior to metamorphism.

2.3 THE EFFECTS OF METAMORPHISM IN ARGILLIC-STYLE HYDROTHERMALLY ALTERED ZONES

The metamorphism of hydrothermally altered rocks typically preserves the original chemical changes of the protolith (Trägårdh, 1991; Hannington *et al.* 2003; Roberts *et al.* 2003; Blein *et al*. 2004; Stanton 2004). Because aluminous bulk chemistries are common in such rocks, the P-T conditions of metamorphism can be assessed using petrogenetic grids designed for pelitic rocks (e.g. Spear *et al.* 1999).

2.3.1 Metamorphic mineral assemblages in alteration zones

Prior to metamorphism, VMS alteration zones mainly consist of variable proportions of sericite, illite, quartz, kaolinite, chlorite and K-feldspar (Table 2.3). With increased grade of metamorphism from greenschist- to amphibolite-facies conditions, major changes in the mineralogy include the replacement of: (a) illite and sericite by muscovite; (b) kaolinite by pyrophyllite + quartz and pyrophyllite by Al-silicate; and (c) chlorite by biotite (Table 2.3; Bonnet and Corriveau 2007). At upper amphibolite- to granulite-facies conditions, muscovite, and then biotite experience dehydration melting

by reactions such as: (a) muscovite + quartz → Al-silicate + melt + K-feldspar [R1]; and (b) biotite + Al-silicate + quartz → garnet and/ or cordierite + melt + K-feldspar ([R2]; Fig. 2.2; Spear *et al.* 1999). Therefore, the metamorphic mineral assemblage at granulite-facies conditions in zones of sericitic and argillic alteration consist of biotite, K-feldspar, garnet, and/ or cordierite, and quartz in the presence of melt, with very high proportions of Al-silicate and quartz in zones of advanced argillic alteration (Table 2.3; Bonnet and Corriveau 2007).

2.3.2 The effects of partial melting in granulite-facies VMS environments

The composition of rocks in hydrothermal alteration zones of VMS environments typically remains unchanged except if: (a) anatectic melt mobilization during partial melting under granulite-facies conditions has occurred; or (b) there is an external influx of fluids at any point in time (Bonnet and Corriveau 2007). Partial melting in aluminous rocks under granulite-facies conditions can be identified by the presence of leucosomes at the outcrop scale (Holness *et al.* 2011, and references herein), and/ or by a range of microstructures (Sawyer 1999) such as:

(a) thin films and/ or pools of feldspar enclosing corroded quartz and/ or Al-silicate and/ or biotite, and best preserved as composite inclusions in garnet. These are attributed to the biotite dehydration melting reaction ([R2]), with the corroded minerals and garnet representing relict reactant phases and a product phase respectively. The thin films and pools are inferred to represent former melt pseudomorphs (Holness *et al.* 2011); and

(b) biotite, commonly with quartz symplectite, corroding rims of garnet. This microstructure is inferred to develop during melt crystallization by [R2] in the reverse direction (Spear *et al.* 1999).

2.4 IDENTIFICATION OF FORMER HYDROTHERMALLY ALTERED VMS ENVIRONMENTS IN METAMORPHIC TERRANES

In highly metamorphosed terranes, the precursor rock types are largely transformed into gneiss complexes where deformation and metamorphic recrystallization lead to an extensive modification of their initial character (Bonnet *et al.* 2005; Bonnet and Corriveau 2007). However, despite these modifications to the original rock, recent studies have shown that hydrothermally altered rocks from VMS environments metamorphosed under high-grade conditions may preserve, to some extent, diagnostic features of the volcanic precursors and the hydrothermally altered products (Hodges and Manojlovic 1993; Barrett and MacLean 1994; Zaleski and Peterson 1995; Roberts *et al.* 2003; Bonnet and Corriveau 2003, 2005, 2007; Gifkins *et al.* 2005). For instance, relict volcanic textures such as recrystallized fiamme, lapilli- and bomb-fragments can be recognized in some cases (Bonnet *et al.* 2003, 2005; Bonnet and Corriveau 2005; Corriveau *et al.* 2003; Corriveau and Bonnet 2003, 2005, 2007). However, different processes may lead to the formation of similar rock types, and careful petrographic and geochemical studies are essential for the detection of hydrothermally altered VMS environments in gneissic terranes (Gifkins *et al.* 2005; Bonnet *et al.* 2005; Bonnet and Corriveau 2007).

As discussed in Bonnet and Corriveau (2007), diagnostic features of previous hydrothermal alteration in gneissic rocks include:

(a) an unusual abundance of aluminous and/or mafic minerals;

(b) the presence of aluminous nodules; and

(c) the presence of atypical minerals in rock types where major elements are in excess or depleted with respect to the unaltered protoliths (if known).

The following sections provide two examples of well-known high-grade metamorphic VMS environments that are relevant to this study:

(i) La Romaine Supracrustal Belt, Grenville Province, Canada; and

(ii) Broken Hill, New South Wales, Australia.

2.4.1 La Romaine Supracrustal Belt, Grenville Province, Canada

The Mesoproterozic La Romaine Supracrustal Belt belongs to the SE half of the Natashquan domain in the eastern Grenville Province, Canada (Gobeil *et al.* 2003; Bonnet *et al.* 2005; van Breemen and Corriveau 2005). This belt mainly consists of a volcaniclastic felsic to intermediate sequence that was metamorphosed and deformed under granulite-facies conditions during the Grenvillian orogeny (Bonnet *et al.* 2005; Bonnet and Corriveau 2003; Corriveau *et al.* 2003; Corriveau and Bonnet 2005;).

The alteration zones of La Romaine recognized by Bonnet *et al.* (2005) consist of:

(a) quartzofeldspathic pink gneiss with aluminous nodules and dismembered quartz veins. These rocks are strongly enriched in K and Fe, and depleted in Ca, Na, and Mg, consistent with sericitic alteration distal from the volcanic center;

(b) migmatized aluminous biotite-sillimanite-garnet gneiss locally preserving lapilli- and bomb-sized fragments that attest to a pyroclastic origin. These rocks are depleted in alkalis and enriched in Al and Si, consistent with argillic to advanced argillic alteration; and

(c) quartz-cordierite gneisses in close proximity to the pyroclastic unit. These rocks have unusually high Si, Al, and Ba contents, and are depleted in Ca, Fe, Mg and Na, consistent with silicic alteration.

The metamorphic mineral assemblage of the aluminous gneisses from La Romaine consists of variable proportions of biotite, cordierite, garnet, K-feldspar, plagioclase,

quartz, and abundant sillimanite forming lenticular clusters or inclusion trains within garnet (Bonnet *et al.* 2005). Incipient in situ partial melting in these rocks is suggested by the presence of leucosomes, which are generally scarce and disconnected (Bonnet *et al.* 2005).

The geochemical signatures of the altered metavolcanic rocks in terms of the relatively immobile elements Ti, Al, and Nb, are consistent with a rhyolite/dacite to andesite/basalt composition and have calc-alkaline arc affinities (Bonnet *et al.* 2005). Chondrite-normalized rare-earth element (REE) patterns show profiles with moderate enrichment in light REE (LREE), relatively flat heavy REE (HREE), and negative Eu anomalies. In contrast, quartz-cordierite gneisses have a U-shaped profile due to the relative depletion in middle and heavy REE (MREE and HREE), and a weak positive Eu anomaly. The negative Eu anomalies, common in rocks with low Na_2O and CaO (ex. nodular quartzofeldspathic gneisses) were attributed to dissolution of plagioclase (Bonnet *et al.* 2005). In addition, MREE and HREE were interpreted to have been extremely mobile in alteration zones due to the interaction with acidic fluids (sericitic, argillic and silicic alterations; Galley 1993; Sillitoe *et al.* 1996; Large *et al.* 2001; Bonnet *et al.* 2005).

2.4.2 Broken Hill, New South Wales, Australia

The Broken Hill Pb-Zn-Ag deposit occurs in the Palaeoproterozoic to Mesoproterozic Purnamoota Subgroup within the Willyama Complex of the Curnamona Craton in western New South Wales, Australia (Willis *et al.* 1983; Pilmer 2006; Spry *et al.* 2007). The Broken Hill complex consist of metapelite, amphibolite, felsic gneiss, garnet-plagioclase 'Potosi' gneiss, quartzitic gneiss, and its most diagnostic lode horizon unit containing garnetites (Johnson and Klinger 1975; Barnes *et al.* 1983; Spry and Wonder 1989). This complex was metamorphosed at ~1700 Ma up to granulite-facies

conditions, and the Pb-Zn-Ag orebodies occur in granulite-facies rock (Pidgeon 1967; Shaw 1968). The Broken Hill complex is interpreted to have formed within an epicontinental basin or an intracontinental rift, but the origin of the deposit is still uncertain (Parr and Pilmer 1993; Page *et al.* 2005a).

2.4.2.1 The Garnetites of Broken Hill

The garnetite rocks recognized at Broken Hill are classified as garnetite and quartz-garnetite (with 10-80% garnet and, locally bluish quartz and gahnite), with massive to laminated varieties (Johnson and Klingner 1975; Spry and Wonder 1989; Spry *et al.* 2000; Pilmer 2006; Spry *et al.* 2007). In addition, a third textural type, known as the 'garnet envelope' occurs on the margins of the Pb-rich orebodies (Spry and Wonder 1989; Spry *et al.* 2007).

Garnet composition of garnetite rocks described by Spry and Wonder (1989), is typically Fe+Mg-rich except for in quartz-gahnite garnetite, in which garnet is Mn-rich. Overgrowths of garnet enriched in Mn±Ca are spatially associated with the garnet envelope and attributed to a retrograde metamorphic event. Ratios of Mn/Fe in garnet increase from the footwall to hanging wall, and are interpreted to reflect a gradient of Mn across the deposit (Hawkins 1968; Pilmer 1979), the origin of which is poorly understood. The increase of Mn/Fe ratios in garnet suggests an overall increase in oxygen fugacity during deposition that resulted from ore-forming fluid when mixed with seawater (Spry and Wonder 1989). Garnetites, generally manganoan (Mn+Ca), are typically found in association with the metamorphosed orebodies in the area (Stanton 1976; Barnes *et al.* 1983; Spry and Wonder 1989). Mn-rich garnets at Broken Hill are suggested to have formed by precipitation from cooler and more oxidized hydrothermal

fluids (Heimann *et al.* 2011). In addition, garnetites with increasing amounts of Mn in garnet exhibit a decrease in grain size with proximity to the orebodies (Spry *et al.* 2007).

The chondrite-normalized REE profiles of the garnetites at Broken Hill are enriched in LREE, exhibit variable HREE, and have negative or positive Eu anomalies (Spry *et al.* 2007). The positive Eu anomalies were inferred to represent increased substitution of Eu into Mn- and Mn-Ca-rich oxides (or carbonates) in the protolith, whereas the negative anomalies were attributed to a Fe-rich, Mn-poor precursor (Heimann *et al.* 2011). The overall REE patterns are suggestive of a precursor being either a Mn-rich sediment of exhalative origin or a hydrothermally altered sediment at or near the seafloor (Schwandt *et al.* 1993; Spry *et al.* 2007). In addition, positive Eu anomalies for manganoan garnet in garnetite rocks of the Broken Hill Pb-Zn-Ag deposit are recognized as potential guides in the exploration of massive sulfide deposits, and considered possible vectors to detecting the presence of mineralization (Spry and Wonder 1989).

2.4.2.2 The Hores Gneiss

Surrounding the Broken Hill Pb-Zn-Ag deposit, the locally well-known 'Potosi' Hores Gneiss consists of a medium-grained quartz-plagioclase-K-feldspar-biotite-garnet rock with relict quartz phenocrysts attesting to a volcanic origin (Stevens and Barron 2002; Page *et al.* 2005a).

These relict phenocrysts occur as partly recrystallized and resorbed bipyramidal quartz within a fine-grained matrix, and are mainly preserved in the amphibolite-facies portion of the gneiss (Laing *et al.* 1984; Page and Laing 1992; Laing 1996; Steven and Barron 2002). The contrast between grain size of the matrix and the size of the phenocrysts decreases with increasing intensity in metamorphism (Page and Laing 1992).

However, quartz phenocrysts of the Hores Gneiss are still recognizable at the boundary with the granulite-facies, as large quartz aggregates with an overall bipyramidal shape (Stevens and Barron 2002). In addition, flattened biotite aggregates in the Hores Gneiss are inferred to have formed after altered volcanic fiamme or lapilli (Page and Laing 1992; Laing 1996).

Table 2.1: The lithological classification and tectonic settings of VMS deposits (modified after Barrie and Hannington 1999; Franklin *et al.* 2005; Galley *et al.* 2007).

Six-Fold Grouping of VMS deposits

Group:	Lithological unit	Tectonic Setting
Mafic	mafic dominated, ophiolite-type assemblages	mature intra-oceanic backarc, some transform fault related (oceanic mature backarc)
Bimodal-Mafic	basalt dominant and up to 25% felsic volcanic strata (latter often hosting deposit)	incipient-rifted bimodal volcanic arcs above intra-oceanic subduction
Pelitic-mafic	pelite dominant or subequal proportions of mafic and siliciclastic rocks (mafic/ ultramatic intrusive rocks common; minor felsic rocks)	mature basalt-pelite backarc successions in juvenile and accreted arc assemblages (oceanic mature backarc)
Bimodal-felsic	bimodal sequences of felsic volcanic rocks (35-70%), basalt (20-50%), and terrigeneous sedimentary strata (~10%)	continental margin arcs and related backarc
Siliciclastic-felsic	siliciclastic dominated (~80%), typically shale-rich with abundant felsic rocks, and <10% mafic rocks	mature epicontiental backarcs
Hybrid bimodal-felsic	felsic volcaniclastic and siliciclastic rocks	normal VMS setting with a shallow-water epithermal environment

Table 2.2: Characteristic geochemical signatures of mafic and felsic rocks from VMS deposits (modified after Piercey 2009).

Geochemisty of mafic and felsic rocks from VMS deposit groups

Group:	Mafic	Felsic
Mafic	Boninite, low Ti-tholeiite, MORB	-
Bimodal-Mafic	MORB, boninite, low Ti-tholeiite (calc-alkalic and island arc tholeiite rarer)	Boninitic rhyolite
Pelitic-mafic	MORB, alkalic, boninite (rare)	-
Bimodal-felsic	MORB, alkalic	HFSE-enriched rhyolite (A-type), peralkaline, and calc-alkalic rhyolite (rarer)
Siliciclastic-felsic	MORB, alkalic	HFSE-enriched rhyolite, peralkaline, and calc-alkalic rhyolite (rarer)

Table 2.3: The diagnostic mineral assemblages of unmetamorphosed, greenschist-, and granulite-grade alteration zones in association with VMS environments (modified after Bonnet and Corriveau 2007; Shanks 2012).

Alteration type:	Chloritic	Sericitic	Argillic	Advanced Argillic
Diagnostic minerals: unmetamorphosed	Chlorite, opal, quartz, sericite	Sericite, illite, opal	Sericite, illite, smectite, pyrophyllite, opal	Kaolinite, alunite, opal, smectite
Diagnostic minerals: greenschist facies	Chlorite, Quartz, Sericite	Muscovite, quartz	Muscovite-pyrophyllite, muscovite-Al-silicate	Kaolinite, pyrophyllite, Al-silicate, corundum, topaz
Diagnostic minerals: granulite facies	Corderite, orthopyroxene, orthoamphibole, phlogopite, Al-silicate	Biotite, K-feldspar, Al-silicate, quartz, cordierite, garnet	Sillimanite, Al-silicate, quartz, biotite, cordierite, garnet	Al-silicate, quartz
Diagnostic composition	Fe_2O_3, MgO, $\pm Al_2O_3$, $\pm SiO_2$	K_2O, Al_2O_3, Fe_2O_3, $\pm$MgO, $\pm SiO_2$	Al_2O_3, SiO_2, K_2O, Fe_2O_3, MgO	Al_2O_3, SiO_2
Similar rocks (at granulite facies)	Metapelite	Metapelite	Metapelite	Metalaterite

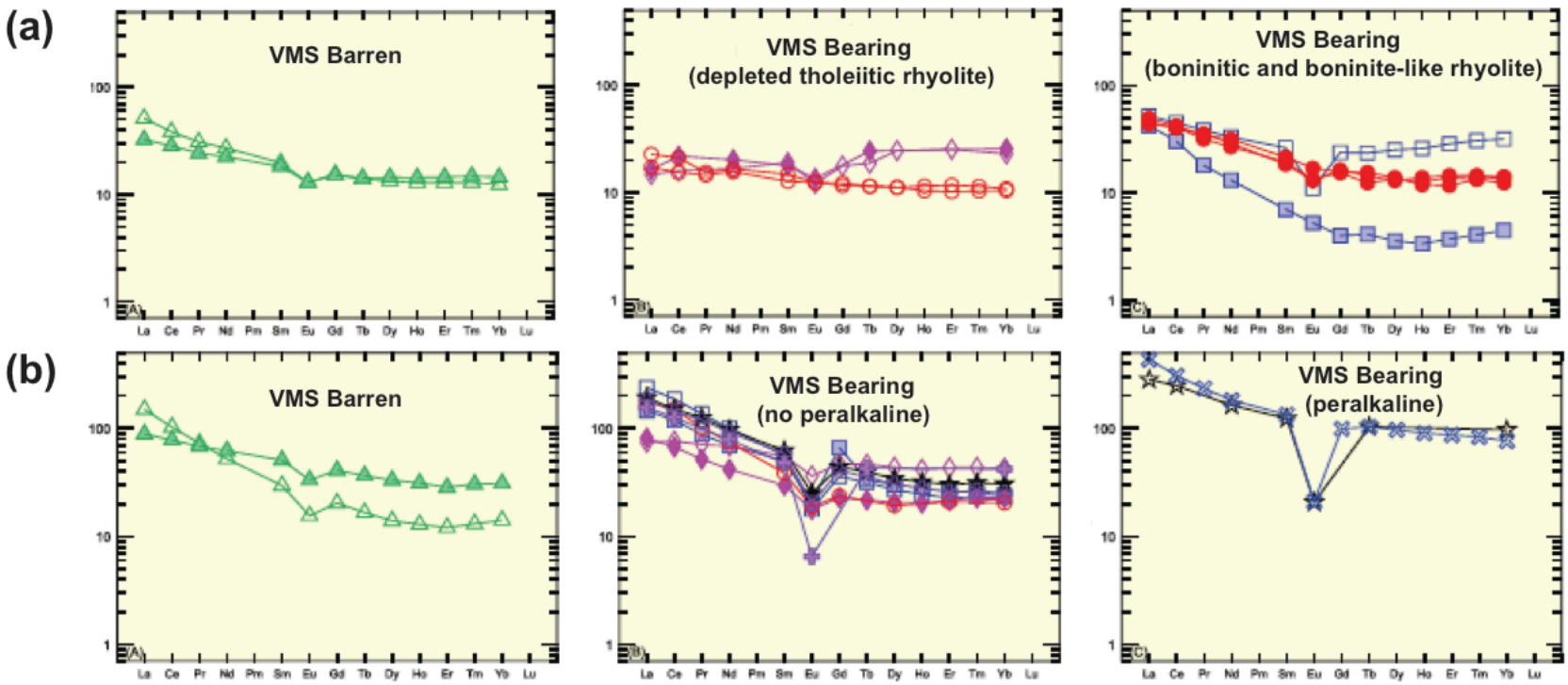

Figure 2.1: Chondrite-normalized rare-earth element (REE) patterns (from Sun and McDonough 1989) of felsic rocks from post-Archean VMS environments. **(a)** Juvenile signatures of tholeiitic to boninitic affinities with low HFSE and low to flat REE contents; and **(b)** evolved signatures with elevated HFSE and REE contents, within-plate (A-type), and peralkaline to calc-alkaline affinities (modified after Piercey 2010).

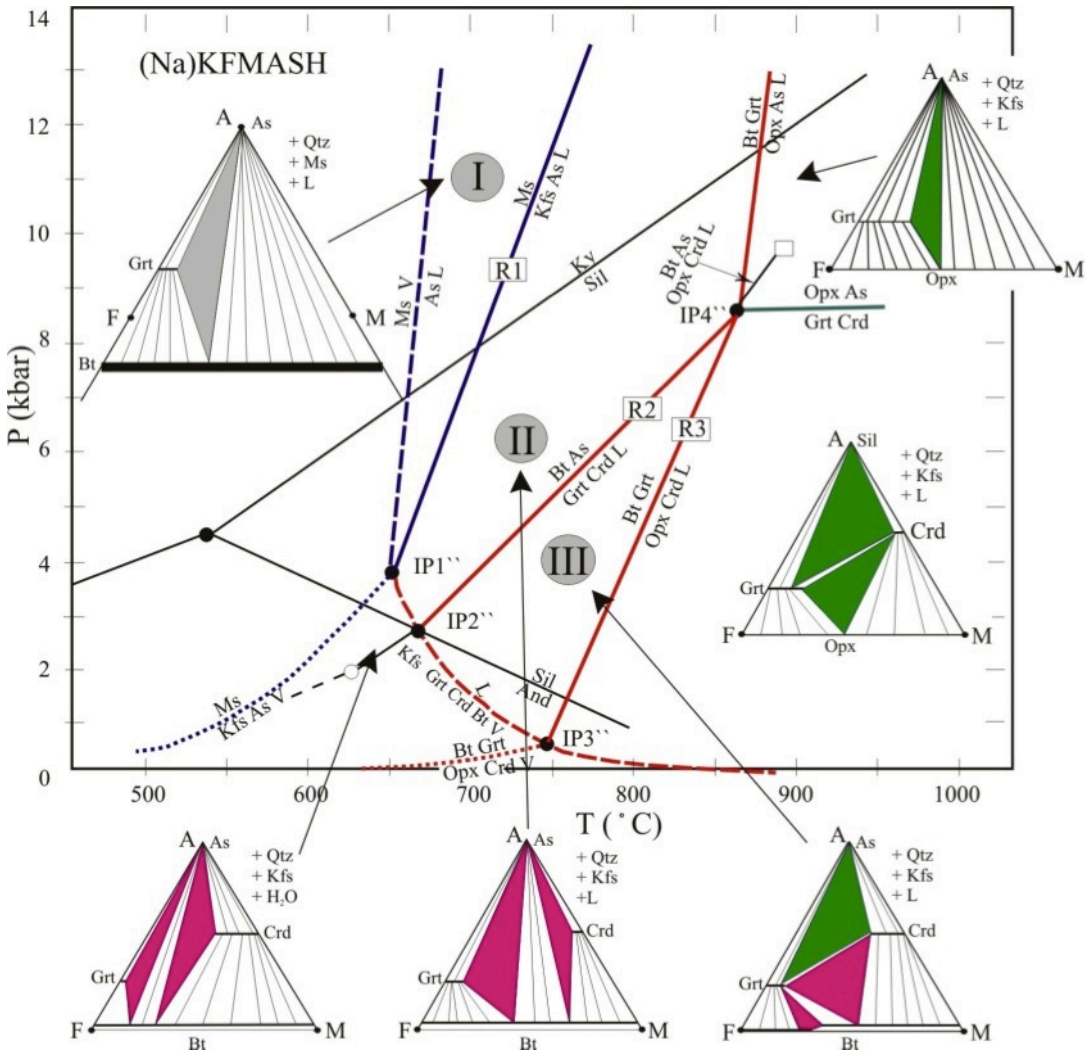

Figure 2.2: A P-T petrogenetic grid for pelitic rocks at upper amphibolite- and granulite-facies conditions (modified after Spear *et al.* 1999).

Chapter 3: GEOLOGICAL SETTING

3.1 THE GRENVILLE PROVINCE

The Grenville Province covers a nearly one million square kilometer region extending across North America (Fig. 3.1; Moore 1986). It represents a late Mesoproterozoic to early Neoproterozoic Himalayan-scale continental collisional orogen active from *ca.* 1.09 to 0.98 Ga (Rivers 2008), and built upon arc systems that formed along the margin of Laurentia between 1.7 and 1.3 Ga (Rivers 1997, 2009).

First order tectonic divisions of the Grenville Province into belts proposed by Rivers *et al.* (1989) and Rivers (2008), provide a general framework of the architecture and metamorphic characteristics of the orogen. The Parautochthonous Belt (Fig. 3.2; Rivers *et al.* 1989) is the lowest structural component, and is bounded by the Grenville Front separating the province from its foreland. The units of the Parautochthonous Belt were imbricated and metamorphosed under greenschist- to high-*P* granulite to eclogite (Rivers *et al.* 1989) during the final stages of the Grenvillian orogeny (1000-980 Ma; Rivers *et al.* 2002; Rivers 2008).

The structurally overlying units towards the southeast are collectively referred to as the Allochthonous Belt (Fig. 3.2; Rivers *et al.* 1989) or hinterland (Dunning and Indares 2010). Large areas of the hinterland were metamorphosed under mid-*P* (locally high-*P*) granulite-facies conditions, *ca.* 1.08-1.04 Ga (Rivers 2008). However, some parts of the hinterland lack evidence of Grenvillian metamorphic overprint, and are inferred to have remained at high structural levels during the Grenvillian orogeny forming an orogenic lid (Rivers 2008). The current juxtaposition of formerly deep and hot crust

with these high structural levels is inferred to be the result of the collapse of an ancient orogenic plateau (Rivers 2012).

3.2 THE MANICOUAGAN AREA

Located in the hinterland of the central Grenville Province, the Manicouagan Reservoir is marked by a Triassic age impact crater (Fig. 3.2; Hodych and Dunning 1992). In this area, the orogenic architecture is particularly well exposed along the shores of the reservoir (Hynes *et al.* 2000; Indares and Dunning 2004). The Manicouagan area (Fig. 3.3), is made-up of Parautochthonous Archean and Palaeoproterozoic units of the Gagnon terrane (GT) to the NW (van Gool *et al.* 2008) that are structurally overlain by Mesoproterozoic units of the hinterland to the SE. These units mainly consist of: (a) Labradorian (1.7-1.6 Ga) anorthosite suites of the Manicouagan Imbricate Zone (MIZ) and gabbroic rocks of the Island domain; (b) 1.5-1.4 Ga orthogneisses and paragneisses of the Hart Jaune terrane (HJT) and Canyon domain (Gobeil *et al.* 1997a & b; Indares *et al.* 2000; Indares and Dunning 2004; Dunning and Indares 2010); and (c) 1.3-1.2 Ga rocks that are recognized in the southern MIZ, the Canyon domain, and the Banded Complex (Indares and Dunning 2004; Dunning and Indares 2010; Valverde Cardenas *et al.* 2012). In addition, anorthosites (Tétépisca and Berthé; Moukhsil *et al.* 2013) and Grenvillian age granites (~1.06 Ga) are locally exposed (Fig. 3.3; Indares and Moukhsil 2013)

During the Grenvillian orogeny, the hinterland units in the Manicouagan area were metamorphosed at granulite-facies conditions under contrasting pressure regimes with high-*P* in the north (*ca.* 1.05-1.03 Ga; Indares *et al.* 2008) and mid-*P* in the south (*ca.* 1.08-1.04 Ga; Dunning and Indares 2010). In addition, the HJT (Rivers *et al.* 1989)

lacks evidence of Grenvillian age deformation and metamorphism and forms part of the orogenic lid (Hynes *et al.* 2000; Indares and Dunning 2004).

3.2.1 The Canyon domain

The Canyon domain (CD), first defined by Hynes *et al.* (2000), lies structurally above Labradorian age (~1650-1690 Ma) crustal packages of the MIZ and Island domain, and is exposed mainly in the southern part of the reservoir between the Tétépisca and Berthé anorthosites (Fig. 3.3; Indares and Moukhsil 2013). The CD mainly consists of four sets of layered mafic and quartzofeldspathic units (Indares and Moukhsil 2013; Moukhsil *et al.* 2013), all of which were metamorphosed under mid-*P* granulite-facies conditions during the Grenvillian orogeny between 1080 and 1040 Ma (Dunning and Indares 2010). This metamorphism is manifested by hornblende-plagioclase-garnet-orthopyroxene-clinopyroxene-quartz mineral assemblages in mafic rocks, and biotite-sillimanite-plagioclase-garnet-quartz-K-feldspar in the more felsic and aluminous rocks (Dunning and Indares 2010Indares and Moukhsil 2013; Lasalle *et al.* 2014).

The oldest set of layered units, exposed in the southern part of the domain, is a metasedimentary sequence of quartzofeldspathic rocks, garnet-sillimanite-bearing anatectic metapelite, quartzite, marble and calcsilicate rocks (Indares and Moukhsil 2013). This sequence is part of the Complexe de la Plus Value (PLV; Fig. 3.3) defined by Moukhsil *et al.* (2012) farther east, and is inferred to have been deposited ~1.5 Ga (Lasalle *et al.* 2013; Moukhsil *et al.* 2013). In the Canyon domain, the PLV is commonly characterized by locally abundant, transposed felsic pegmatite (Indares and Moukhsil 2013).

The second set of layered units is a layered mafic suite (LMS; Fig. 3.3**),** exposed in a large part of the central/ northern portion of the domain. This unit consists of rocks

of mafic to intermediate composition with prominent to vague compositional layering (Indares and Moukhsil 2013), that was dated at 1410±16 Ma (Dunning and Indares 2010). The rocks of the LMS are pervasively recrystallized into granoblastic hornblende-plagioclase-garnet-orthopyroxene-clinopyroxene assemblages (Indares and Moukhsil 2013). Where layering is prominent, it is discontinuous and reminiscent of an original rather than tectonic feature. In such instances, the rocks are massive and lack relict plutonic textures consistent with a supracrustal origin, or with emplacement of a layered intrusion at shallow depth (Indares and Moukhsil 2013). However, in other exposures, the rocks display a homogeneous distribution of elongate mm- to cm-scale ferromagnesian or plagioclase aggregates, which is suggestive of a coarse-grained plutonic protolith (Indares and Moukhsil 2013).

The third set of layered units locally in contact with the LMS is a quartzofeldspathic unit (QFU; Fig. 3.3), which consists of massive white to grey centimeter to decimeter scale layers with variable proportions of quartz and feldspars, traces of biotite, and rare mafic sheets. The systematic compositional layering of the QFU is suggestive of a supracrustal origin; however, the age and affiliation of this unit remains speculative (Indares and Moukhsil 2013).

The youngest and last set of layered units is a layered bimodal sequence (LBS; Indares and Moukhsil 2013), which will be discussed in detail below and is the focus of this study.

3.3 THE LAYERED BIMODAL SEQUENCE (LBS)

Discontinuously exposed in the central/northern parts of the Canyon domain (Fig. 3.3) and amongst the LMS and QFU, the LBS mainly consists of alternating mafic and

felsic layers up to a few meters thick (Fig. 3.4a) first described in Indares and Moukhsil (2013). The mafic layers are heterogeneous, commonly preserve internal cm-scale compositional layering, and are pervasively recrystallized into Hb-plagioclase±garnet±orthopyroxene±clinopyroxene±biotite±quartz mineral assemblages. Felsic layers of the LBS mainly consist of fine grained quartz an feldspars, and are of two types: (i) massive pink layers typically free of ferromagnesian minerals; and (ii) white layers with a 'bleached' appearance and commonly displaying fine compositional layering. In addition, the white gneisses locally grade into homogeneous and nodular aluminous gneiss with biotite-sillimanite-plagioclase-garnet-quartz-K-feldspar mineral assemblages, and/ or garnetite.

This felsic-mafic association of the LBS is interpreted to represent a metamorphosed sequence of ~1.25 Ga dominantly volcanic rocks, emplaced in a crustal extension setting (Indares and Moukhsil 2013; Lasalle *et al.* 2013; Valverde Cardenas *et al.* 2012). In addition, the presence of garnetite and white gneiss with aluminous nodules is suggestive of hydrothermal alteration (Bonnet and Corriveau 2007). Therefore, the LBS is interpreted to represent the remnants of an ancient volcanic belt, parts of which experienced hydrothermal alteration prior to metamorphism (Indares and Moukhsil 2013).

This study focuses on the felsic and aluminous rocks from the hydrothermally altered zones (HAZ) of the LBS (with the exception of 448-11 taken from the PLV). Outcrop-scale characteristics of the HAZ in the LBS are discussed in the section below.

3.4 HYDROTHERMALLY ALTERED ROCKS OF THE LBS

Samples from the hydrothermally altered zones (HAZ) of the LBS (locations A to D in Fig. 3.3) were collected during the 2003-04 and 2011 field seasons by Aphrodite

Indares. In all locations, felsic gneisses are variably intercalated with mafic gneisses, but the former contribute to the dominant lithology and focus of study.

The main felsic lithology in location A represents a range of white to grey felsic gneisses. Rocks are generally very leucocratic and homogeneous, and locally contain aluminous nodules distributed in centimetric layers containing concordant quartz veins (Fig. 3.4b), or grade into garnetite (Fig. 3.4c). Felsic gneisses in location B are rock types of white to pink varieties. The pink gneisses are entirely leucocratic forming a few meter thick layers, and usually contain round quartz-rich concretions surrounded by a hematized zone (Fig. 3.4d). In addition, some homogeneous layers contain specks of hornblende or thin elongated biotite clusters (Fig. 3.4e). White gneisses from location B form centimetric layers interleaved with mafic gneisses, and/or thicker layers grading into a variety with aluminous nodules, sillimanite seams, and concordant quartz veins (Fig. 3.4f). In addition, several meters thick of homogeneous aluminous layers are spotted with garnet porphyroblasts (Fig. 3.4g). Felsic rocks from location C are mainly white gneisses grading into garnet-bearing varieties, gneiss with aluminous nodules, and homogeneous aluminous gneiss (Fig. 3.4h). In the north, location D is part of the islands in the Gabriel Bay (eastern side of the Manicouagan reservoir). These rocks are made up of a complex association of white gneiss, aluminous nodular gneiss, and garnetite. In addition, one white gneiss (448-11) that was found in the metasedimentary layers of the PLV is also included in this study.

Figure 3.1: Exposed Grenville Province (red box) and its subsurface extension in North America (modified after Tollo *et al.* 2004).

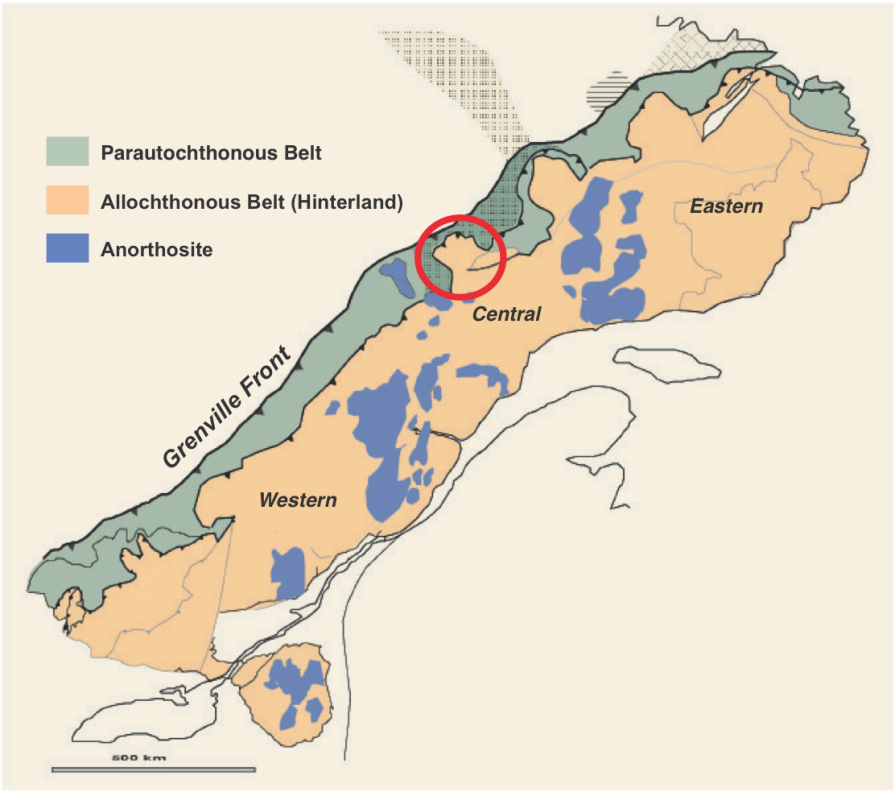

Figure 3.2: Simplified map of the Grenville Province (Canada and NE USA), highlighting the first order tectonic division into Parautochthonous and Allochthonous belts and major anorthosite complexes, with location of the Manicouagan Reservoir area (red circle; modified after Dunning and Indares 2010).

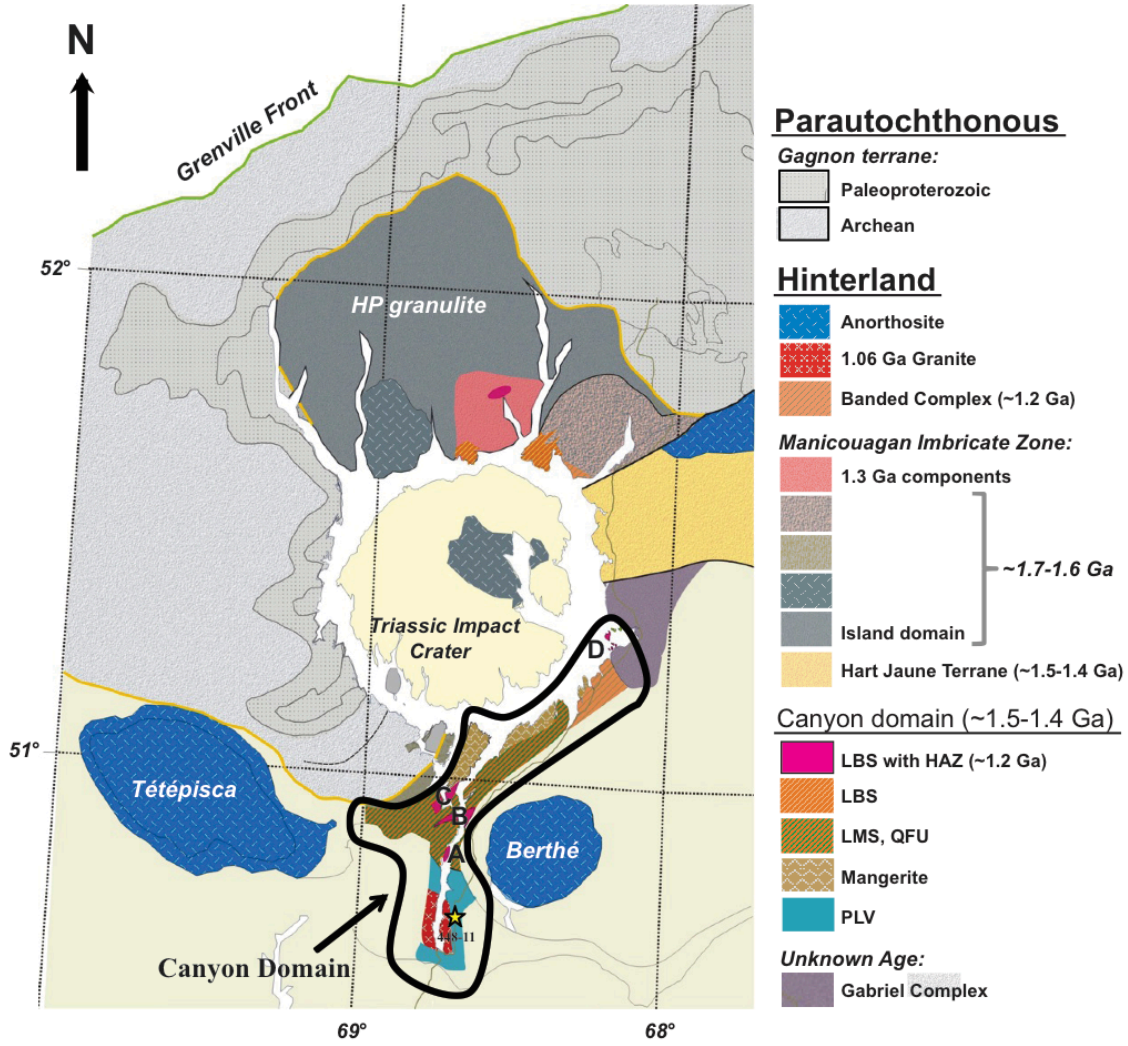

Figure 3.3: Simplified map of the Manicouagan area, A-D are locations of samples analyzed in this study (modified after Indares and Moukhsil 2013).

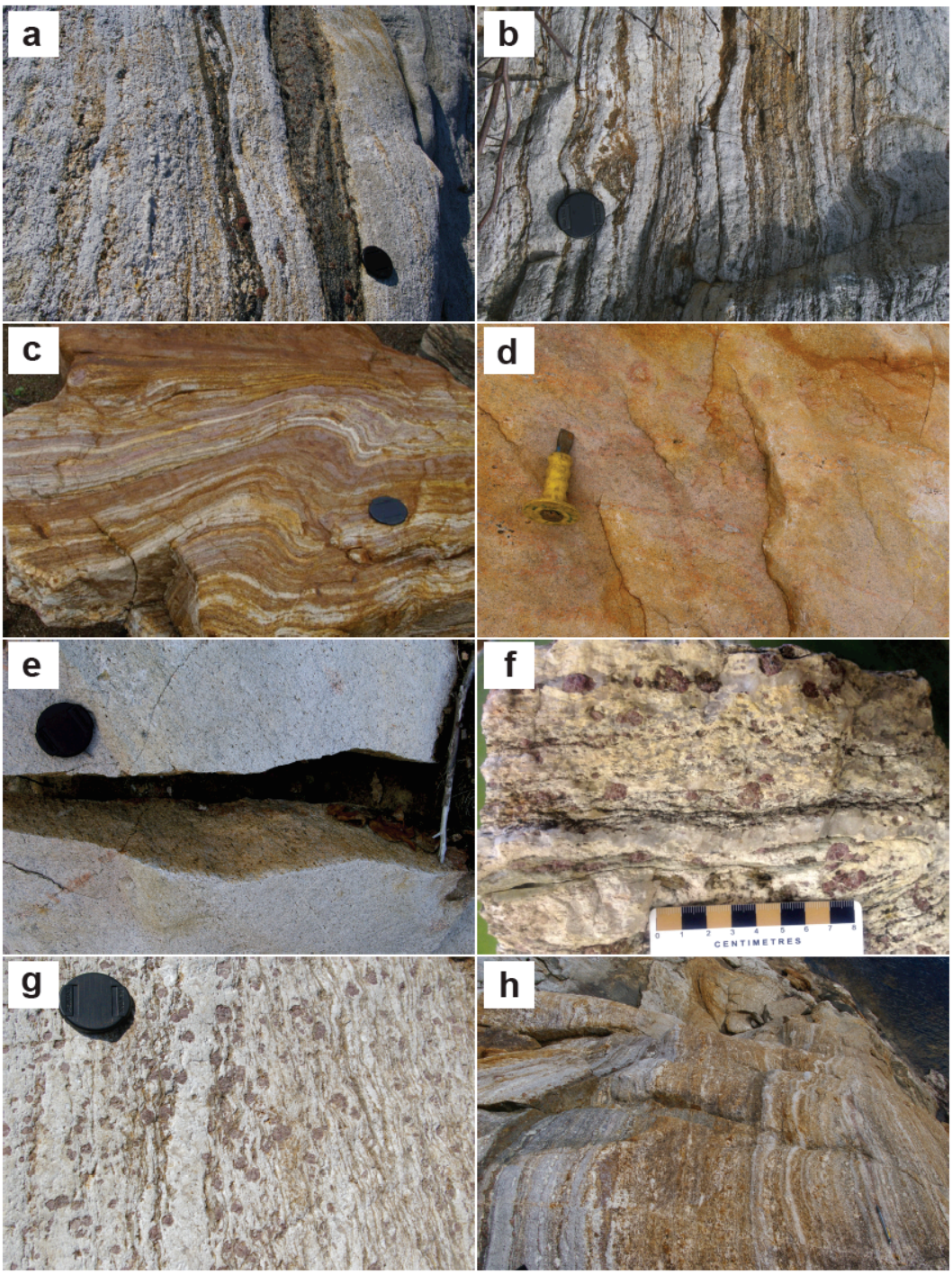

Figure 3.4: Main rock types from the hydrothermally altered zones (HAZ) of the LBS. **(a)** Alternating mafic and felsic layers; **(b)** white felsic gneisses locally containing aluminous layers or nodules (darker color layers); **(c)** white felsic gneiss grading into garnetites; **(d)** pink gneiss containing quartz-rich concretions surrounded by a hematized zone; **(e)** homogenous pink gneiss with elongate biotite aggregates; **(f, g)** white gneiss with aluminous nodules, sillimanite seams, and concordant quartz veins; and **(h)** homogeneous aluminous gneiss.

Chapter 4: ANALYTICAL METHODS

4.1 INTRODUCTION

The petrographic and geochemical study of the different rock types from the hydrothermally altered zones (HAZ) of the layered bimodal sequence (LBS) involved the integration of two methods of imaging and two methods of geochemical analysis, as follows:

(i) optical microscopy was carried out on polished thin sections to provide a first-order assessment of mineral assemblages and microstructures;

(ii) this was followed by X-ray mapping of selected thin sections using a scanning electron microscope and mineral liberation analysis software (SEM-MLA), to show mineral associations and their textural relationships at the thin section scale;

(iii) the chemical compositions of selected mineral species (garnet, biotite, spinel, feldspars) in aluminous gneiss, white gneiss, and garnetites were acquired by electron probe micro-analyzer (EPMA); and

(iv) the bulk rock compositions of selected samples were acquired by fusion and inductively-coupled plasma mass spectrometry (FUS-ICPMS) in order to provide information on the protolith, tectonic setting, and degree of alteration.

4.2 OPTICAL MICROSCOPY

Polished thin-sections were made in the Department of Earth Sciences, Memorial University of Newfoundland from a selection of LBS hand specimens collected during the 2003-04 and 2011 field seasons. These thin sections were examined using transmitted and reflected light with an Olympus BH2-UMA in the Department of Earth Sciences at

Memorial University of Newfoundland. In total, 56 thin sections were examined, and a subset of 30 was selected for a detailed study of microtextures. The results are discussed in Chapter 5.

4.3 SCANNING ELECTRON MICROSCOPE – MINERAL LIBERATION ANALYSIS (SEM-MLA)

Following initial examination by optical microscopy, a selection of 30 polished thin sections were carbon coated and imaged using a FEI Quanta 600 ESEM with a Roentec (now Bruker-AXS) XFlash® 3001 SDD energy dispersive X-ray (EDX) detector, and controlled by JKTech Mineral Liberation Analysis (MLA) image analysis software (Gu, 2003) at the Bruneau Center, Memorial University of Newfoundland.

Analytical conditions included an accelerating voltage of 25 kV, a beam current of 10 nA, a 2mm frame size (or horizontal field width, HFW), dwell time of 10 ms, and a step size of 50 μm. After carbon coating and correlating of all phases present in each sample, the MLA software was used to compute a precise point-counted estimation of mineral proportions (modes), and a composition-sensitive image of mineral associations and textural relationships (Shaffer *et al.* 2008). The software automatically: (a) acquires an image frame; (b) removes epoxy from consideration via a fixed threshold; (c) applies an algorithm for separating touching particles; (d) segments each particle for grain boundaries and surface defects; (e) acquires an X-ray spectrum from within the segmented grain; and (f) moves the stage to a new frame location when all X-ray spectra have been acquired (Shaffer 2009). Full thin section scanning took approximately 2-3 hours per sample.

Following scanning, the phases present were identified by comparing the acquired spectra with those of minerals from the database of the MLA software. Specific

compositional ranges in the sample undertaken were updated in the software where necessary. Then, the proportions the phases present were calculated with the MLA software and, by assigning a color for each phase, a false coloured mineral map showing the special distribution of the phases was computed. The colors were selected according to a preselected scheme, which was used for all samples to facilitate comparison among the obtained images. The results are discussed in Chapter 5.

4.4 MINERAL ANALYSIS BY ELECTRON PROBE MICRO-ANALYZER (EPMA)

After SEM-MLA imaging, a subset of 15 thin sections was selected for in situ major element mineral analysis by electron probe micro-analyzer (EPMA) using a JEOL JXA-8200 instrument at the Department of Geosciences, University of Calgary. Analyses were carried out with an accelerating voltage of 15 kV, a beam current at 20 nA, and a beam diameter of 10 μm. The instrument was calibrated using a range of natural and artificial standard materials of known composition, listed in Appendix A. Analytical uncertainties of the standards used for EPMA were based on theoretical calculations by the instrument, which were generally accepted with an approximation of accuracy +/- 2%. Attention was focused on the compositions of the solid-solution phases garnet, biotite, spinel and feldspars in the aluminous gneiss, white gneiss, and garnetites of the LBS (refer to Appendix A). SEM-MLA maps showing the locations and corresponding points of the analyses in Appendix A are shown in Appendix B, and the results are discussed in Chapter 6.

4.4.1 Recalculations of Mineral Analyses

Garnet compositions were recalculated on the basis of 12 oxygens per formula unit. Fe was apportioned into Fe^{3+} and Fe^{2+} cations using the equation: F=2X(1-T/S),

where F = Fe^{3+}, T = the ideal number of cations per formula unit (8), and S = the measured cation total per X oxygens (X=12) and is normalized (Droop 1987). End-member molar proportions were calculated in terms of almandine (Alm), pyrope (Prp), spessartine (Sps), andradite (And), and grossular (Grs) components. Fe^{3+} for And was calculated using a mean cation value for each garnet analyzed.

Biotite compositions were recalculated on the basis of 22 oxygens per formula unit with Ti and Al^{VI} [Al^{VI} = Al-Al^{IV}] assigned to octahedral sites, and Al^{IV} = [Al^{IV} = 2+(6-Si)] assigned to tetrahedral sites.

Spinel composition was recalculated on the basis of 4 oxygens per formula unit. As with garnet, Fe for spinel was apportioned into Fe^{3+} and Fe^{2+} cations using the equation F=2X(1-T/S). End-member molar proportions were calculated in terms of spinel (Spl), hercynite (Hc) = (Fe^{2+}- Fe^{3+}/2), gahnite (Gah), and magnetite (Mag) = (Fe^{3+}/2) components.

Feldspar compositions were recalculated on the basis of 8 oxygens per formula unit, and the molar proportions of orthoclase (Or), albite (Ab), and anorthite (An) components were calculated based on cation proportions of K^+, Na^+ and Ca^{2+}.

4.5 WHOLE-ROCK ANALYSIS

Twenty-three samples were selected for whole-rock analysis by fusion pre-preparation following inductively-coupled plasma optical emission spectrometry (ICP-OES) for majors and some minor/trace elements, and mass spectrometry (ICP-MS) for most trace elements. Samples were sent to Activation Laboratories Ltd. (Actlabs) in Ancaster, Ontario, and analyzed under the combination package Code 4B (lithium metaborate/tetaborate fusion ICP whole rock) and Code 4B2 (trace element ICP-MS).

The precision of detection limit for fusion ICP (%) and trace element ICP-MS (ppm) are listed in Appendix C. Samples chosen were visually homogeneous in character with the exception of garnetite sample 355cx-11, which was separated into 3 sub-samples, 355cxA-11, 355cxB-11 and 355cxC-11. 355cxB-11 represents a felsic layer and is classified with the white gneisses.

Whole-rock major and trace contents of the samples analyzed are listed in Appendix C. Major oxides (volatile free) were normalized to 100% on the basis of Fe total = FeO* using the software IgPet. Loss on ignition (LOI) of major elements ranged in from -1.49 to 1.29%. Elements given values of '<' were considered to be present at half the given value (refer to Appendix C). Whole-rock chemistry is discussed in Chapter 7.

Chapter 5: PETROGRAPHY

5.1 INTRODUCTION

The mineralogy and textures from a selection of 9 aluminous gneisses, 6 white gneisses, 4 pink gneisses, and 5 garnetites were documented by a means of SEM-MLA imaging and optical microscopy. SEM-MLA imaging provided mineralogical 'maps' showing the distribution of phases and textures at the thin section scale, and a precise estimation of mineral modes. In addition, the different compositions in feldspars was mapped as orthoclase and perthite for K-feldspar, and albite and anorthite for plagioclase by the MLA software. Detailed microtextures were examined by a means of optical microscopy. The mineral modes determined from SEM-MLA imaging per sample are listed in Table 5.1.

5.2 ALUMINOUS GNEISSES

These rocks have a gneissic fabric and mainly consist of garnet, sillimanite, biotite, plagioclase, quartz and K-feldspar, with the total of aluminous minerals (garnet, biotite, sillimanite, spinel, corundum, and cordierite) ranging from ~10 to 31% (Table 5.1). Based on the spatial distribution of these minerals, rocks are classified into two types: (i) nodular gneisses in which aluminous minerals mainly occur in several mm large clusters or nodules; and (ii) relatively homogeneous gneisses in which aluminous minerals tend to concentrate in diffuse layers.

5.2.1 Nodular Gneisses

In these gneisses, aluminous nodules are enclosed in: (a) a quartzofeldspathic matrix (samples *354-2-04* loc. A, *10-A1-76* loc. D, and *333-2-03* loc. C); or (b) in a

matrix dominated by K-feldspar (samples *339-11* loc. B, *333x-03* loc. C, and *355-1-04* loc. A).

5.2.1.1 Gneisses with Aluminous Nodules in a Quartzofeldspathic matrix

In samples ***354-2-04*** (Fig. 5.1a) and ***10-A1-76*** (Fig. 5.1b), the nodules consist of garnet, biotite, sillimanite, spinel, corundum, plagioclase and minor sulfides and are mineralogically zoned (Fig. 5.1a). Sillimanite, spinel and corundum are concentrated in the central part of nodules (Fig. 5.2a), and are variably overgrown by garnet aggregates with composite inclusions of plagioclase enclosing rounded quartz grains (Fig. 5.2b). Biotite corrodes garnet and forms clusters mainly concentrated at the rims of the aggregates (Fig. 5.2c). The nodules are mantled by plagioclase, which becomes more albitic towards the matrix (Fig. 5.1a), and are rimmed by perthitic K-feldspar with blebby exsolution of plagioclase and inclusions of quartz and biotite (Fig. 5.2d). In sample *10-A1-76*, garnet also occurs as a porphyroblast with a tail feature (Fig. 5.1b). The quartzofeldspathic matrix consists of relatively fine-grained perthitic K-feldspar with fine exsolution, plagioclase, randomly oriented interstitial biotite, and isolated anhedral quartz. In sample *354-2-04*, discontinuous ribbons of quartz branch through a layer of K-feldspar between two nodules (Fig. 5.1a). Quartz ribbons are partially recrystallized and resorbed, and contain inclusions of feldspar and biotite (Fig. 5.2e). In sample *10-A1-76*, the matrix is a fine K-feldspar rich groundmass with clusters of quartz (Fig. 5.1b).

Sample ***333-2-03*** (Fig. 5.1c) contains one nodule of elongated garnet variably corroded by biotite (Fig. 5.2f), and rimmed by plagioclase. In this sample, garnet also occurs as euhedral grains scattered in the matrix (Fig. 5.1c). These garnets contain inclusions of quartz in pools of K-feldspar (Fig. 5.2g). The quartzofeldspathic matrix consists of relatively fine-grained perthitic K-feldspar (and minor microcline),

plagioclase, variably oriented interstitial biotite, and flattened partially recrystallized and corroded quartz with inclusions of feldspar and biotite (Fig. 5.2h).

5.2.1.2 Gneisses with Aluminous Nodules in a K-feldspar matrix

Samples ***339-11*** (Fig. 5.3a), ***333x-03*** (Fig. 5.3b) and ***355-1-04*** (Fig. 5.3c) are characterized by large aluminous nodules, discontinuous sillimanite seams (*339-11, 333x-03*), and large elongated partly recrystallized and resorbed quartz (*333x-03*), in a K-feldspar dominated matrix. The aluminous nodules consist of: (a) garnet porphyroblasts with polymineralic inclusions of sillimanite, biotite, plagioclase and quartz in pools of feldspar (*339-11*; Fig. 5.4a), and rimmed by thin layers of biotite-sillimanite and albitic plagioclase (*333x-03*; Fig. 5.3a); (b) diffuse clusters of small framboidal garnet overgrowing the matrix (Fig. 5.4b), and sillimanite seams (Fig. 5.4c), locally corroded by biotite (Fig. 5.3b); and (c) coarse sillimanite aggregates with subordinate garnet and biotite partly rimmed by plagioclase (*355-1-04*; Fig. 5.3c). The matrix (locally sericitized) consists of a fine groundmass of K-feldspar with minor quartz, plagioclase, randomly oriented interstitial biotite and minor sulfides. K-feldspar is perthitic with fine exsolution of plagioclase, contains inclusions of quartz, and is corroded and rimmed by myrmekite (Fig. 5.4d).

5.2.2 Homogeneous Gneisses

This group includes samples ***331E2-11*** (Fig. 5.5a), ***331-3-03*** (Fig. 5.5b), and ***333-03*** (Fig. 5.5c) from location C. In samples ***331E2-11*** (Fig. 5.5a) and ***331-3-03*** (Fig. 5.5b), garnet, biotite, sillimanite, and plagioclase are concentrated in diffuse layers. Garnet porphyroblasts contain polymineralic inclusions of sillimanite, biotite, plagioclase and quartz in pools of feldspar (Fig. 5.6a). They locally overgrow clusters of sillimanite blades (Fig. 5.6b) and are variably corroded by biotite. Garnet and associated biotite is

mantled by plagioclase that becomes albitic towards the matrix (Fig. 5.5a). Biotite also occurs as isolated clusters of larger grains in the matrix. The matrix is defined by a relatively fine-grained groundmass dominated by K-feldspar with locally microcline twinning (Fig. 5.6c). This matrix encloses: (a) large perthitic K-feldspar with fine exsolution of plagioclase and quartz inclusions (Fig. 5.6d); (b) partially recrystallized and resorbed quartz aggregates (Fig. 5.5a), with inclusions of feldspar and biotite (Fig. 5.6e); and (c) minor disseminated sulfides (Fig. 5.5a). In sample *331E2-11*, the largest aggregates of quartz have an overall triangular shape (Fig. 5.5a).

Sample ***333-03*** (Fig. 5.5c) consists of euhedral garnet porphyroblasts scattered in a layered quartzofeldspathic matrix. Garnet contains polymineralic inclusions of biotite, plagioclase and quartz in pools of feldspar, and is variably corroded by biotite. The matrix is dominated by K-feldspar and consists of discontinuous partially recrystallized and resorbed ribbons of quartz, plagioclase and interstitial biotite. K-feldspar is perthitic with blebby exsolution of plagioclase and is locally rimmed by myrmekite (Fig. 5.6f). Quartz ribbons contain inclusions of biotite and feldspar (Fig. 5.6g).

5.3 WHITE GNEISSES

Samples from this suite of rocks have a white or 'bleached' appearance and mainly consist of K-feldspar, quartz and lesser plagioclase. They contain up to 11% garnet with traces of biotite, and in some cases, sillimanite (Table 5-1).

Sample ***355a-11*** (Fig. 5.7a) from location A is the most felsic of this suite, and has <1% Grt-Sill-Bt. ***206a-04*** (Fig. 5.7b) from location B and ***355b1-11*** (Fig. 5.7c) from location A are layered (in terms of proportion of quartzofeldspathic minerals) and peppered by garnet, which is mainly concentrated in K-feldspar-poor layers. ***2163d2-11***

(Fig. 5.8a) from location C and ***448-11*** (Fig. 5.8b) from the Complexe de la Plus Value (PLV), are the most coarse-grained and are characterized by large flattened quartz aggregates in a K-feldspar-rich matrix. Finally, sample ***A1-10-90A2*** (Fig. 5.8c) from location D is distinct from the rest of the white gneisses by having thin sillimanite-bearing layers in a fine-grained quartz dominated matrix.

Garnet in this suite of rocks occurs as nodular (Fig. 5.7a) or euhedral porphyroblasts either concentred into elongate clusters (Fig. 5.9a) or scattered in the matrix. Porphyroblasts contain inclusions of plagioclase and quartz in pools of feldspar (Fig. 5.9b). In addition, garnet is pinkish under plane-polarized light (Fig. 5.9c), and variably corroded by biotite (Fig. 5.8a). Locally, garnet rims sillimanite seams (sample *A1-10-90A2*; Figs. 5.8c and 5.9d).

The matrix is fine to coarse-grained, and is generally K-feldspar-rich (except for *A1-10-90A2*), with variable amounts of quartz and plagioclase, and minor interstitial biotite. K-feldspar occurs as larger perthitic grains with blebby or fine exsolution of plagioclase (Fig. 5.9e), and smaller grains of microcline (Fig. 5.9f). K-feldspar contains inclusions of quartz and is commonly rimmed by myrmekite. In samples *206a-04* and *355b1-11*, quartz locally occurs as partially recrystallized and resorbed ribbons with inclusions of feldspar (Fig. 5.9g) enclosed in, or rimming K-feldspar layers (Fig. 5.7b and 5.7c). In contrast, samples *2163d2-11* and *448-11* quartz commonly occurs as flattened partially recrystallized and resorbed aggregates with inclusions of feldspar (Fig. 5.9h) that are segregated in discontinuous layers in the matrix. The matrix in sample *A1-10-90A2* is a fine-grained compositionally layered groundmass dominated by quartz, with lesser plagioclase and perthitic K-feldspar.

5.4 PINK GNEISSES

All members of this suite of four felsic rocks (339b1-11, 399b2-11, 319-1-11, and 216e-11) have a pinkish color and mainly consist of K-feldspar, quartz, plagioclase and minor biotite or hornblende. Samples ***339b1-11*** (Fig. 5.10a) and ***339b2-11*** (Fig. 5.10b) from location B are characterized by branching bands of quartz and/ or large quartz aggregates consisting of K-feldspar, lesser plagioclase, and minor biotite (locally chloritized). K-feldspar is perthitic with blebby exsolution of plagioclase and inclusions of quartz (Fig. 5.11a). Branching bands of partially recrystallized quartz contain inclusions of feldspar (Fig. 5.11b) and are commonly rimmed by flattened aggregates of biotite (Fig. 5.11c and Fig. 511d). In sample *339b2-11*, the matrix is coarser-grained and contains flattened and corroded quartz aggregates with inclusions of feldspar (Fig. 5.11e), and zoned plagioclase (Fig. 5.11f).

Sample ***319-1-11*** (Fig. 5.12a) from location B has a relatively homogeneous fine-grained matrix with rare hornblende porphyroblasts containing quartz inclusions (Fig. 5.13a). ***216e-11*** (Fig. 4.12b) from location C contains randomly oriented biotite and layers of K-feldspar in a coarse-grained matrix. The matrix of sample *319-1-11* consists of perthitic K-feldspar with blebby exsolution of plagioclase (Fig. 5.13b), smaller microcline grains (Fig. 5.13c), lesser plagioclase, and partially recrystallized and resorbed quartz clusters with inclusions of feldspar (Fig. 5.13d). The matrix of sample *216e-11* consists of K-feldspar, plagioclase, and quartz. Layers of perthitic K-feldspar with fine exsolutions and inclusions of plagioclase, quartz and biotite (Fig. 5.13e), contain partially recrystallized and resorbed ribbons of quartz with inclusions of feldspar (Fig. 5.13f).

5.5 GARNETITES

Samples from this suite of rocks are from location A and represent variable degrees of 'garnetitization' of the white gneisses, with garnet ranging from ~19 to 71% (Table 5-1). These rocks consist of garnet, quartz, K-feldspar, plagioclase, and minor graphite and biotite.

Garnetites ***355c1-11*** (Fig. 5.14a), ***355-2a-04*** (Fig. 5.14b) and ***355c2-11*** (Fig. 5.14c) are characterized by compositional layering defined by the distribution of garnet and K-feldspar. In contrast, sample ***355c3-11*** (Fig. 5.15a) is a massive and homogeneous garnetite without compositional layering observed at the thin section scale. ***355cx-11*** (Fig. 5.15b) is the least garnetized and most quartz rich sample in this suite.

Garnet in these rocks occurs as tightly packed euhedral grains with tiny inclusions of quartz and plagioclase (Fig. 5.16a) locally rimmed by graphite (Fig. 5.16b) and myrmekite (Fig. 5.16c). In sample *355-2a-04*, locally altered layers of K-feldspar contain pinnite overgrown by garnet (Fig. 5.16d). The matrix is quartz dominant, with K-feldspar and lesser plagioclase. Sample *355c2-11* is finer-grained, and contains layers of perthitic K-feldspar with discontinuous branching ribbons of partially recrystallized and resorbed quartz with inclusions of feldspar (Fig. 5.16e). The quartz matrix in sample *355c3-11* has an interstitial character between porphyroblasts (Fig. 5.16f). Quartz-bearing layers in *355cx-11* contain round inclusions of garnet (Fig. 5.16g) and discontinuous layers of plagioclase (locally sericitized).

5.6 TEXTURAL INTERPRETATION

The investigated felsic and aluminous rocks types from HAZ in the LBS show: (a) preserved relict textures that provide constraints on the protolith; (b) textures diagnostic

of hydrothermal alteration prior to metamorphism; and (c) textures related to granulite-facies metamorphism and partial melting.

5.6.1 Relict textures diagnostic of the protolith

Relict primary textures are best observed in the aluminous gneisses and consist of recrystallized and resorbed angular quartz domains that preserve a bipyramidal shape (Fig. 5.17a), typical of quartz phenocrysts in felsic volcanic rocks (Gifkins *et al.* 2005). These are similar to bipyramidal quartz phenocrysts from the Hores Gneiss surrounding the Broken Hill Pb-Zn-Ag deposit, which are preserved at amphibolite-facies conditions, and have been used to infer a volcanic origin for the host rock (Stevens and Barron 2002). In addition, lenticular (Fig. 5.17b) flattened angular quartz aggregates (Fig. 5.17c) corroded by a finer-grained K-feldspar matrix may also represent evidence of recrystallized and flattened quartz phenocrysts (Bonnet *et al.* 2005; Bonnet and Corriveau 2007). Large and corroded perthitic K-feldspar with round inclusions of quartz in a much finer groundmass in the white gneisses (sample *355a-11*; Fig. 5.17d) is another potential case of relict phenocrysts in a volcanic host. Finally, flattened aggregates of biotite observed in a pink gneiss sample (*339b2-11*; Fig. 5.17e and 5.17f) may also represent relicts of an earlier feature. These may be compared with the biotite aggregates in the Hores Gneiss, which were interpreted by Stevens and Barron (2002) as potentially derived from altered fiamme or lapilli.

5.6.2 Pre-metamorphic hydrothermal alteration

Diagnostic features of felsic gneisses that experienced pre-metamorphic hydrothermal alteration include nodular or vein-like distribution of minerals and unusual mineral proportions, as described earlier in chapter two (e.g. Bonnet and Corriveau 2007). Such features also occur in the aluminous gneiss and garnetites of the LBS.

Nodular textures were observed in several aluminous gneisses, where the nodules are characterized by a high concentration of garnet and sillimanite (with cases of corundum and spinel; Fig. 5.18a). The same rocks are also characterized by:

(a) seams of sillimanite (Fig. 5.18b);

(b) concordant quartz veins (Fig. 5.18c); and

(c) abnormally high concentrations of K-feldspar in the matrix.

Collectively, these features are suggestive of K and Al enrichment, which is consistent with sericitic and argillic types of alteration (Hannington *et al.* 2003; Galley *et al.* 2007; Bonnet *et al.* 2005; Bonnet and Corriveau 2007). Variably disconnected quartz veins are always present in rocks with silimanite seams, and may attest to fluid circulation during hydrothermal alteration (Figs. 3.4f and 5.3A). In addition, we note that similar types of alteration are also reported from quartzofeldspathic and aluminous gneisses from La Romaine (Bonnet *et al.* 2005), which contain abundant lenticular clusters of aluminous minerals and/ or sillimanite trains within garnet, and dismembered quartz veins.

In addition, the gradual garnetitzation of the white gneisses observed in several localities (Fig. 5.18d), provides compelling evidence of a hydrothermal origin of the garnet-rich rocks. The most famous garnetites in metamorphosed VMS environments at Broken Hill, has massive to laminated varieties, which have been interpreted as the product of a metamorphosed Mn-rich sediment or exhalative origin of hydrothermally altered sediments (Schwandt *et al.* 1993; Spry and Wonder 1989). Garnetites observed from the LBS are of clearly hydrothermal origin, but less developed than those from Broken Hill.

5.6.3 Metamorphism and partial melting

The aluminous gneisses preserve the most complex metamorphic microstructures. The dominant mineral assemblage in these gneisses is garnet-sillimanite-biotite-quartz-K-feldspar-plagioclase, which is typical of mid-*P* granulite-facies metamorphism in systems of pelitic composition (Spear *et al.* 1999; Bonnet and Corriveau 2007; Vernon and Clarke 2008). This assemblage is stable in the P-T field of the dehydration melting of biotite by the continuous reaction: biotite + sillimanite + quartz → garnet + melt + K-feldspar ([R2]; Spear *et al.* 1999).

Microstructural evidence of the former operation of this partial melting reaction in aluminous gneisses is preserved as:

(a) composite inclusions in garnet porphyroblasts consisting of corroded quartz±sillimanite±biotite (reactants of [R2]) in films or pools of feldspar, which represent former melt (Fig. 5.19a); and

(b) garnet (product in [R2]) overgrowing sillimanite (Fig. 5.19b).

In addition, local corrosion of garnet by biotite (Fig. 5.19c) is consistent with the reverse operation of [R2], during retrogression and melt crystallization. The presence of sillimanite inclusions in garnet suggests that a large part of the prograde evolution of these aluminous gneisses occurred in the sillimanite stability field. This, together with the absence of retrograde cordierite during melt crystallization is consistent with the generalized P-T shown in Fig. 5.19d. This P-T path is broadly similar to those predicted by P-T pseudosections calculated for other aluminous samples from the same area (Laselle *et al.* 2014).

Table 5.1: Mineral modes aquired by SEM-MLA imaging of selected samples.

	Aluminous Gneisses									*White Gneisses*					
Sample:	**354-2-04**	**10-A1-76**	**331E2-11**	**331-3-03**	**RS339-11**	**333x-03**	**MS355-1-04**	**333-03**	**333-2-03**	**355a-11**	**206a-04**	**355b1-11**	**2163d2-11**	**448-11**	**A1-10-90A2**
Quartz	18.74	21.73	13.39	28.56	12.1	5.81	14.58	15.98	38.36	25.85	31.18	32.98	38.59	36.27	57.61
Orthoclase	25.78	43.85	32.58	26.75	23.46	30.21	44.32	19.92	10.05	54.79	25.11	32.18	23.47	43.39	15.59
Perthite	1.48	1.61	2.83	1.8	1.88	5.51	1.28	2.6	2.01	0.89	1.8	1.43	2.82	1.12	1.11
Sum Ksp	**27.26**	**45.46**	**35.41**	**28.55**	**25.34**	**35.72**	**45.6**	**22.52**	**12.06**	**55.68**	**26.91**	**33.61**	**26.29**	**44.51**	**16.7**
Plagioclase An (10-30)	20.71	13.26	13.17	7.53	7.38	2.31	11.56	32.59	23.89	12.22	22.58	21.07	13.78	9.15	0.57
Albite	10.27	3.26	6.76	3.26	9.45	20.94	1.17	3.3	9.35	2.91	3.09	3.43	4.67	4.15	14.69
Sum Plg	**30.98**	**16.52**	**19.93**	**10.79**	**16.83**	**23.25**	**12.73**	**35.89**	**33.24**	**15.13**	**25.67**	**24.5**	**18.45**	**13.3**	**15.26**
Sum QF minerals	**76.98**	**83.71**	**68.73**	**67.9**	**54.27**	**64.78**	**72.91**	**74.39**	**83.66**	**96.66**	**83.76**	**91.09**	**83.33**	**94.08**	**89.57**
Garnet	6.09	4.44	3.28	4.5	22.97	19.05	4.72	10.81	6.38	0	10.71	3.91	9	3.55	6.88
Biotite	10.97	4.86	17.11	12.41	5.65	1.91	3.98	9.61	6.14	0.12	0.27	0.1	1.4	0.13	0
Sillimanite	0.48	0	0.53	0.32	2.66	1.16	13.19	0	0	0.03	0	0	0	0	1.05
Spinel	0.16	0.23	0	0	0	0	0	0	0	0	0	0	0	0	0
Corundum	0.14	0	0	0	0	0	0	0	0	0	0	0	0	0	0
Cordierite	0	0	0	0	0	0	0	0	0	0	0	0	0	0	0
Sum Al+FM minerals	**17.84**	**9.53**	**20.92**	**17.23**	**31.28**	**22.12**	**21.89**	**20.42**	**12.52**	**0.15**	**10.98**	**4.01**	**10.4**	**3.68**	**7.93**
Chlorite	2.61	2.26	2.65	5.51	5.99	8.41	1.72	1.82	1.62	1.29	1.36	1.46	2.28	1.3	1.56
Sericite	0.53	0.66	0.77	1.57	1.8	1.49	0.34	0.65	0.44	0.19	1.49	1.05	1.45	0.11	-
Sulphides	-	0.15	0.54	0.44	-	-	-	-	-	-	-	-	-	-	-
Graphite	-	-	-	-	-	-	-	-	-	-	-	-	-	-	-
Ilmenite	0.15	0.15	0.34	0.61	1.63	-	-	0.23	0.11	-	1.82	0.19	0.19	0.23	0.17
Rutile	-	-	-	0.14	0.16	0.39	0.23	0.16	0.12	-	0.11	0.27	0.25	-	0.18
Monazite	-	-	-	-	-	-	-	-	-	-	-	-	-	-	-
Magnetite	-	-	-	-	-	-	-	-	-	-	-	-	-	-	-
Apatite	-	-	-	-	-	-	-	-	-	-	0.64	-	-	-	-
Calcite	-	-	-	-	-	-	-	-	-	-	-	-	0.51	-	-
Titanite	-	-	-	-	-	-	-	-	-	-	-	-	-	-	-
Hornblende	-	-	-	-	-	-	-	-	-	-	-	-	-	-	-
Magnetite (Ti)	-	-	-	-	-	-	-	-	-	-	-	-	-	-	-
Allanite	-	-	-	-	-	-	-	-	-	-	-	-	-	-	-

Table 5.1: (cont.)

	Pink Gneisses				*Garnetites*				
Sample:	**339b1-11**	**399b2-11**	**319-1-11**	**216e-11**	**355c1-11**	**355-2a-04**	**355c2-11**	**355c3-11**	**355cx-11**
Quartz	49.68	39.19	40.32	26.1	36.7	40.5	30.4	21.12	53.53
Orthoclase	22.38	25.69	32.14	29.93	18.04	22.07	34.59	0	0
Perthite	4.03	11.77	4.85	0.91	0.85	1.03	0.87	0	0.36
Sum Ksp	**26.41**	**37.46**	**36.99**	**30.84**	**18.89**	**23.1**	**35.46**	**0**	**0.36**
Plagioclase An (10-30)	3.31	0.66	14.84	34.11	2.5	0	8.76	0	10.36
Albite	17.74	19.59	3.79	1.11	1.05	2.53	0.87	0	0.49
Sum Plg	**21.05**	**20.25**	**18.63**	**35.22**	**3.55**	**2.53**	**9.63**	**0**	**10.85**
Sum QF minerals	**97.14**	**96.9**	**95.94**	**92.16**	**59.14**	**66.13**	**75.49**	**21.12**	**64.74**
Garnet	0	0	0	0	32.4	28.56	22.62	69.49	22.51
Biotite	0.19	0.3	0.2	5.38	0	0.17	0	0.13	0.12
Sillimanite	0	0	0	0	0	0	0	0	0
Spinel	0	0	0	0	0	0	0	0	0
Corundum	0	0	0	0	0	0	0	0	0
Cordierite	0	0	0	0	0	0	0	1.55	0
Sum Al+FM minerals	**0.19**	**0.3**	**0.2**	**5.38**	**32.4**	**28.73**	**22.62**	**71.17**	**22.63**
Chlorite	0.64	1.13	0.68	0.31	1.59	0.86	0.12	0.92	2.56
Sericite	0.6	0.86	0.91	-	0.87	1.27	0.42	-	0.23
Sulphides	-	-	-	-	-	-	-	-	0.23
Graphite	-	-	-	-	2.89	0.68	-	-	1.91
Ilmenite	-	-	0.29	0.14	1.49	0.61	0.15	3.38	0.94
Rutile	-	-	-	-	0.16	0.21	0.26	-	-
Monazite	-	-	-	-	-	-	-	-	-
Magnetite	-	-	0.54	0.23	-	-	0.14	-	0.14
Apatite	-	-	-	0.17	-	-	-	0.13	-
Calcite	-	-	-	-	-	-	-	-	-
Titanite	-	-	-	-	-	-	-	-	-
Hornblende	-	-	-	-	-	-	-	-	-
Magnetite (Ti)	-	-	0.43	-	-	-	-	-	0.43
Allanite	-	-	0.2	-	-	-	-	-	-

Sum Ksp: orthoclase + perthite
Sum Plag: plagioclase An (10-30) + albite
Sum QF minerals: Total of quartzofeldspathic minerals
Sum Al+FM minerals: Total of aluminous and ferromagnesian minerals

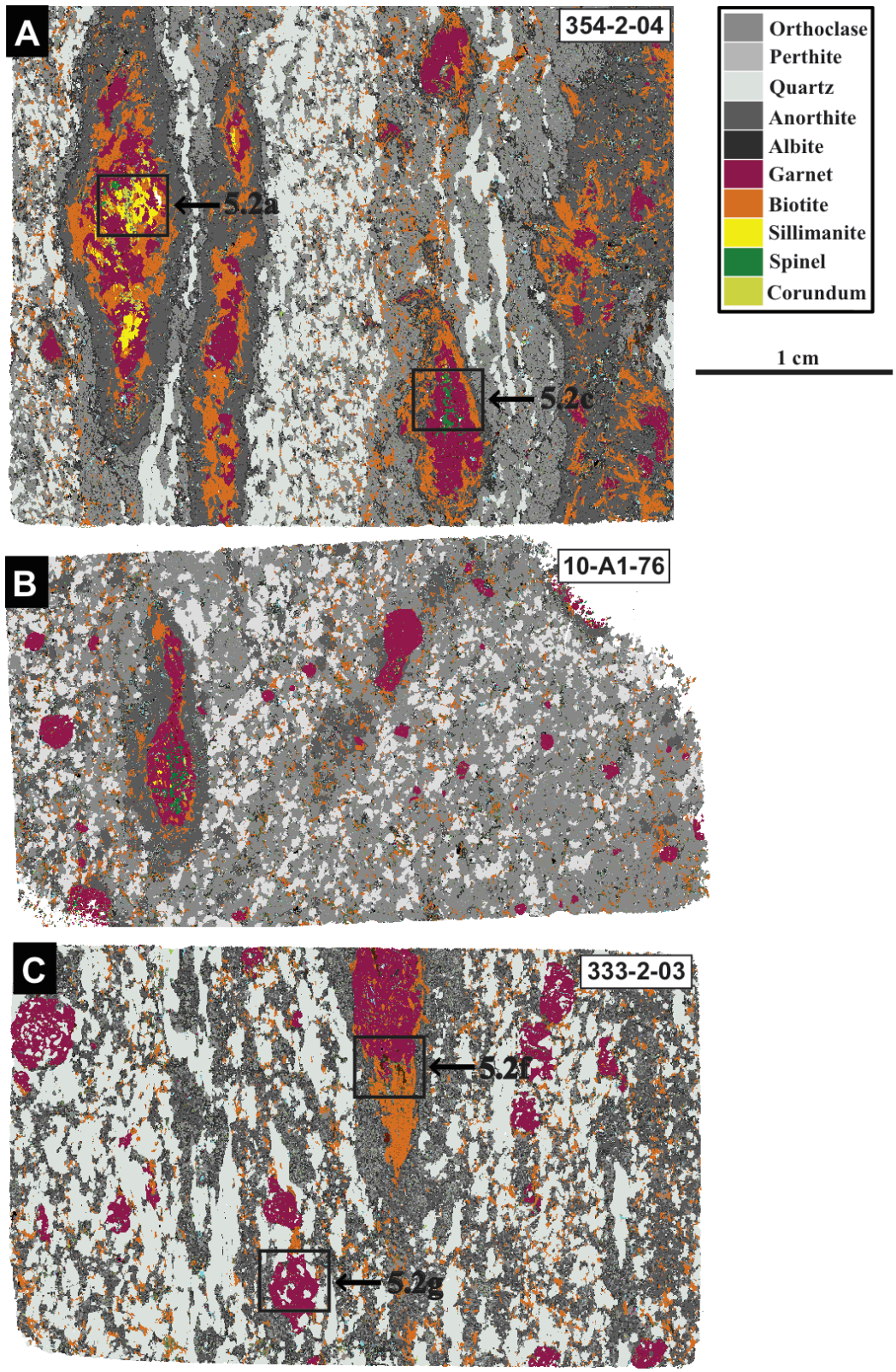

Figure 5.1: SEM-MLA mineral maps of gneisses with aluminous nodules in a quartzofeldspathic matrix. **(A)** 354-2-04; **(B)** 10-A1-76; and **(C)** 333-2-03.

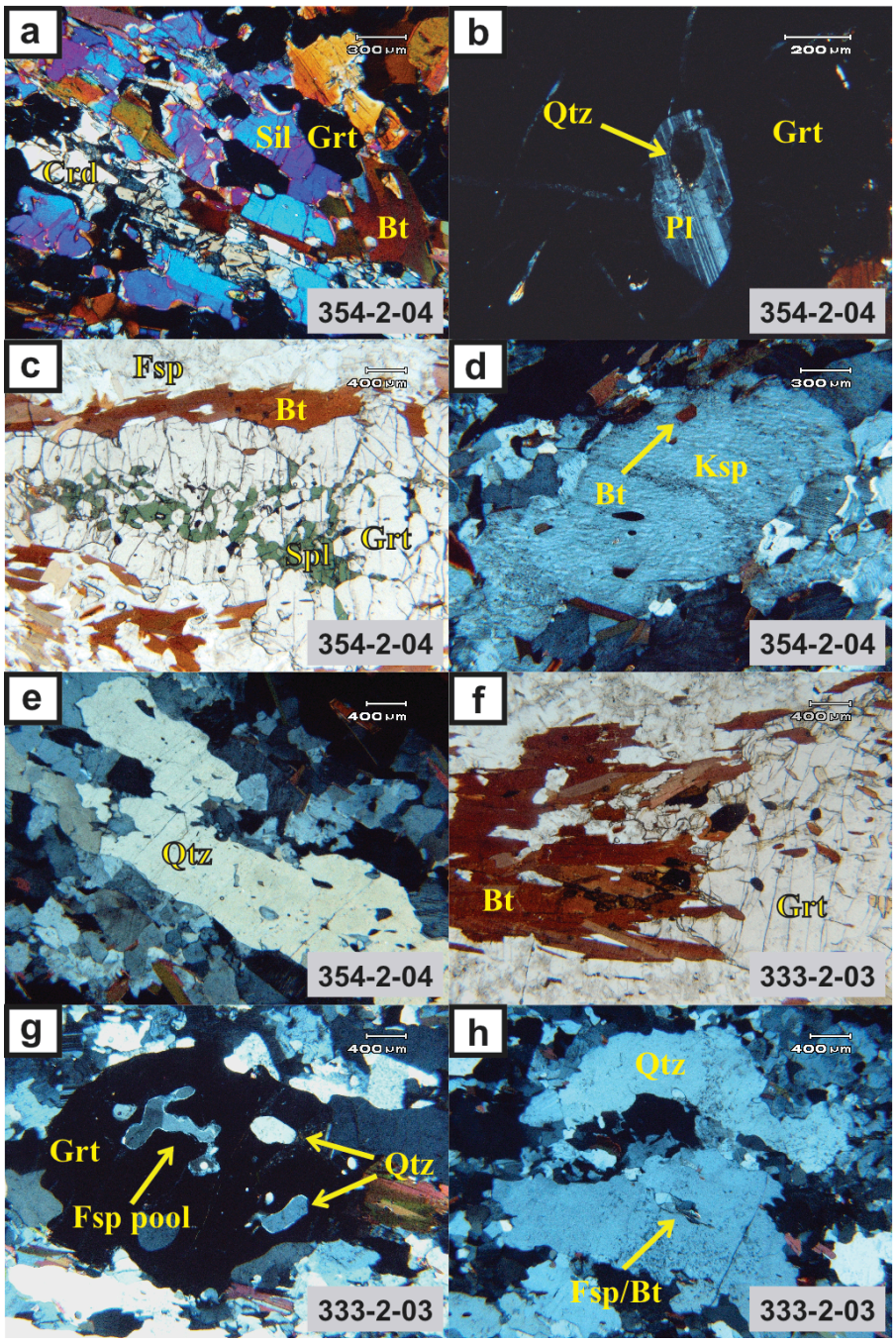

Figure 5.2: Photomicrographs of gneisses with aluminous nodules in a quartzofeldspathic matrix. **(a)** Nodule with sillimanite, spinel and corundum in the center overgrown by garnet aggregates (XPL); **(b)** garnet with composite inclusions of plagioclase enclosing round quartz (XPL); **(c)** biotite clusters corroding a garnet nodule with inclusions of spinel in the center (PPL); **(d)** perthitic K-feldspar with blebby exsolution of plagioclase and inclusions of quartz and biotite (XPL); **(e)** partially recrystallized and corroded quartz ribbons with inclusions of feldspar and biotite (XPL); **(f)** nodular garnet variably corroded by biotite (PPL); **(g)** garnet with inclusions of quartz in pools of K-feldspar (XPL); and **(h)** recrystallized quartz with inclusions of feldspar and biotite (XPL).

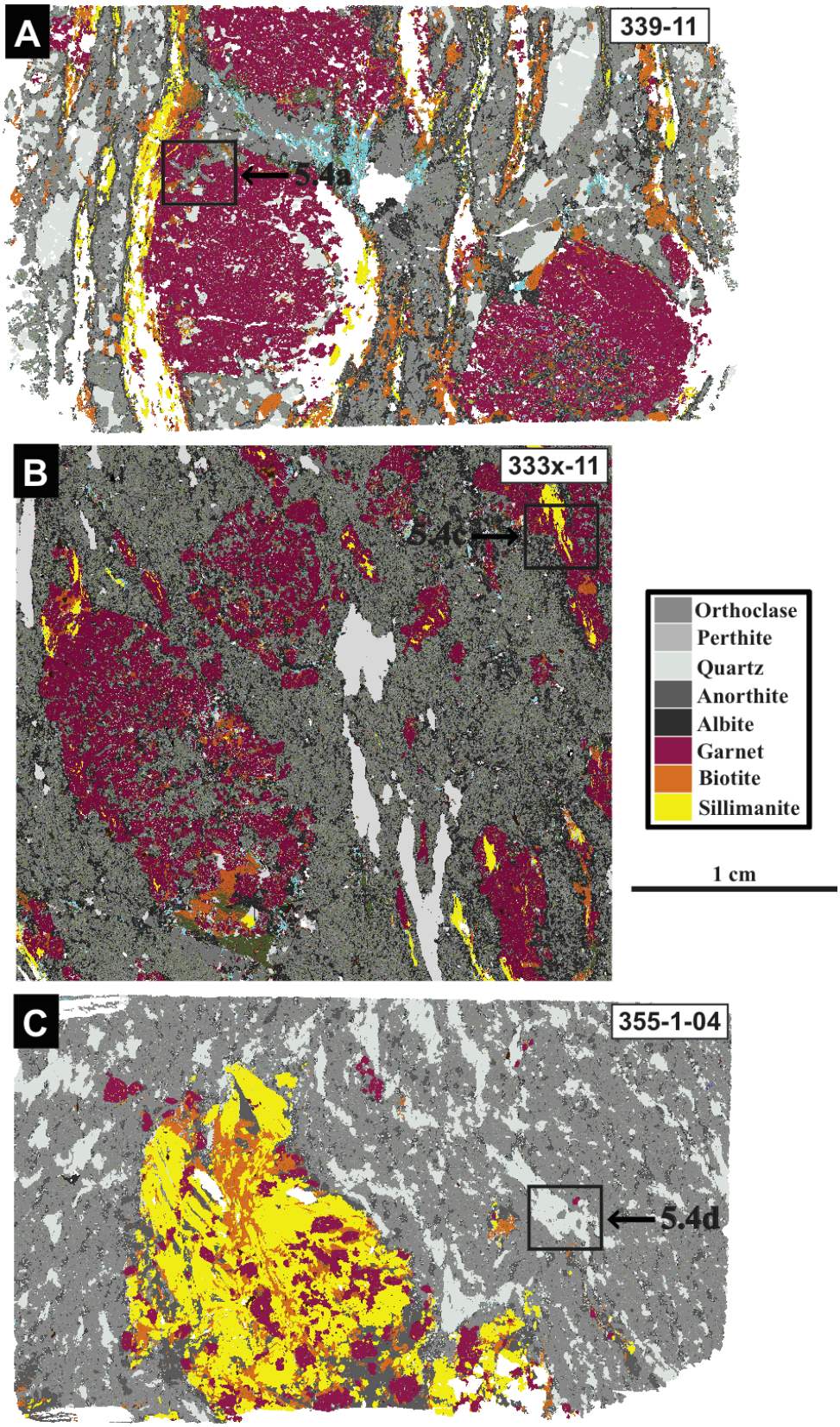

Figure 5.3: SEM-MLA mineral maps of gneisses with aluminous nodules in a K-feldspar matrix. **(A)** 339-11; **(B)** 333x-03; and **(C)** 355-1-04.

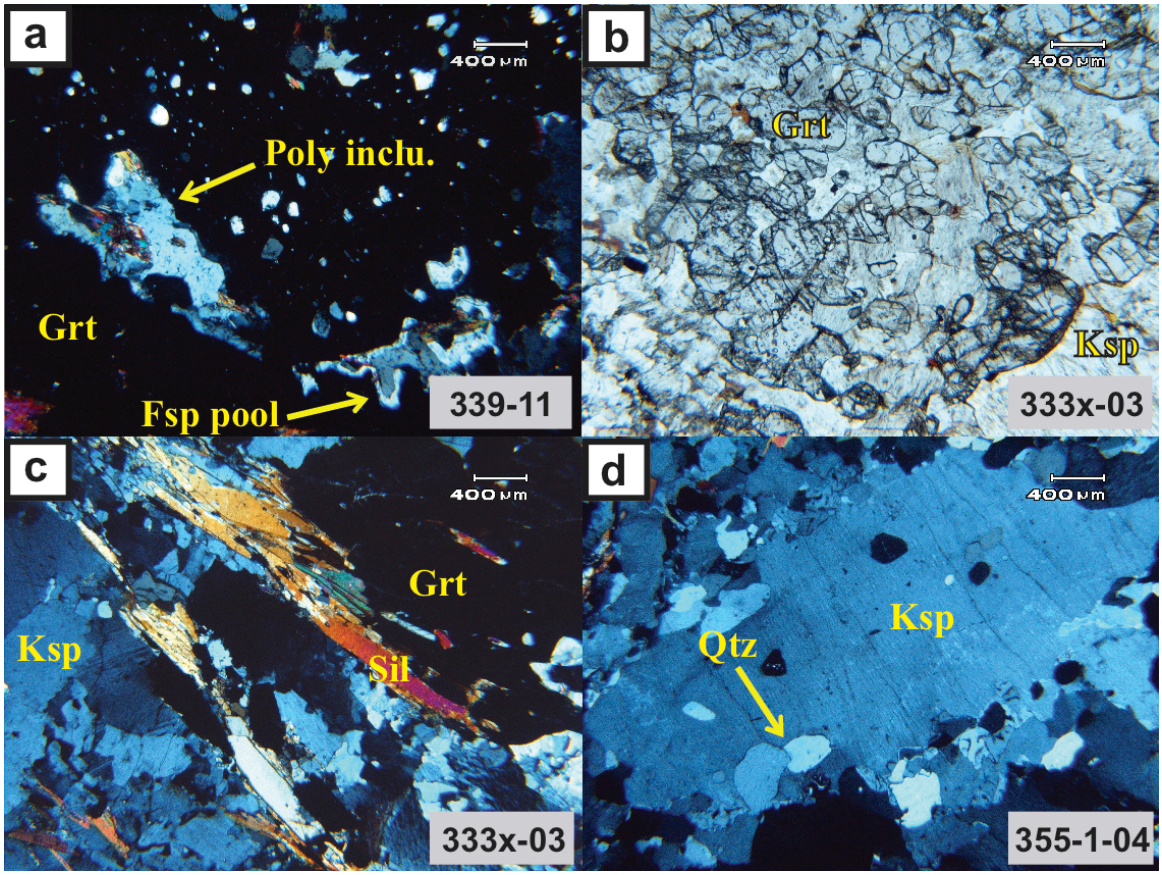

Figure 5.4: Photomicrographs of gneisses with aluminous nodules in a K-feldspar matrix. **(a)** Garnet porphyroblasts with polymineralic inclusions of sillimanite, biotite, plagioclase and quartz in pools of feldspar (XPL); **(b)** nodule made-up of a diffuse small framboidal garnet cluster overgrowing the matrix (PPL); **(c)** sillimanite seams overgrown by garnet (XPL); and **(d)** perthitic K-feldspar with fine exsolution of plagioclase and inclusions of quartz, rimmed by myrmekite (XPL).

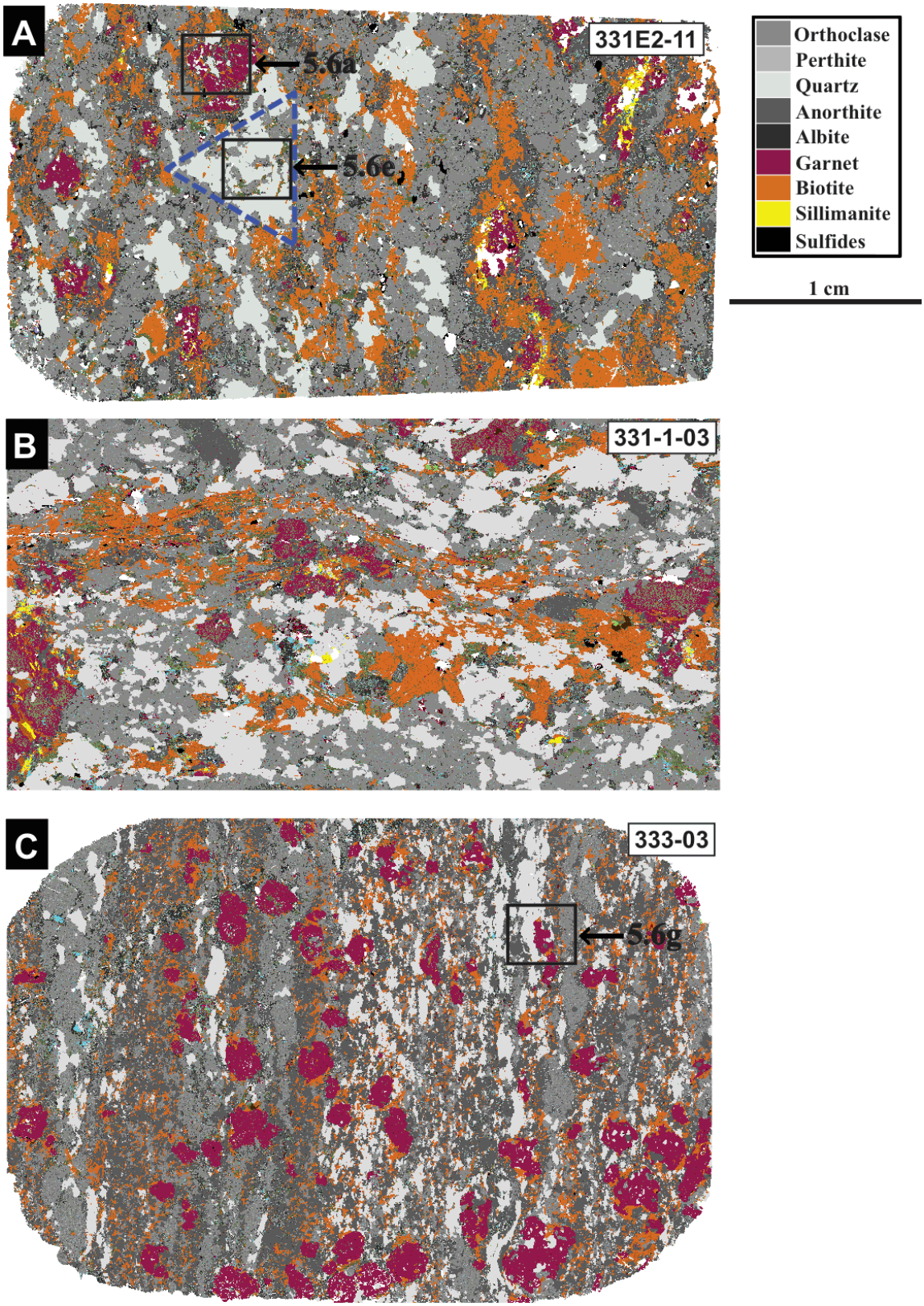

Figure 5.5: SEM-MLA mineral maps of homogeneous aluminous gneisses. **(A)** 331E2-11; **(B)** 331-1-03; and **(C)** 333-03.

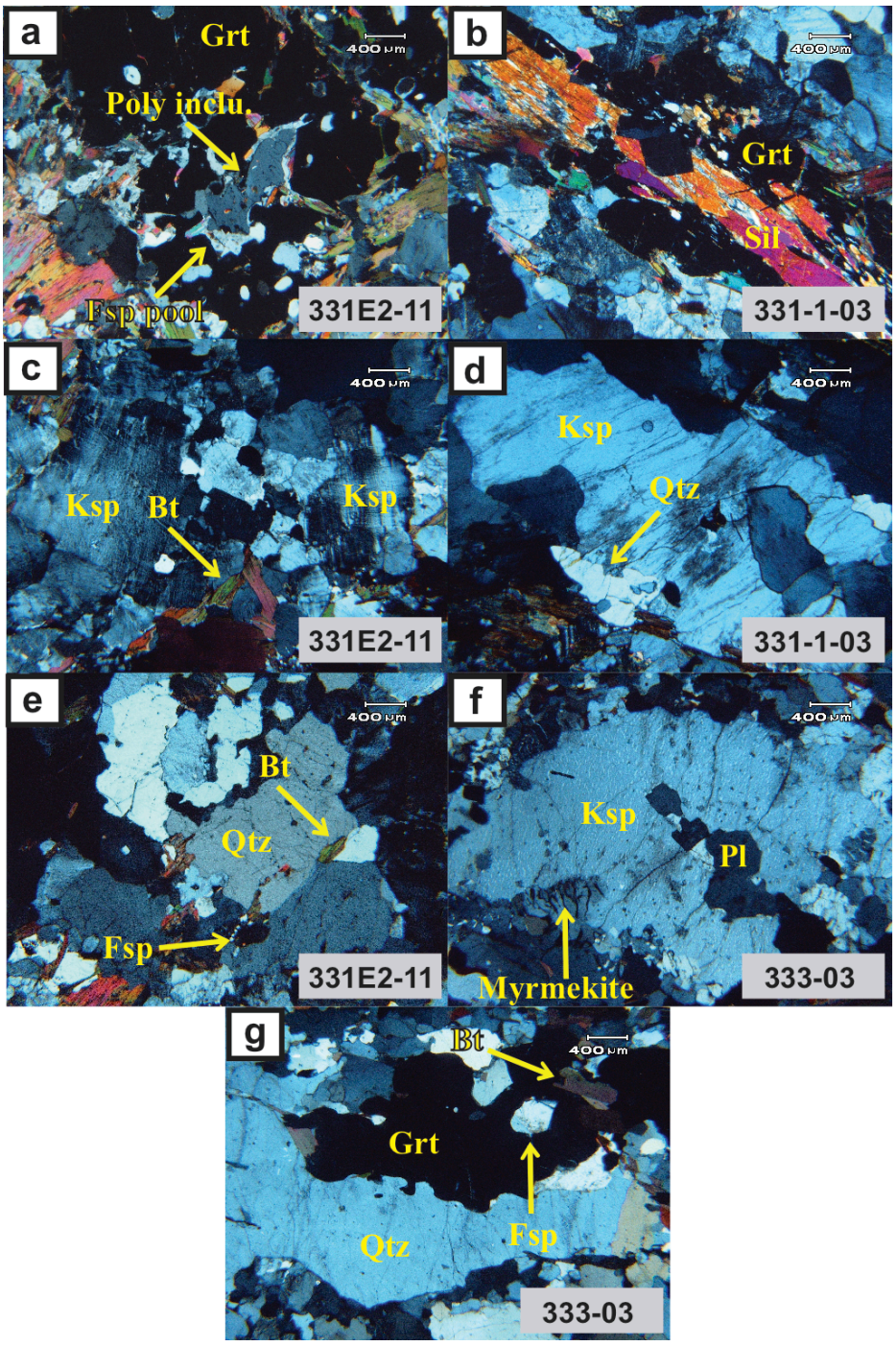

Figure 5.6: Photomicrographs of homogeneous aluminous gneisses. **(a)** Garnet porphyroblasts with polymineralic inclusions of sillimanite, biotite, plagioclase and quartz in pools of feldspar (XPL); **(b)** garnet overgrowing clusters of sillimanite (XPL); **(c)** smaller microcline grains of K-feldspar in the matrix (XPL); **(d)** perthitic K-feldspar with fine exsolution of plagioclase and inclusions of quartz (XPL); **(e)** clusters of quartz aggregates in the matrix with inclusions of feldspar and biotite (XPL; refer to blue triangle Fig. 5.5A); **(f)** perthitic K-feldspar with blebby exsolution of plagioclase and rimmed by myrmekite (XPL); and **(g)** partially recrystallized and resorbed ribbons of quartz with inclusions of biotite and feldspar (XPL).

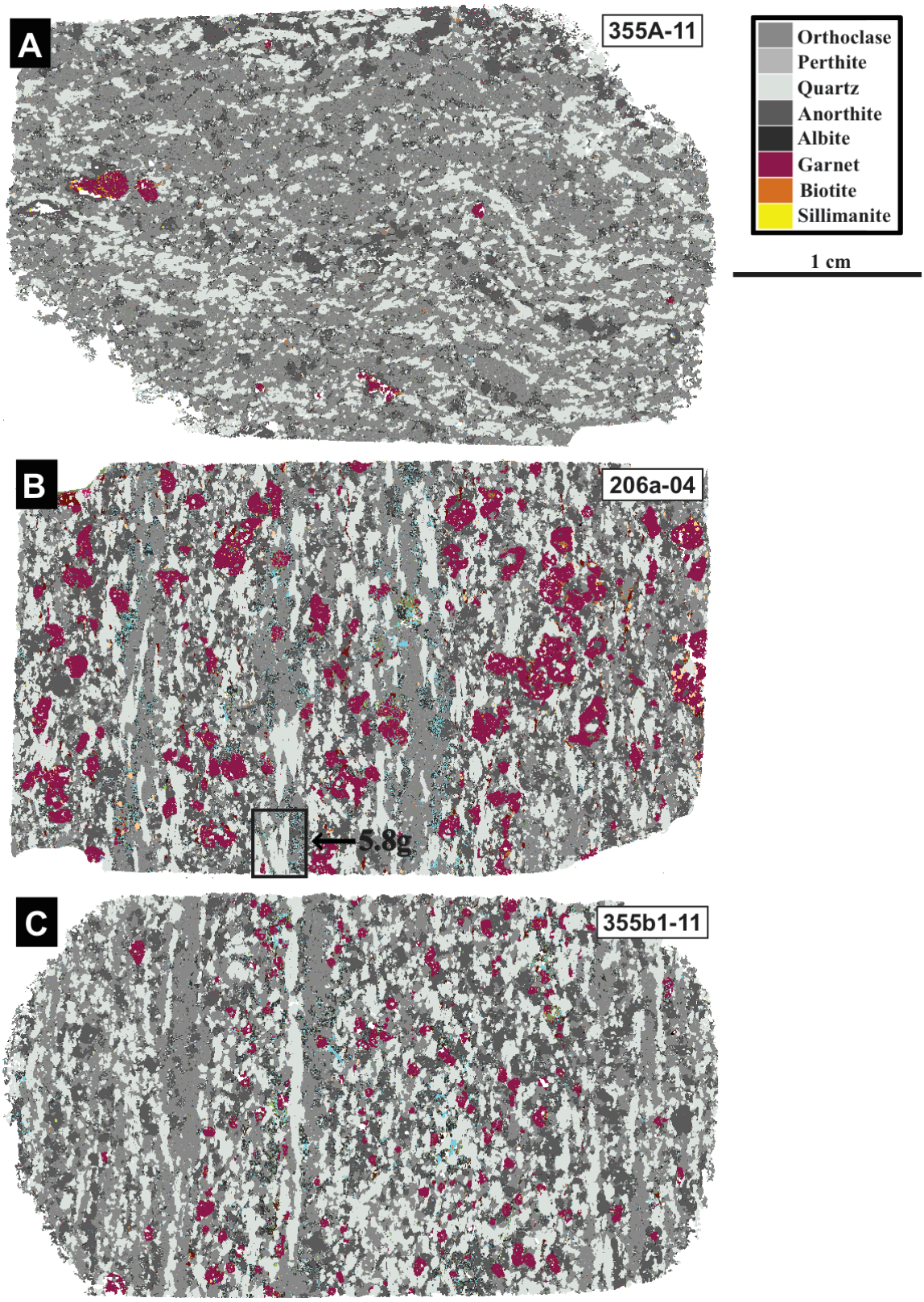

Figure 5.7: SEM-MLA mineral maps of white gneisses. **(A)** 355a-11; **(B)** 206a-04; and **(C)** 355b1-11.

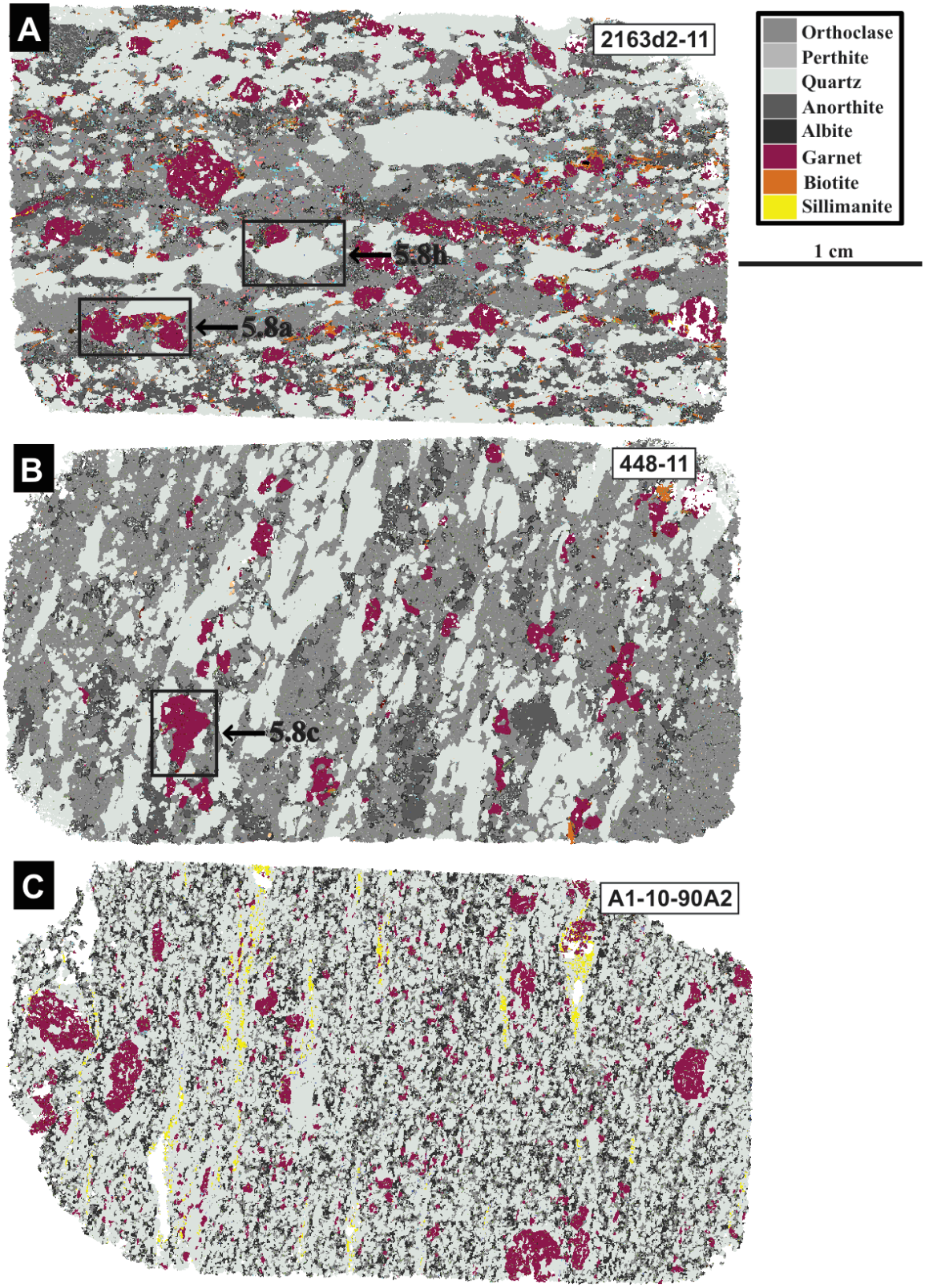

Figure 5.8: SEM-MLA mineral maps of white gneisses. **(A)** 2163d2-11; **(B)** 448-11; and **(C)** A1-10-90A2.

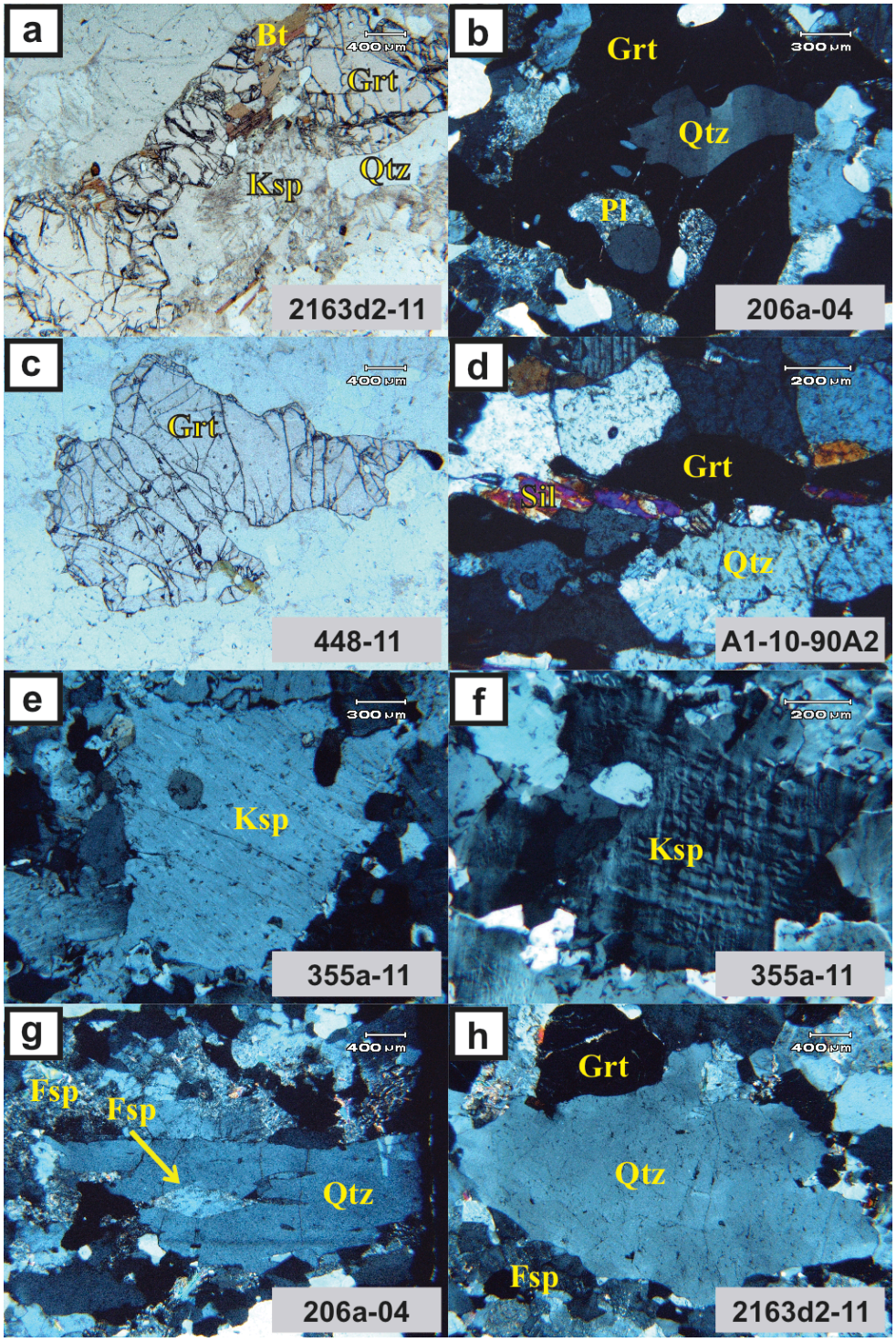

Figure 5.9: Photomicrographs of white gneisses. **(a)** Garnet porphyroblasts aggregated into elongate clusters (PPL); **(b)** garnet porphyroblast with inclusions of plagioclase and quartz in pools of feldspar (XPL); **(c)** pinkish garnet under plane-polarized light (PPL); **(d)** sillimanite rimming garnet (XPL); **(e)** perthitic K-feldspar with blebby or fine exsolution of plagioclase (XPL); **(f)** smaller grains of microcline K-feldspar (XPL); **(g)** discontinuous ribbons of partially recrystallized quartz with inclusions of feldspar (XPL); and **(h)** flattened lensoidal partially recrystallized and resorbed quartz aggregates (XPL).

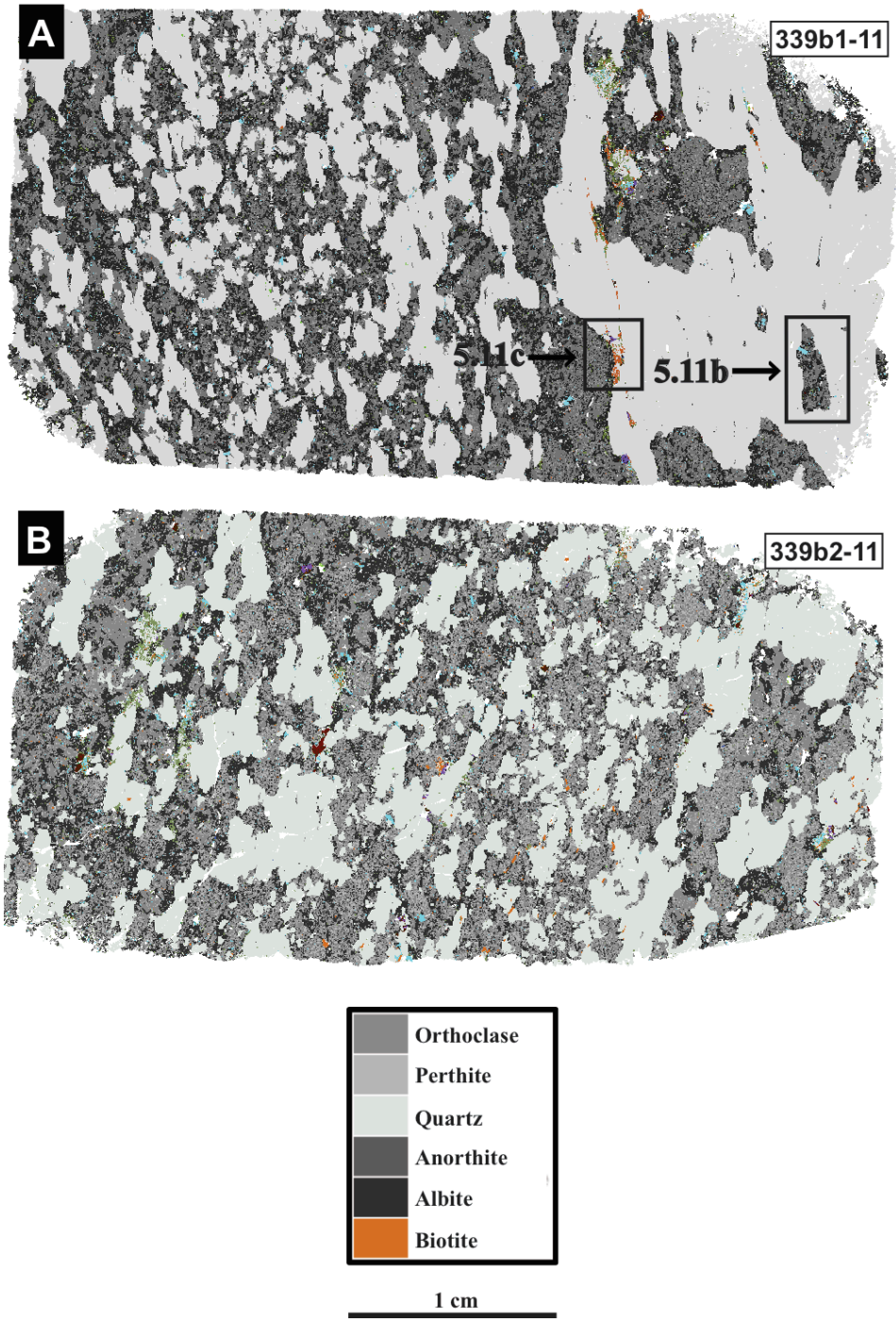

Figure 5.10: SEM-MLA mineral maps of pink gneisses. **(A)** 339b1-11; and **(B)** 339b2-11.

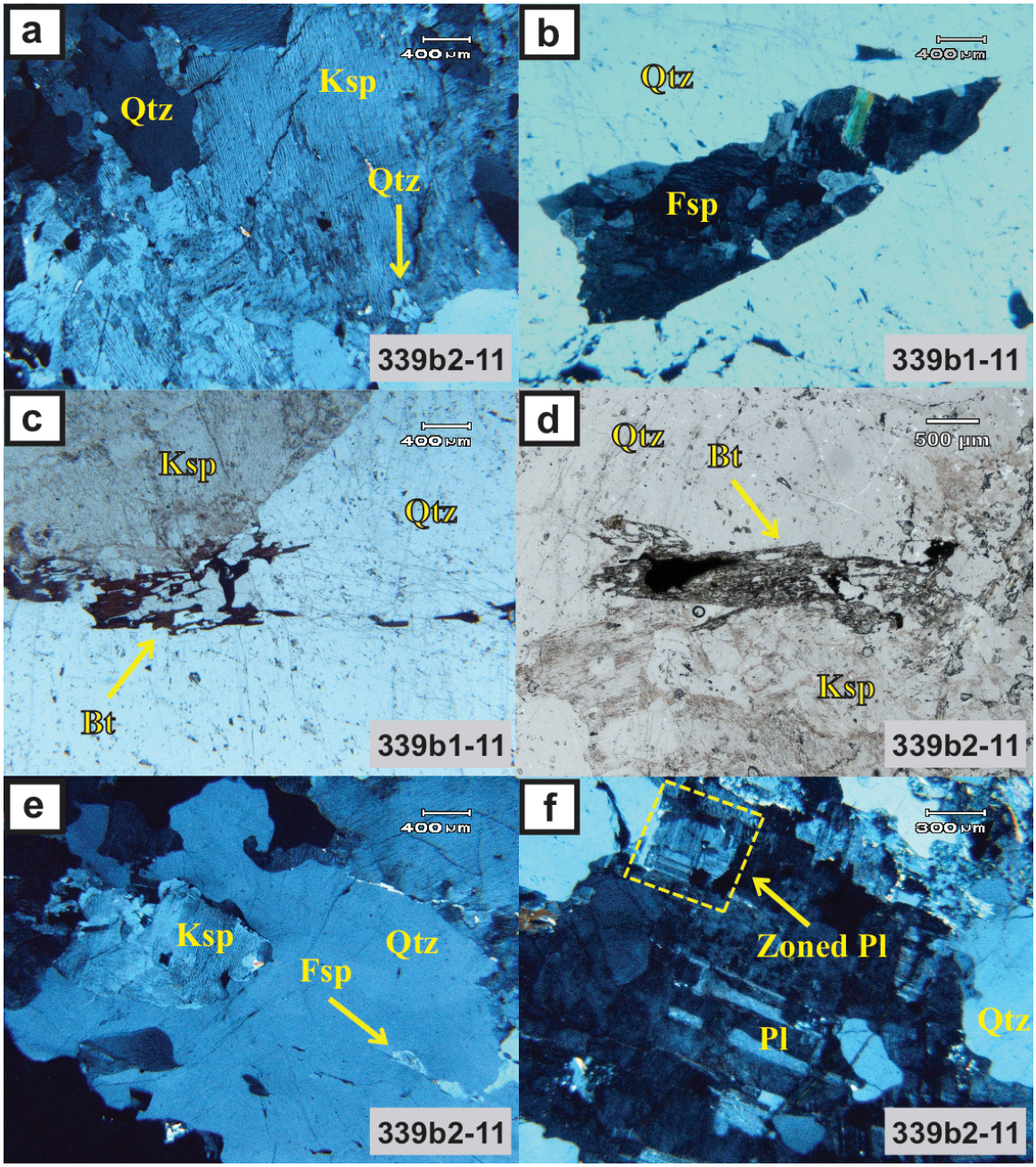

Figure 5.11: Photomicrographs of pink gneisses 339b1-11 and 339b2-11. **(a)** Perthitic K-feldspar with blebby exsolution of plagioclase and inclusions of quartz (XPL); **(b)** branching bands of partially recrystallized quartz with inclusion of feldspar (PPL); **(c, d)** flattened biotite aggregates rimming quartz bands (PPL); **(e)** matrix containing flattened and resorbed quartz aggregates with inclusions of feldspar (XPL); and **(f)** zoned plagioclase (XPL).

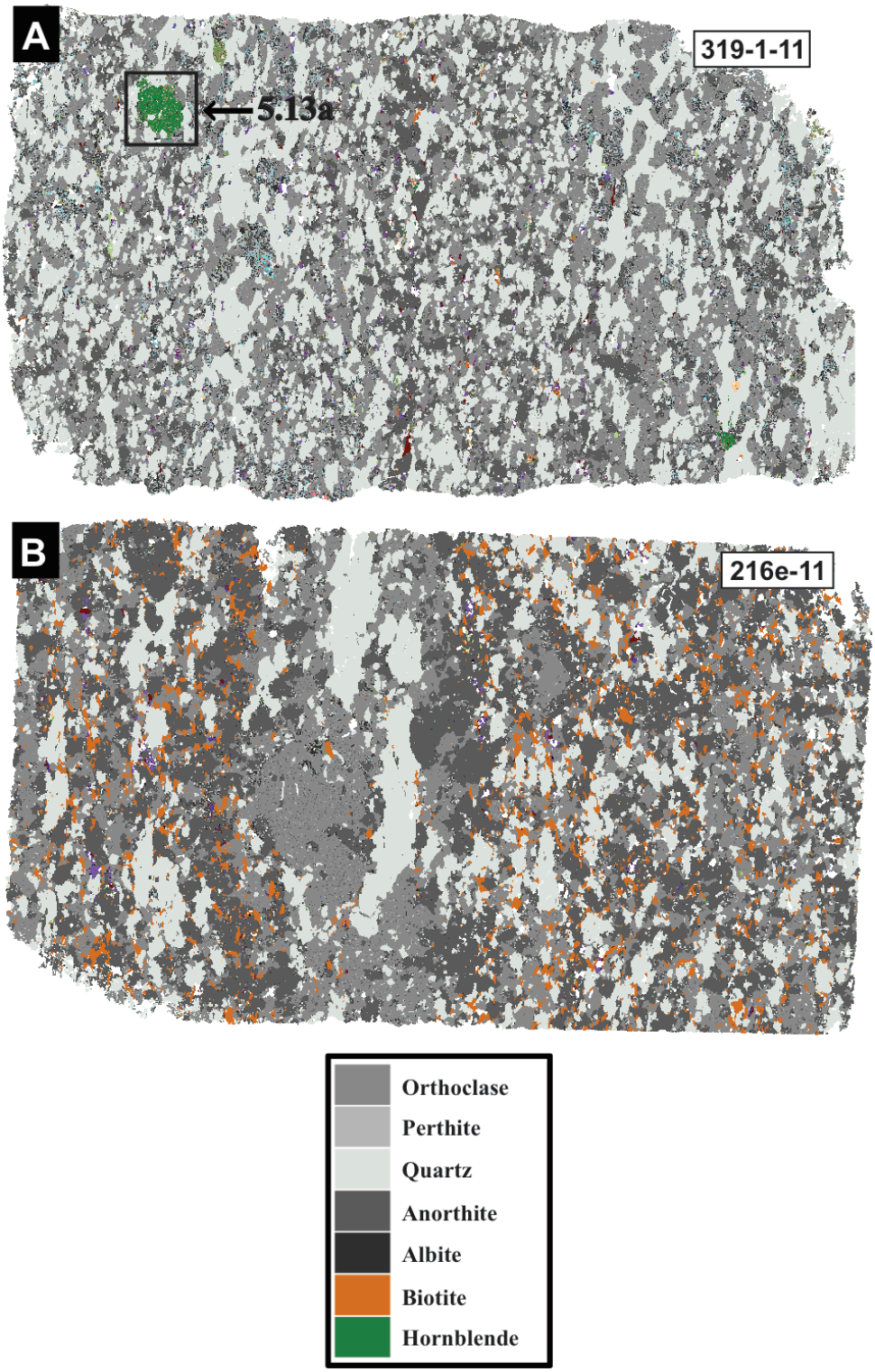

Figure 5.12: SEM-MLA mineral maps of pink gneisses. **(A)** 319-1-11; and **(B)** 216e-11.

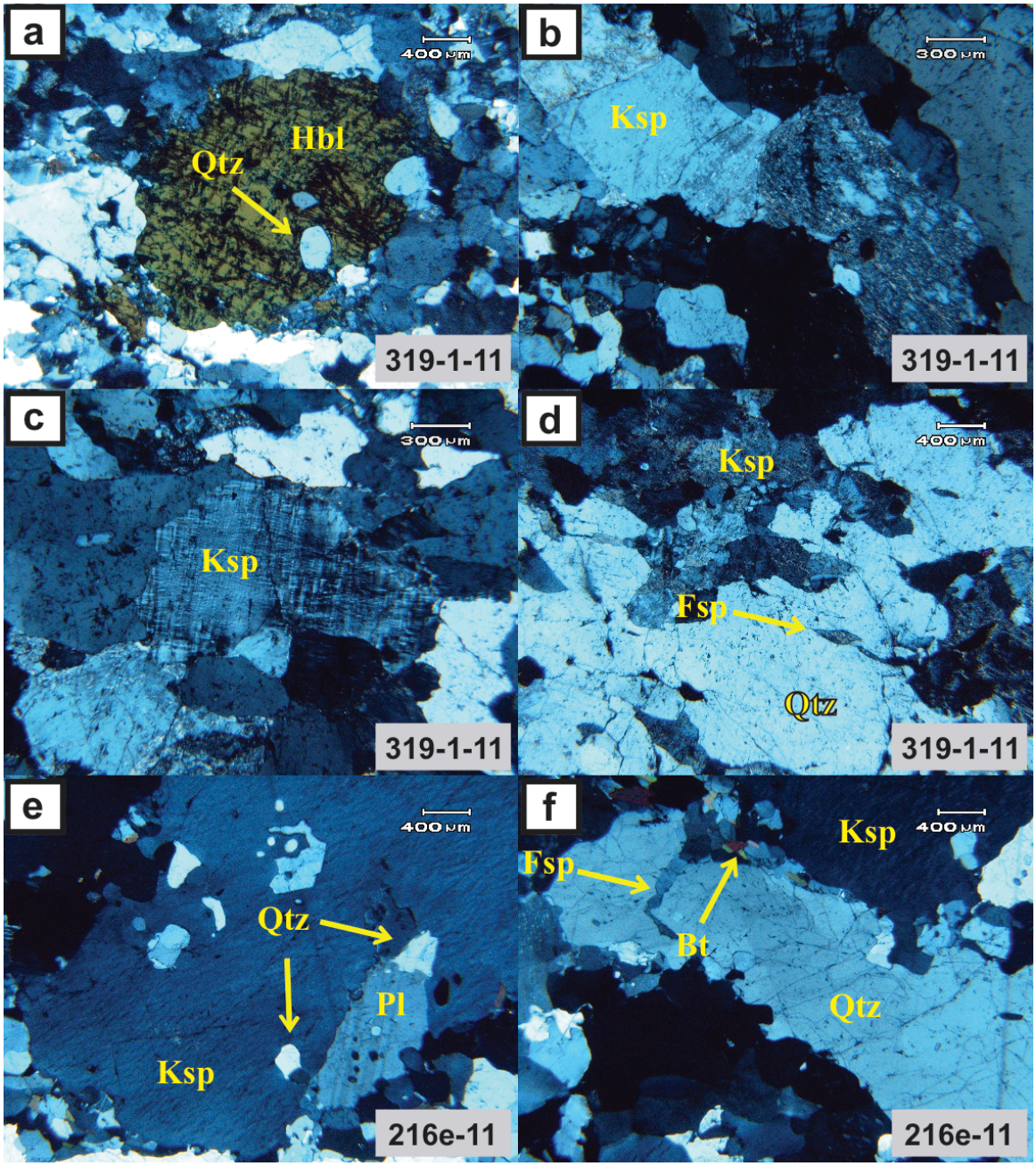

Figure 5.13: Photomicrographs of pink gneisses 319-1-11 and 216e-11. **(a)** Euhdral hornblende porphyroblast with quartz inclusions (XPL); **(b)** perthitic K-feldspar in the matrix (XPL); **(c)** smaller microcline grains of K-feldspar (XPL); **(d)** recrystallized quartz with inclusions of feldspar and corroded by the matrix (XPL); **(e)** perthitic K-feldspar with fine exsolution of plagioclase and inclusions of quartz and plagioclase (XPL); and **(f)** recrystallized quartz ribbons with inclusions of biotite and feldspar (XPL).

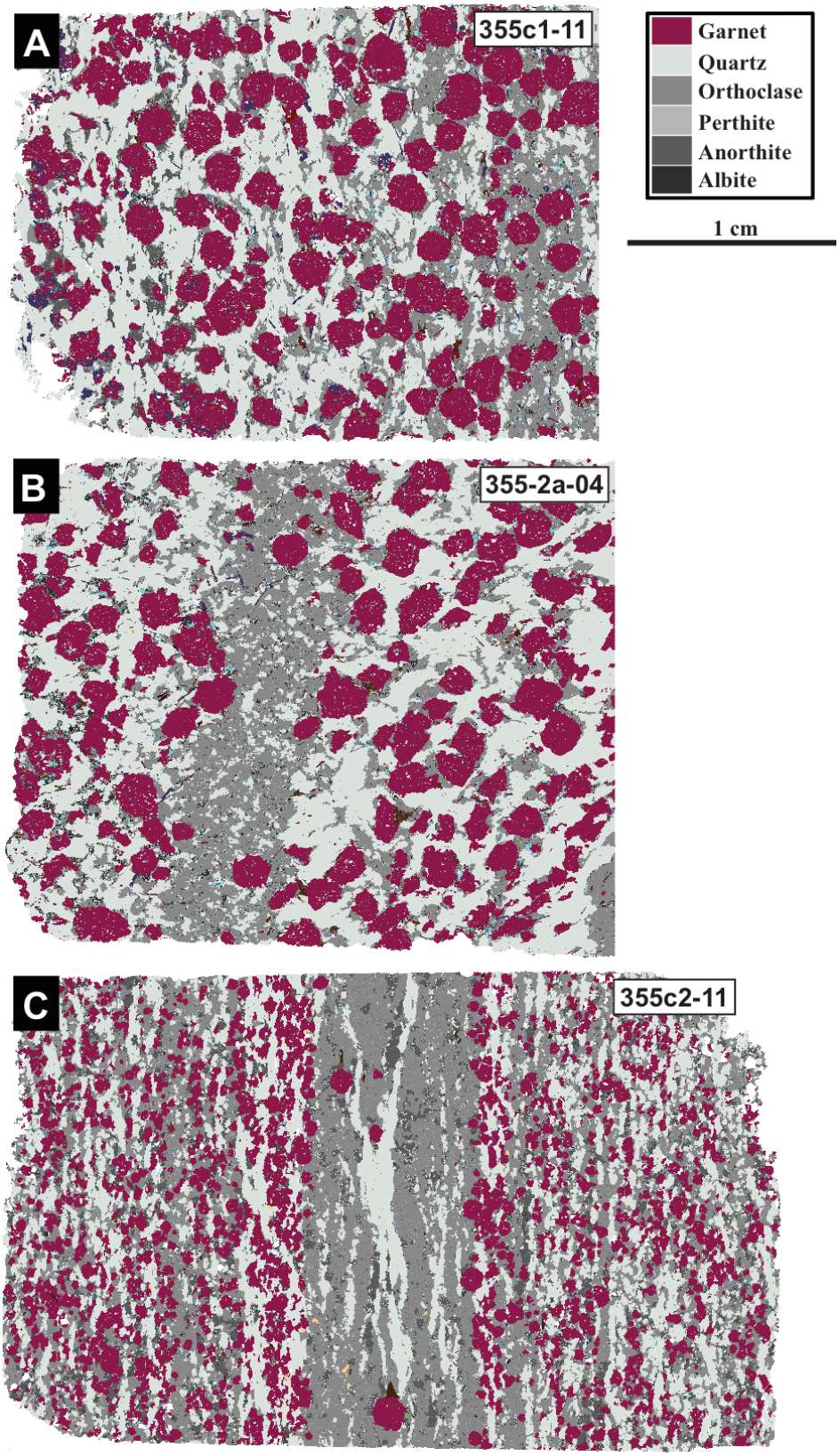

Figure 5.14: SEM-MLA mineral maps of garnetites. **(A)** 355c1-11; **(B)** 355-2a-04; and **(C)** 355c2-11.

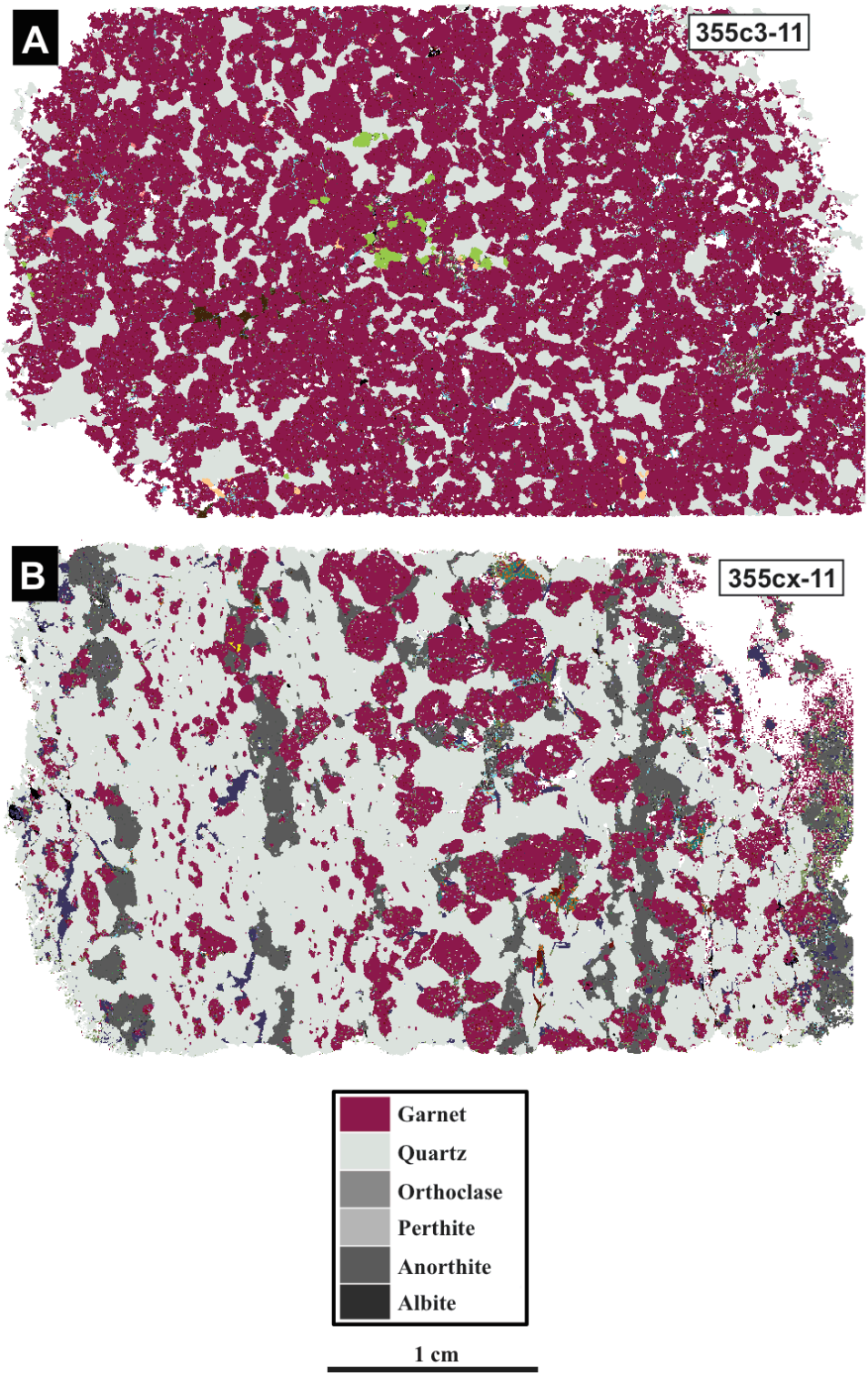

Figure 5.15: SEM-MLA mineral of garnetites. **(A)** 355c3-11; and **(B)** 355cx-11.

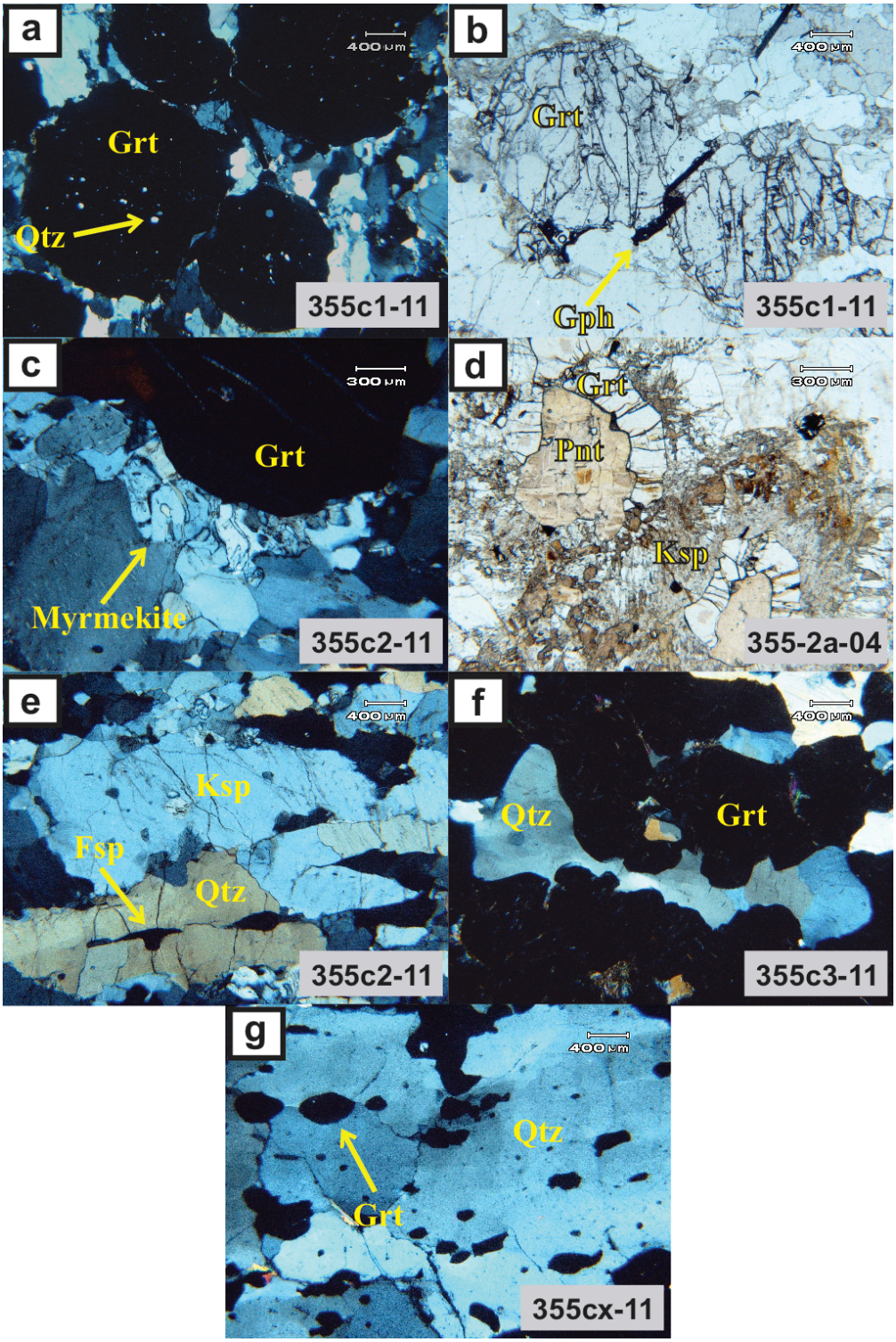

Figure 5.16: Photomicrographs of garnetites. **(a)** Euhedral garnet porphyroblasts tightly packed with tiny inclusions of quartz and plagioclase (XPL); **(b)** graphite rimming garnet (PPL); **(c)** myrmekite rimming garnet (XPL); **(d)** altered layers of K-feldspar with overgrowths of pinnite by garnet (PPL); **(e)** discontinuous branching ribbons of partially recrystallized quartz with inclusions of feldspar (XPL); **(f)** interstitial recrystallized quartz matrix (XPL); and **(g)** quartz-bearing layers with round inclusions of garnet (XPL).

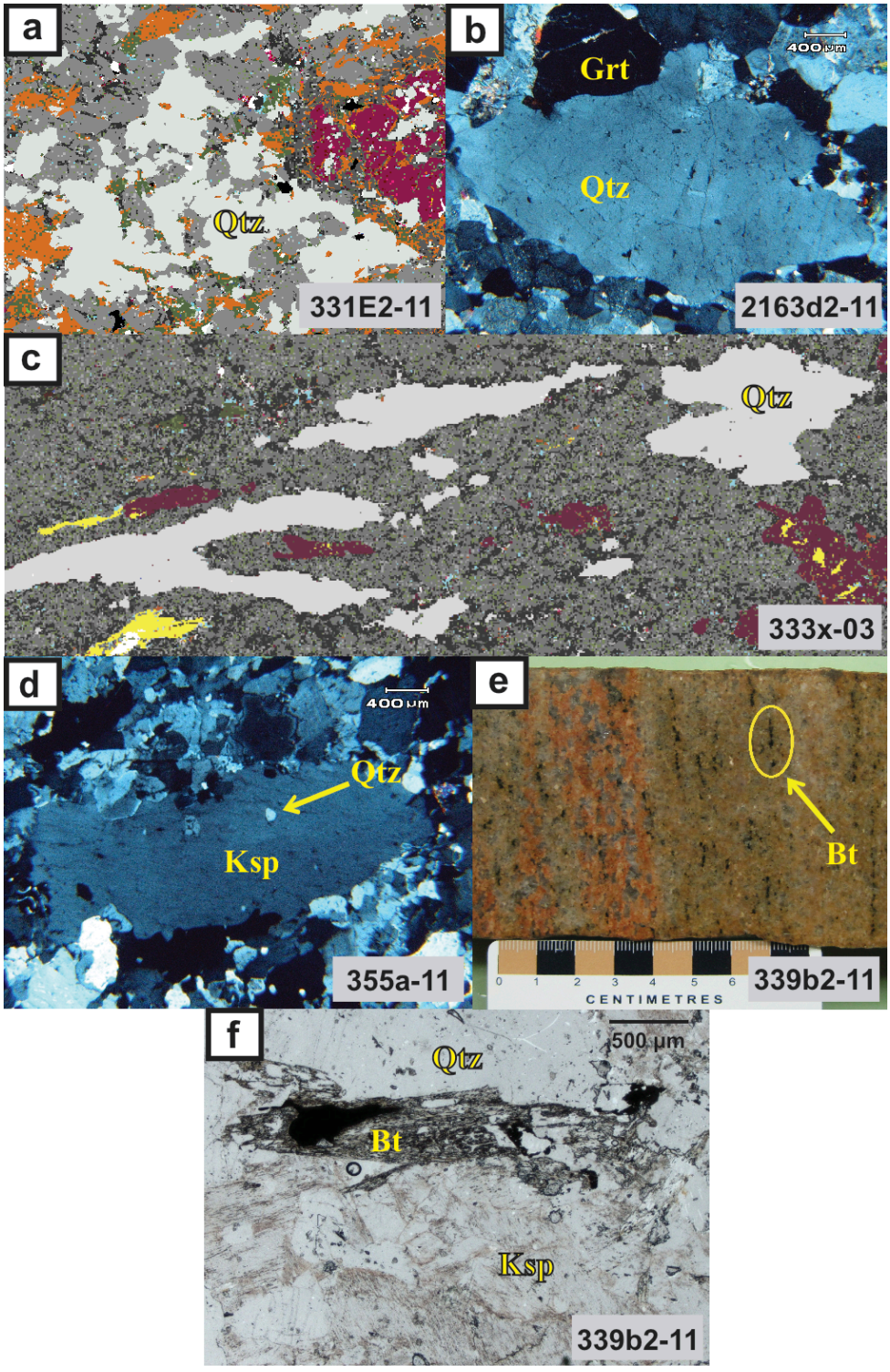

Figure 5.17: Relict textures diagnostic of the protolith. **(a)** Bipyramidal clusters of quartz phenocrysts; **(b)** flattened lenticular quartz phenocrysts deflected around garnet and corroded by the matrix (XPL); **(c)** flattened angular quartz phenocrysts corroded by the matrix; **(d)** large perthitic K-feldspar phenocrysts with quartz inclusions; and **(e, f)** specks of flattened biotite aggregates resembling metamorphosed volcanic ashes in hand specimen and at the thin section scale (PPL).

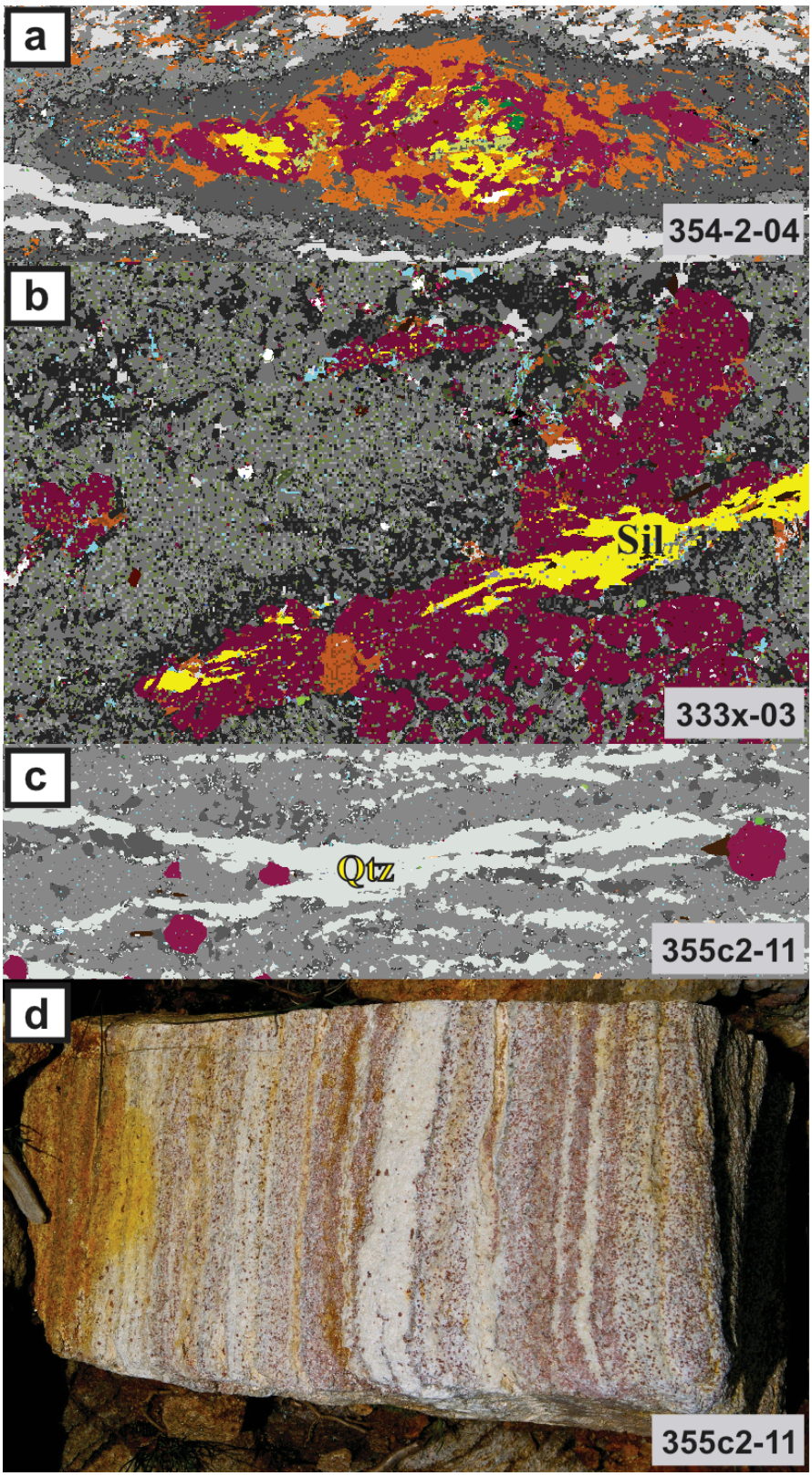

Figure 5.18: Features diagnostic of pre-metamorphic hydrothermal alteration. **(a)** Aluminous nodules; **(b)** discontinuous sillimanite seams; **(c)** concordant quartz veins; and **(d)** garnetitization of the white gneiss.

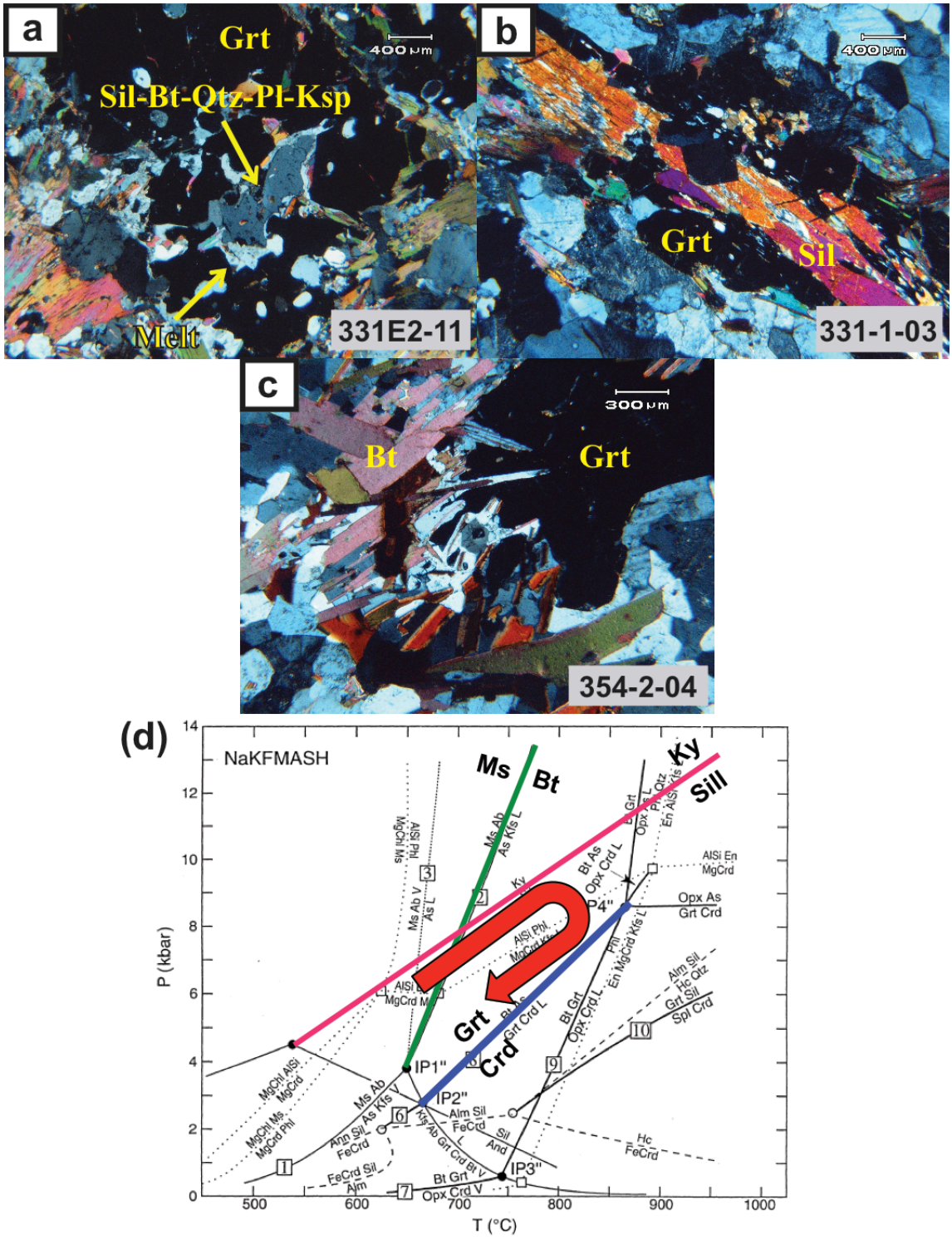

Figure 5.19: Textures related to granulite-facies metamorphism and partial melting in the aluminous gneisses. **(a)** Garnet with inclusions of Sill-Bt-Qtz-Pl-Ksp in pools of former melt (XPL); **(b)** evidence of prograde metamorphism from sillimanite overgrown by garnet (XPL); **(c)** evidence of retrograde metamorphism from biotite corroding rims of garnet (XPL); and **(d)** a schematic P-T path based on mineral assemblage and textural evidence of partial melting in the aluminous gneisses (modified after Spear *et al.* 1999).

Chapter 6: MINERAL CHEMISTRY

6.1 INTRODUCTION

The compositions of garnet, biotite, spinel, and feldspars from representative samples of the aluminous gneisses, white gneisses, and garnetites of the LBS were acquired by electron probe micro-analyzer (EPMA; refer to Appendix A) to:

(i) compare mineral chemistries within and among the three suites of rock types listed above; and

(ii) determine any unusual proportions of constituents, which could be associated with hydrothermal fluids (i.e. Mn, Ba, F, Cl or Sr).

6.2 GARNET

The compositions of garnet were determined in 12 samples, and are listed in Table 6.1-6.2 in terms of Sps, Alm, Prp, And, Grs components and X(Fe^{2+}). Zoning profiles of individual grains of garnet with diameters of approximately 1 to 5 mm are shown in Figures. 6.1-6.3. In addition, ternary plots using average composition parameters are shown in Figure. 6.4.

In all lithologies, garnet grains are chemically homogeneous except for a variable increase in Alm and decrease in Prp at the rims (Figs. 6.1-6.3). These patterns are consistent with diffusional homogenization of garnet under high-*T* metamorphic conditions followed by partial re-equilibration of the rims with another ferromagnesian phase (i.e. biotite) during retrogression (Spear *et al.* 1999). However, there are compositional variations in garnet both within and between the three rock types.

The composition of garnet falls within the following ranges:

(a) [$Sps_{1-5}Alm_{48-75}Prp_{15-37}And_{3-7}Grs_{0-7}$], with $X(Fe^{2+})_{0.59-0.83}$ in aluminous gneisses;

(b) [$Sps_{1-4}Alm_{49-52}Prp_{21-46}And_{5-9}Grs_{0-4}$], with $X(Fe^{2+})_{0.52-0.76}$ in white gneisses; and

(c) [$Sps_{1-16}Alm_{50-68}Prp_{5-33}And_{5-8}Grs_{0-22}$], with $X(Fe^{2+})_{0.63-0.93}$ in the garnetites.

Among the aluminous gneisses, garnet has the highest Sps, Alm, and And+Grs contents in the spinel-bearing and the homogeneous varieties, and highest Prp contents in the nodular gneiss *333-2-03* (Fig. 6.4). Sps and And contents of garnet in the white gneisses are inversely correlated with the modal amount of garnet in the rocks (*355a-11*). In contrast, Prp contents are the highest in garnets from the sample with the highest garnet mode (*2163d2-11;* Fig. 6.4). Garnet in the garnetites has the highest Alm contents in the layered sample *355-2-04*, and the highest Sps, Prp, and Grs contents in *355c3-11* and *355c2-11* (Fig. 6.4), which represent a massive and layered portion of the same rock. And content is the highest in garnets from the quartz-rich sample *355cx-11*.

Overall, the data shows that although there is significant overlap in the composition ranges of garnet for the three rock types, there are also some notable differences, with: (a) garnet from aluminous and white gneisses reaching the highest Alm and Prp contents respectively; and (b) garnet from the garnetites being clearly the most rich in Sps and, in some cases, Grs. More commonly, garnet-rich rocks are formed by Mn and Fe carried in high-temperature hydrothermal fluids containing high amounts of CO_2 under reduced conditions, and where Mn is deposited either proximal or distal to a hydrothermal vent under relatively oxidized conditions (Borchert 1980; Sry and Wonder 1989; Heimann *et al.* 2011). The combination of relatively higher contents of Sps in garnet for these garnet-rich rocks at high-grade metamorphic conditions is indicative and inferred the result of hydrothermal fluid activity.

6.3 BIOTITE

The compositions of biotite (a) included in garnet; (b) rimming garnet; and (c) interstitial in the matrix, were determined in six samples of aluminous and white gneisses. Compositional ranges in terms of X(Mg), Ti, Al^{VI}, Ba, F and Cl are listed in Table 6.3, and plots of Ti-X(Mg) and Ti-Al^{VI} are shown in Figures. 6.5-6.6.

The compositions of biotite in terms of X(Mg), Ti, Al^{VI} fall in the range $[X(Mg)_{0.50\text{-}0.74}Ti_{0.23\text{-}0.70}Al^{VI}_{0.14\text{-}0.76}]$ in the aluminous gneisses, and $[X(Mg)_{0.58\text{-}0.72}Ti_{0.33\text{-}0.56}Al^{VI}_{0.20\text{-}0.42}]$ in the one white gneiss sample *2163d2-11*. Ti is inversely correlated with X(Mg) and Al^{VI} in the biotite of the aluminous gneisses, but shows a positive correlation in biotite of the white gneiss (Figs. 6.5-6.6). In the spinel-bearing aluminous gneiss *354-2-04*, interstitial biotite in the matrix exhibits high contents of Ti (Fig. 6.5a), whereas X(Mg) and Al^{VI} are highest in grains included in or rimming garnet.

Ba, F and Cl contents of biotite per formula unit are $[Ba_{0\text{-}2.3}F_{1.4\text{-}36}Cl_{0.06\text{-}12}]$ in the aluminous gneisses, and $[Ba_{0.01\text{-}1.4}F_{1.4\text{-}17}Cl_{2.2\text{-}11}]$ in the white gneiss. Ba and F contents are highest in biotite included within garnet in the nodular aluminous gneiss *333-2-03*. The contents of F and Cl in matrix grains are highest in homogeneous aluminous gneisses (*331E2-11*, *333-03*) and the white gneiss *2163d2-11*.

6.4 SPINEL

Spinel was analyzed in the two spinel-bearing nodular aluminous gneisses *354-2-04* and *10-A1-76*. Its composition is listed in Table 6.4 in terms of Spl, X(Hc), Gah, X(Mag), and is plotted in ternary diagrams shown in Figure. 6.7.

The composition of spinel is in the range $[Spl_{13\text{-}19}X(Hc)_{55\text{-}65}Gah_{7\text{-}27}X(Mag)_{0.4\text{-}2}]$ and shows the following trends:

(a) Gah contents are the highest in spinel inclusions within the largest garnets of *354-2-04* (Figs. 6.7a-6.7c);

(b) X(Hc) and Spl contents are the highest in spinel of sample *10-A1-76* (Figs. 6.7a, 6.7c); and

(c) spinel in both samples have very low contents of X(Mag).

The contents of Zn in spinel inclusions for both samples are slightly elevated compared to typical Fe-bearing spinel found in granulite-facies rocks. Garnet-rich rocks at Broken Hill contain the highest contents of Zn, but this is dependent upon whether another phase is present in the same rock (e.g. gahnite) that can substitute Zn into the garnet structure (Spry and Wonder 1989; Spry *et al.* 2007; Heimann *et al.* 2011). Zn contents in spinel inclusions for these samples are inferred similar to the Zn-bearing garnetite rocks at Broken Hill, however, this interpretation is with caution as the content of Zn for these spinel inclusions have a very low amounts in comparison to typical Zn spinel formed in VMS environments (Spry *et al.* 2007).

6.5 FELDSPARS

Alkali feldspar and plagioclase adjacent to garnet and/ or interstitial grains in the matrix were analyzed in 12 samples of aluminous gneisses, white gneisses, and garnetites. Compositional ranges in terms of orthoclase (Or), albite (Ab), anorthite (An), Ba and Sr contents are listed in Tables 6.5-6.6, and ternary Or-An-Ab diagrams are shown in Figure. 6.8.

6.5.1 K-feldspar

The compositional ranges of K-feldspar in terms of Or, Ab and An overlaps substantially among the three types of rocks (Table 6.5):

(a) $[Or_{76\text{-}93}Ab_{5\text{-}24}An_{0.1\text{-}2}]$ in the aluminous gneisses;

(b) $[Or_{81\text{-}94}Ab_{5\text{-}18}An_{0.3\text{-}1}]$ in the white gneisses; and

(c) $[Or_{79\text{-}92}Ab_{1\text{-}21}An_{0.1\text{-}0.6}]$ in the garnetites.

However, the white gneiss *206a-04*, has a distinctively higher average Or content than the rest (Fig. 6.8). At the thin section scale, in all the three rock types, K-feldspar adjacent to garnet shows the highest Or contents. In general, the matrix of these rock types observed from maps by SEM-MLA imagining have a dominant feldspar composition of Or (refer to Figs. 5.1, 5.3, 5.5, 5.7, and 5.8).

Ba and Sr contents of K-feldspar fall in the ranges $[Ba_{0.04\text{-}0.17}Sr_{0.03\text{-}0.07}]$ in the aluminous gneisses, $[Ba_{0.01\text{-}0.11}Sr_{0.03\text{-}0.06}]$ in the white gneisses, and $[Ba_{0.02\text{-}0.14}Sr_{0.04\text{-}0.14}]$ in the garnetites (Table 6.5). The content of Ba is highest in the homogeneous aluminous gneiss *333-03*, the white gneiss *206a-04*, and the garnetites *355-2a-04*, *355c2-11*. The highest parts of these ranges are unusual, and may attest to the effects of hydrothermal fluids.

6.5.2 Plagioclase

The composition ranges of plagioclase in terms of Or, Ab and An are (Table 6.6):

(a) $[Or_{0.6\text{-}3}Ab_{68\text{-}90}An_{8\text{-}27}]$ in the aluminous gneisses;

(b) $[Or_{0.7\text{-}2}Ab_{64\text{-}75}An_{25\text{-}35}]$ in the white gneisses; and

(c) $[Or_{0.7\text{-}2.7}Ab_{68\text{-}75}An_{25\text{-}32}]$ in the garnetites.

As shown in Figure. 6.8, the average values of Ab are higher in aluminous gneisses, whereas those of plagioclase in garnetites are towards the lower or Ab end. For all cases, plagioclase tends to be richest in An with proximity to garnet. The increase in An with proximity to garnet is consistent with maps from SEM-MLA imaging for the aluminous gneisses, where the more nodular garnets are seen mantled by plagioclase of

An composition and becoming Ab towards the rim (refer to Fig. 5.1A). In addition, Ba and Sr contents of plagioclase among the three rocks types are in the range [$Ba_{0-0.07}Sr_{0.02-0.06}$], and much lower relative to those of K-feldspar (Table 6.6).

6.6 DISCUSSION

The key points revealed by the mineral chemistry of garnet, biotite, spinel, K-feldspar and plagioclase in aluminous gneisses, white gneisses, and garnetites of the LBS are the following:

(a) in all lithologies, garnet zoning profiles show consistent diffusional homogenization during high-*T* metamorphism followed by retrograde resetting of Fe and Mg at the rims;

(b) garnet is most Fe-rich in the aluminous gneisses, most Mg-rich in white gneisses, and most Mn-rich (and in some cases Ca-rich) in the garnetites; and

(c) K-feldspar and plagioclase adjacent to garnet in all lithologies are the richest in Or and An contents, respectively.

In addition, there are several observations compatible with the interpretation of pre-metamorphic hydrothermal alteration. These include the relatively high contents of:

(a) Mn and Ca in garnet of the garnetites;

(b) Zn in spinel of the nodular aluminous gneisses;

(c) Ba and F in biotite of the nodular aluminous gneisses; and

(d) Ba in K-feldspar from some homogeneous aluminous gneisses, white gneisses, and garnetites.

Table 6.1: Compositional ranges of garnet in terms of Sps, Alm, Prp, And, Grs, and $X(Fe^{2+})$.

Garnet Compositional Ranges

Aluminous Gneisses	**Sps**	**Alm**	**Prp**	**And**	**Grs**	**$X(Fe^{2+})$***
354-2-04 (cores)	0.018-0.024	0.711-0.735	0.189-0.245	0.046	0.005	0.740-0.795
354-2-04 (rims)	0.021-0.026	0.729-0.746	0.150-0.209	0.047	0.004-0.030	0.777-0.832
354-2-04 (grt 2)	0.023-0.029	0.721-0.743	0.164-0.227	0.047	0.000-0.016	0.761-0.819
331E2-11 (grt 1)	0.019-0.031	0.640-0.680	0.205-0.291	0.076	0.001-0.036	0.688-0.761
331E2-11 (grt 2)	0.010-0.029	0.623-0.665	0.232-0.371	0.075	0.007	0.627-0.738
333-03 (grt 1)	0.015-0.018	0.599-0.620	0.308-0.354	0.057	0.000	0.634-0.668
333-03 (grt 2)	0.016-0.019	0.608-0.623	0.294-0.338	0.057	0.000-0.014	0.648-0.679
333-03 (grt 3)	0.018-0.024	0.613-0.645	0.202-0.317	0.058	0.001-0.069	0.660-0.761
333-2-03 (grt 1)	0.012-0.017	0.593-0.621	0.282-0.353	0.066	0.000-0.011	0.628-0.688
333-2-03 (grt 2)	0.012-0.014	0.581-0.597	0.340-0.373	0.065	0.001	0.614-0.631
10-A1-76 (grt 1)	0.045-0.048	0.643-0.651	0.231-0.246	0.064	0.001-0.006	0.723-0.738
10-A1-76 (grt 2)	0.044-0.049	0.645-0.659	0.223-0.252	0.064	0.001-0.013	0.720-0.745
White Gneisses	**Sps**	**Alm**	**Prp**	**And**	**Grs**	**$X(Fe^{2+})$***
355A-11	0.032-0.041	0.582-0.607	0.263-0.332	0.087	0.000	0.639-0.697
206a-04 (grt 1)	0.015-0.017	0.658-0.671	0.232-0.248	0.065	0.001-0.027	0.728-0.740
206a-04 (grt 2)	0.016-0.019	0.662-0.675	0.210-0.247	0.066	0.008-0.032	0.729-0.762
2163d2-11 (grt 1)	0.006-0.009	0.498-0.515	0.393-0.460	0.054	0.000-0.016	0.523-0.566
2163d2-11 (grt 2)	0.006-0.008	0.499-0.520	0.389-0.456	0.054	0.000-0.042	0.524-0.566
Garnetites	**Sps**	**Alm**	**Prp**	**And**	**Grs**	**$X(Fe^{2+})$***
355-2a-04 (grt 1)	0.063-0.067	0.663-0.668	0.200-0.212	0.053	0.001-0.020	0.758-0.768
355-2a-04 (grt 2)	0.062-0.065	0.660-0.670	0.208-0.216	0.053	0.001-0.015	0.755-0.763
355c2-11 (grt 1)	0.152-0.156	0.508-0.512	0.259-0.273	0.073	0.000-0.003	0.652-0.663
355c2-11 (grt 2)	0.153-0.160	0.512-0.527	0.258-0.282	0.074	0.000	0.652-0.667
355c3-11 (cores)	0.089-0.092	0.603-0.613	0.149-0.164	0.080	0.054-0.073	0.787-0.805
355c3-11 (rims)	0.089-0.101	0.593-0.668	0.143-0.182	0.811	0.006-0.090	0.782-0.809
355cx-11 (grt 1)	0.042-0.046	0.565-0.577	0.265-0.329	0.092	0.020	0.634-0.685
355cx-11 (grt 2)	0.041-0.044	0.563-0.574	0.315-0.330	0.092	0.000	0.633-0.643

$X(Fe^{2+})$* = $[Fe^{2+}/(Fe^{2+}+Mg)]$

Table 6.2: Average compositions of garnet in terms of Sps, Alm, Prp, And, Grs, and $X(Fe^{2+})$.

Average Garnet Composition

Aluminous Gneisses	**Sps**	**Alm**	**Prp**	**And**	**Grs**	**$X(Fe^{2+})$***
354-2-04 (includ. cores)	0.024	0.726	0.213	0.047	0.001	0.773
331E2-11	0.022	0.649	0.274	0.076	0.001	0.704
333-03	0.018	0.614	0.316	0.057	0.003	0.661
333-2-03	0.013	0.598	0.344	0.066	0.001	0.635
10-A1-76	0.046	0.650	0.238	0.064	0.004	0.732
White Gneisses	**Sps**	**Alm**	**Prp**	**And**	**Grs**	**$X(Fe^{2+})$***
355A-11	0.034	0.589	0.321	0.087	0.000	0.647
206a-04	0.016	0.665	0.237	0.065	0.016	0.737
2163d2-11	0.007	0.505	0.437	0.054	0.005	0.536
Garnetites	**Sps**	**Alm**	**Prp**	**And**	**Grs**	**$X(Fe^{2+})$***
355-2a-04	0.064	0.664	0.210	0.053	0.009	0.760
355c2-11	0.155	0.515	0.268	0.073	0.000	0.658
355c3-11 (cores)	0.091	0.608	0.158	0.080	0.063	0.793
355cx-11	0.043	0.570	0.319	0.092	0.001	0.641

$X(Fe^{2+})$* = $[Fe^{2+}/(Fe^{2+}+Mg)]$

Table 6.3: Compositional ranges of biotite in terms of X(Mg) ratios, Ti and Al^{VI}, Ba, F and Cl.

Aluminous Gneisses

354-2-04	**X(Mg)***	**Ti**	**Al^{vi}**	**Ba**	**F**	**Cl**
(included in grt)	0.615-0.660	0.291-0.415	0.357-0.598	0.000-0.003	0.158-0.330	0.010-0.014
(around grt rim)	0.573-0.596	0.344-0.434	0.484-0.659	0.000-0.008	0.137-0.208	0.006-0.011
(matrix)	0.515-0.529	0.553-0.648	0.278-0.337	0.001-0.009	0.078-0.256	0.011-0.022
331E2-11						
(included in grt)	0.554-0.574	0.375-0.419	0.481-0.596	0.000-0.006	0.022-0.134	0.069-0.084
(around grt rim)	0.544-0.644	0.235-0.441	0.405-0.645	0.001-0.007	0.006-0.128	0.077-0.093
(matrix)	0.548-0.592	0.338-0.448	0.368-0.751	0.000-0.011	0.000-0.140	0.061-0.092
333-03						
(included in grt)	0.698-0.739	0.413-0.698	0.144-0.366	0.009-0.017	0.103-0.334	0.085-0.113
(around grt rim)	0.552-0.672	0.459-0.692	0.243-0.438	0.008-0.022	0.159-0.358	0.061-0.088
(matrix)	0.539-0.701	0.522-0.668	0.276-0.388	0.008-0.019	0.162-0.287	0.078-0.092
333-2-03						
(included in grt)	0.649-0.704	0.420-0.661	0.451-0.576	0.017-0.023	0.100-0.176	0.044-0.063
(around grt rim)	0.573-0.668	0.407-0.536	0.340-0.458	0.005-0.016	0.133-0.287	0.043-0.052
(matrix)	0.538-0.628	0.479-0.620	0.281-0.482	0.006-0.013	0.085-0.267	0.041-0.076
10-A1-76						
(included in grt)	0.520-0.614	0.574-0.678	0.256-0.337	0.001-0.017	0.100-0.304	0.010-0.068
(around grt rim)	0.553-0.614	0.490-0.591	0.253-0.399	0.002-0.014	0.089-0.216	0.024-0.066
(matrix)	0.504-0.594	0.547-0.676	0.209-0.342	0.005-0.016	0.014-0.241	0.062-0.068

White Gneisses

2163d2-11	**X(Mg)***	**Ti**	**Al^{vi}**	**Ba**	**F**	**Cl**
(included in grt)	0.587-0.699	0.330-0.559	0.224-0.329	0.001-0.012	0.014-0.135	0.022-0.071
(matrix)	0.652-0.720	0.395-0.559	0.207-0.419	0.002-0.014	0.028-0.168	0.053-0.106

X(Mg)* = [Mg/(Mg+Fe)]

Table 6.4: Compositional ranges and averages of spinel in terms of Spl, X(Hc), Gah and X(Mag).

Spinel Compositional Ranges

Sample	**Spl**	**X(Hc)***	**Gah**	**X(Mag)***
354-2-04 (sml grt)	0.139-0.146	0.634-0.654	0.129-0.146	0.010-0.016
354-2-04 (lrg grt)	0.131-0.137	0.554-0.573	0.254-0.271	0.004-0.007
10-A1-76 (sml grt)	0.163-0.183	0.610-0.645	0.099-0.104	0.004-0.017
10-A1-76 (lrg grt)	0.175-0.186	0.620-0.633	0.079-0.085	0.017-0.024

Average Spinel Composition

Sample	**Spl**	**X(Hc)***	**Gah**	**X(Mag)***
354-2-04 (sml grt)	0.143	0.644	0.137	0.014
354-2-04 (lrg grt)	0.134	0.563	0.259	0.005
10-A1-76 (sml grt)	0.173	0.630	0.101	0.011
10-A1-76 (lrg grt)	0.180	0.626	0.081	0.020

X(Hc)* = [Fe^{2+} - (Fe^{3+}/2)]
X(Mag)* = (Fe^{3+}/2)

Table 6.5: Compositional ranges and averages of K-feldspar in terms of Or, Ab, An, Ba, and Sr.

K-feldspar

Aluminous gneisses	**Or**	**Or *(Average)***	**Ab**	**Ab *(Average)***	**An**	**An *(Average)***	**Ba**	**Sr**
354-2-04 (rim grt)	0.890-0.899	0.892	0.095-0.121	0.111	0.001-0.002	0.001	0.004-0.009	0.003-0.005
354-2-04 (matrix)	0.768-0.910	0.868	0.093-0.242	0.136	0.001-0.005	0.003	0.003-0.007	0.003-0.006
331E2-11 (rim grt)	0.784-0.890	0.851	0.098-0.213	0.141	0.002-0.006	0.003	0.005-0.011	0.004-0.007
331E2-11 (matrix)	0.804-0.912	0.870	0.079-0.202	0.127	0.001-0.004	0.002	0.005-0.011	0.004-0.007
333-03 (rim grt)	0.843-0.920	0.867	0.084-0.148	0.130	0.003-0.005	0.004	0.004-0.017	0.004-0.007
333-03 (matrix)	0.803-0.917	0.823	0.075-0.138	0.106	0.003-0.015	0.006	0.007-0.013	0.005-0.007
333-2-03 (rim grt)	0.831-0.931	0.882	0.073-0.134	0.103	0.001-0.006	0.003	0.004-0.009	0.004-0.007
333-2-03 (matrix)	0.838-0.931	0.891	0.059-0.161	0.099	0.001-0.010	0.003	0.007-0.012	0.004-0.007
10-A1-76 (rim grt)	0.857-0.908	0.883	0.086-0.134	0.109	0.002-0.004	0.004	0.005-0.009	0.003-0.005
10-A1-76 (matrix)	0.763-0.921	0.861	0.084-0.190	0.137	0.002-0.007	0.004	0.004-0.010	0.004-0.006
White gneisses	**Or**	**Or *(Average)***	**Ab**	**Ab *(Average)***	**An**	**An *(Average)***	**Ba**	**Sr**
355a-11 (rim grt)	0.804-0.825	0.808	0.113-0.171	0.160	0.004-0.005	0.004	0.004-0.006	0.004-0.005
355a-11 (matrix)	0.814-0.858	0.843	0.131-0.141	0.137	0.003	0.003	0.003-0.005	0.004
206a-04 (rim grt)	0.825-0.877	0.854	0.119-0.182	0.145	0.003-0.007	0.005	0.008-0.011	0.003-0.005
206a-04 (matrix)	0.936	0.936	0.050	0.050	0.004	0.004	0.010	0.005
2163d2-11 (rim grt)	0.915-0.926	0.921	0.087-0.089	0.088	0.002-0.004	0.003	0.001-0.006	0.003-0.006
2163d2-11 (matrix)	0.845-0.920	0.873	0.080-0.182	0.135	0.004-0.011	0.007	0.004-0.008	0.004-0.005
Garnetites	**Or**	**Or *(Average)***	**Ab**	**Ab *(Average)***	**An**	**An *(Average)***	**Ba**	**Sr**
355-2a-04 (rim grt)	0.847-0.922	0.890	0.011-0.196	0.115	0.001-0.005	0.003	0.002-0.008	0.004-0.007
355-2a-04 (matrix)	0.835-0.920	0.883	0.062-0.176	0.122	0.001-0.004	0.002	0.003-0.014	0.007-0.014
355c2-11 (rim grt)	0.797-0.889	0.849	0.114-0.206	0.152	0.003-0.004	0.003	0.007-0.011	0.004-0.008
355c2-11 (matrix)	0.823-0.889	0.846	0.117-0.182	0.155	0.002-0.006	0.003	0.005-0.010	0.004-0.008

Table 6.6: Compositional ranges, averages and zoning trends of plagioclase in terms of Or, Ab, An, Ba, and Sr.

Plagioclase

Aluminous gneisses	**Ab**	**Ab *(Average)***	**Ab Trends**	**An**	**An *(Average)***	**An Trends**	**Or**	**Or *(Average)***	**Or Trends**	**Ba**	**Sr**
354-2-04 (rim grt)	0.715-0.860	0.794	↓ towards Al-nodule	0.130-0.259	0.185	↑ towards Al-nodule	0.010-0.016	0.012	slight ↑ towards Al-nodule	0.000-0.001	0.003-0.005
354-2-04 (matrix)	0.809-0.871	0.842	↑ in Na	0.113-0.155	0.134	↓ in Ca	0.006-0.010	0.008	↓ in K	0.000-0.002	0.003-0.004
331E2-11 (rim grt)	0.798-0.828	0.811	↓ towards Al-nodules	0.177-0.200	0.184	↑ towards Al-nodules	0.008-0.013	0.011	↓ towards Al-nodules	0.000-0.002	0.004-0.006
331E2-11 (matrix)	0.789-0.903	0.832	↓ away from bt zones	0.084-0.206	0.172	↑ away from bt zones	0.006-0.014	0.010	↑ away from bt zones	0.000-0.0001	0.003-0.006
333-2-03 (rim grt)	0.847-0.872	0.862	↓ towards garnet	0.128-0.136	0.132	↑ towards garnet	0.010-0.019	0.013	↓ towards garnet	0.000-0.002	0.004-0.006
333-2-03 (matrix)	0.806-0.868	0.853	homo Na	0.127-0.139	0.133	↓ away from bt zones	0.009-0.015	0.012	↓ away from bt zones	0.000-0.002	0.004-0.005
333-03 (rim grt)	0.780-0.784	0.782	↓ towards garnet	0.182-0.198	0.184	↑ towards garnet	0.014-0.017	0.016	↑ towards garnet	0.000-0.001	0.003-0.005
333-03 (matrix)	0.775-0.803	0.788	↓ in Na	0.180-0.198	0.188	homo Ca	0.007-0.022	0.018	↑ in K	0.000-0.002	0.003-0.005
10-A1-76 (rim grt)	0.733-0.759	0.750	↓ towards Al-nodules	0.228-0.269	0.242	↑ towards Al-nodules	0.010-0.016	0.013	↓ towards Al-nodules	0.000-0.001	0.003-0.005
10-A1-76 (matrix)	0.746-0.767	0.759	↓ in center of grains	0.227-0.246	0.232	↑ in center of grains	0.010-0.017	0.013	↑ in center of grains	0.000-0.001	0.003-0.005
White gneisses	**Ab**	**Ab *(Average)***	**Ab Trends**	**An**	**An *(Average)***	**An Trends**	**Or**	**Or *(Average)***	**Or Trends**	**Ba**	**Sr**
355A-11 (rim grt)	0.718-0.757	0.737	↑ away from garnet	0.230-0.242	0.236	↓ away from garnet	0.011-0.013	0.012	↑ away from garnet	0.001	0.003-0.005
355a-11(matrix)	0.782-0.788	0.785	↑ in Na	0.232-0.240	0.236	homo Ca	0.008-0.009	0.009	↓ in K	0.000	0.004-0.005
206a-04 (rim grt)	0.675-0.698	0.683	↑ away from garnet	0.299-0.327	0.316	↓ away from garnet	0.010-0.012	0.011	↑ away from garnet	0.000-0.001	0.003-0.005
206a-04 (matrix)	0.690	0.690	↓ in Na	0.310	0.310	↑ in Ca	0.009	0.009	↓ in K	0.001	0.003
2163d2-11 (rim grt)	0.735-0.741	0.738	↑ away from garnet	0.258-0.260	0.259	↓ away from garnet	0.009-0.014	0.011	↑ away from garnet	0.000-0.001	0.003-0.005
2163d2-11 (matrix)	0.720-0.772	0.748	↓ in Na	0.218-0.268	0.290	similar with variation	0.011-0.017	0.014	↑ in K	0.000-0.007	0.002-0.005
Garnetites	**Ab**	**Ab *(Average)***	**Ab Trends**	**An**	**An *(Average)***	**An Trends**	**Or**	**Or *(Average)***	**Or Trends**	**Ba**	**Sr**
355c2-11 (rim grt)	0.689-0.750	0.709	↓ in center of layer	0.251-0.316	0.296	↑ in center of layer	0.008-0.011	0.009	↑ in center of layer	0.000-0.001	0.004-0.006
355c2-11 (matrix)	0.687-0.742	0.703	↓ in center of grains	0.262-0.309	0.298	↑ in center of grains	0.007-0.013	0.009	slight ↑ in center of grains	0.000-0.002	0.004-0.005
355cx-11 (rim grt)	0.687-0.729	0.712	↓ in center of layer	0.284-0.302	0.293	↑ in center of layer	0.017-0.027	0.021	↑ in center of layer	0.000-0.002	0.003-0.005

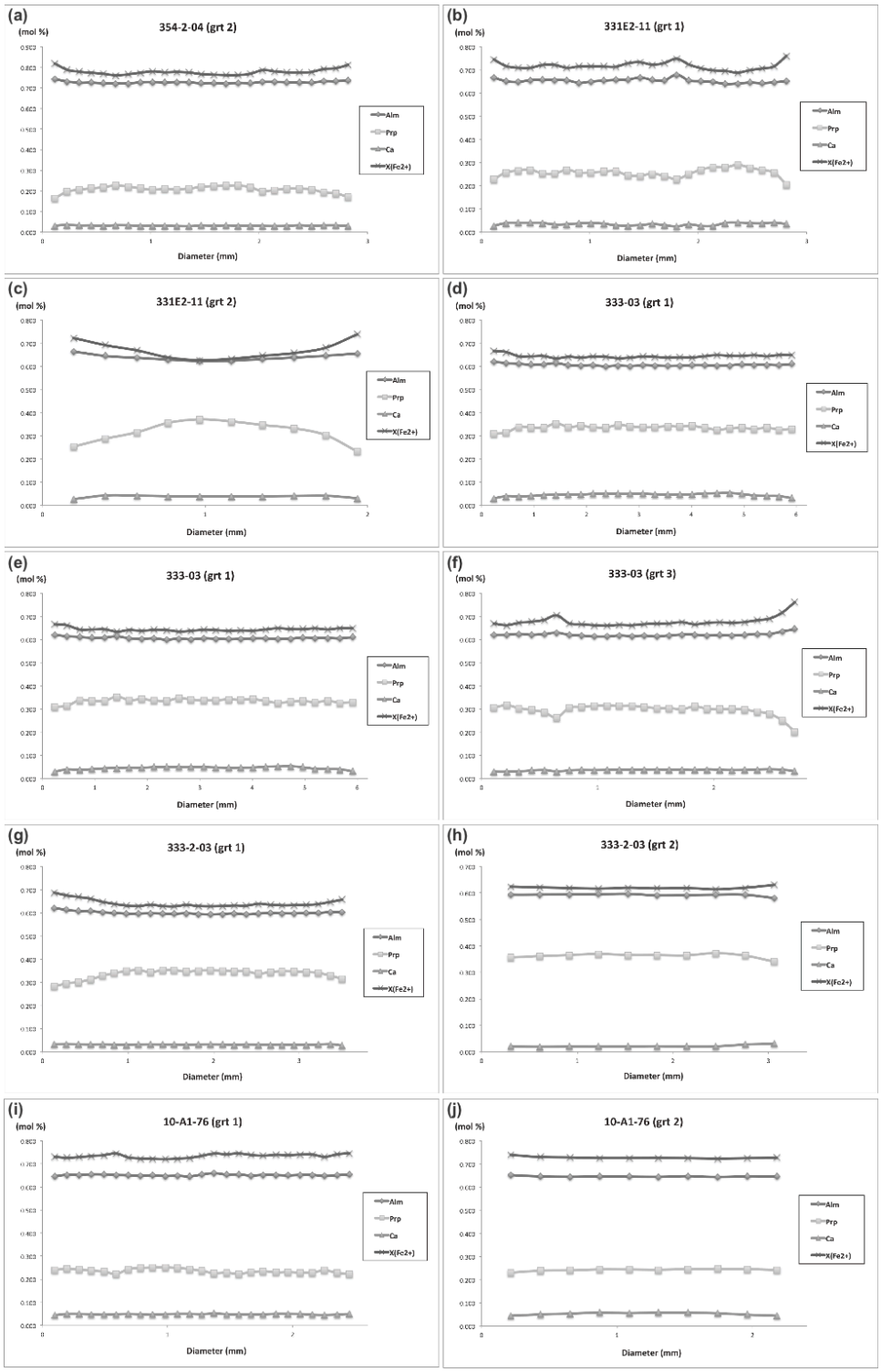

Figure 6.1: Zoning profiles of garnets from aluminous gneisses in terms of Alm, Prp, Ca (Grs+And), and X(Fe^{2+}). **(a)** 354-2-04; **(b)** 331E2-11 grt 1; **(c)** 331E2-11 grt 2; **(d)** 333-03 grt 1; **(e)** 333-03 grt 2; **(f)** 333-03 grt 3; **(g)** 333-2-03 grt 1; **(h)** 333-2-03 grt 2; **(i)** 10-A1-76 grt 1; and **(j)** 10-A1-76 grt 2.

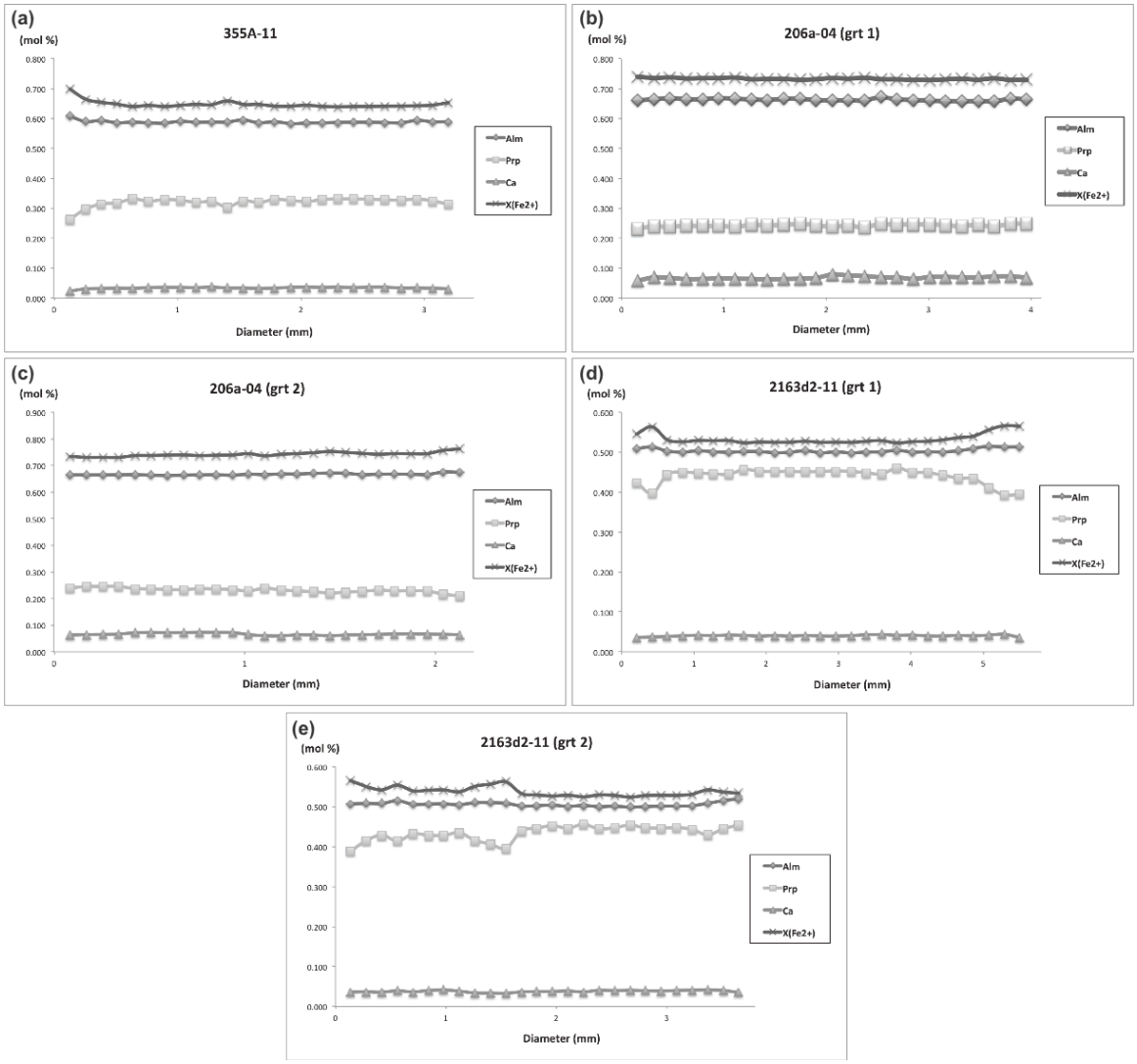

Figure 6.2: Zoning profiles of garnets from white gneisses in terms of Alm, Prp, Ca (Grs+And), and X(Fe^{2+}). **(a)** 355a-11; **(b)** 206a-04 grt 1; **(c)** 206a-04 grt 2; **(d)** 2163d2-11 grt 1; and **(e)** 2163d2-11 grt 2.

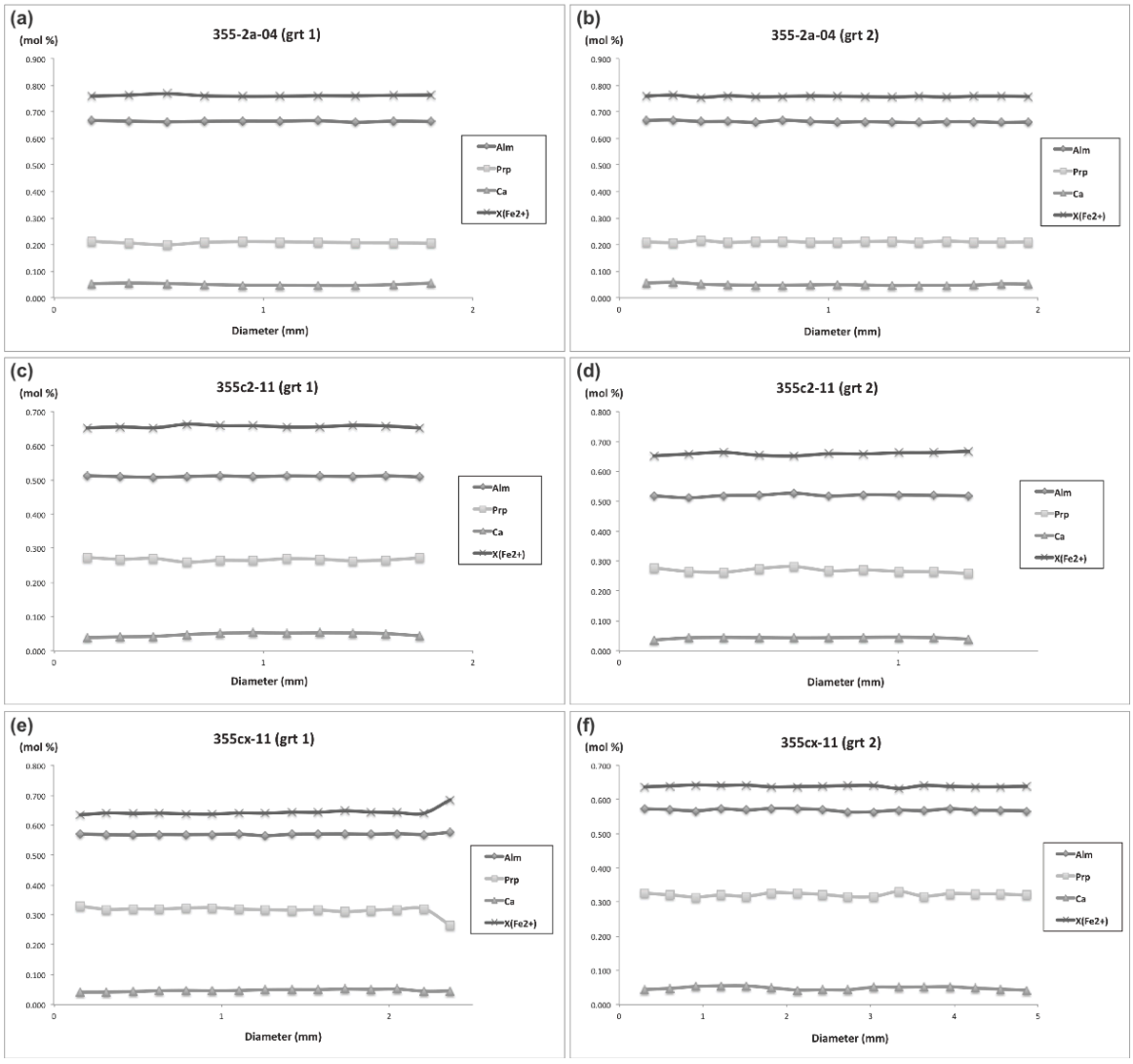

Figure 6.3: Zoning profiles of garnets from garnetites in terms of Alm, Prp, Ca (Grs+And), and X(Fe^{2+}). **(a)** 355-2a-04 grt 1; **(b)** 355-2a-04 grt 2; **(c)** 355c2-11 grt 1; **(d)** 355c2-11 grt 2; **(e)** 355cx-11 grt 1; and **(f)** 355c2-11 grt 2.

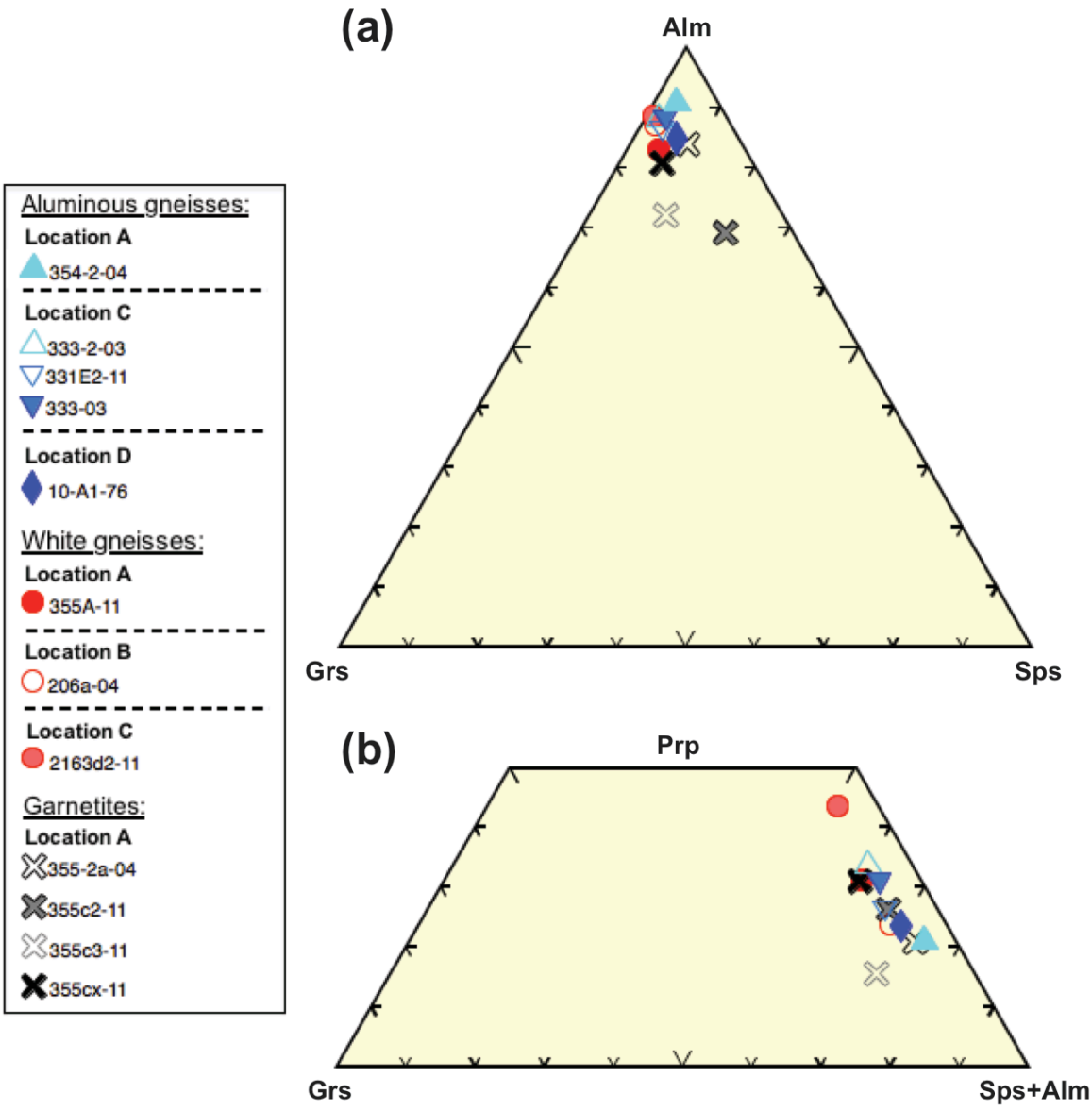

Figure 6.4: Ternary composition plots of garnet: **(a)** Alm-Grs-Sps; and **(b)** Prp-Grs-Sps+Alm.

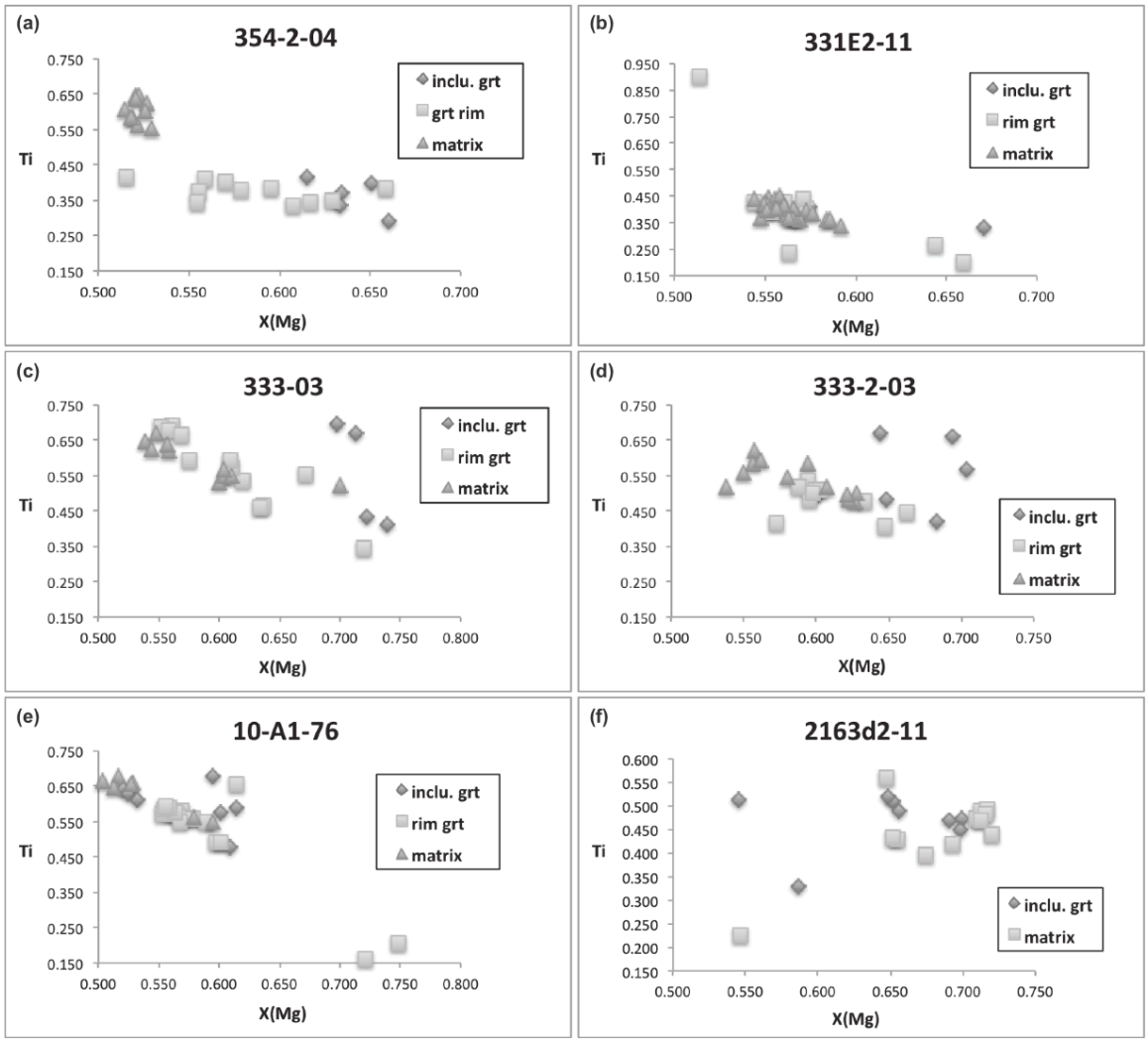

Figure 6.5: Ti vs. X(Mg) composition plots of biotite from: **(a)** 354-2-04; **(b)** 10-A1-76; **(c)** 333-2-03; **(d)** 331E2-11; **(e)** 333-03; and **(f)** 2163d2-11.

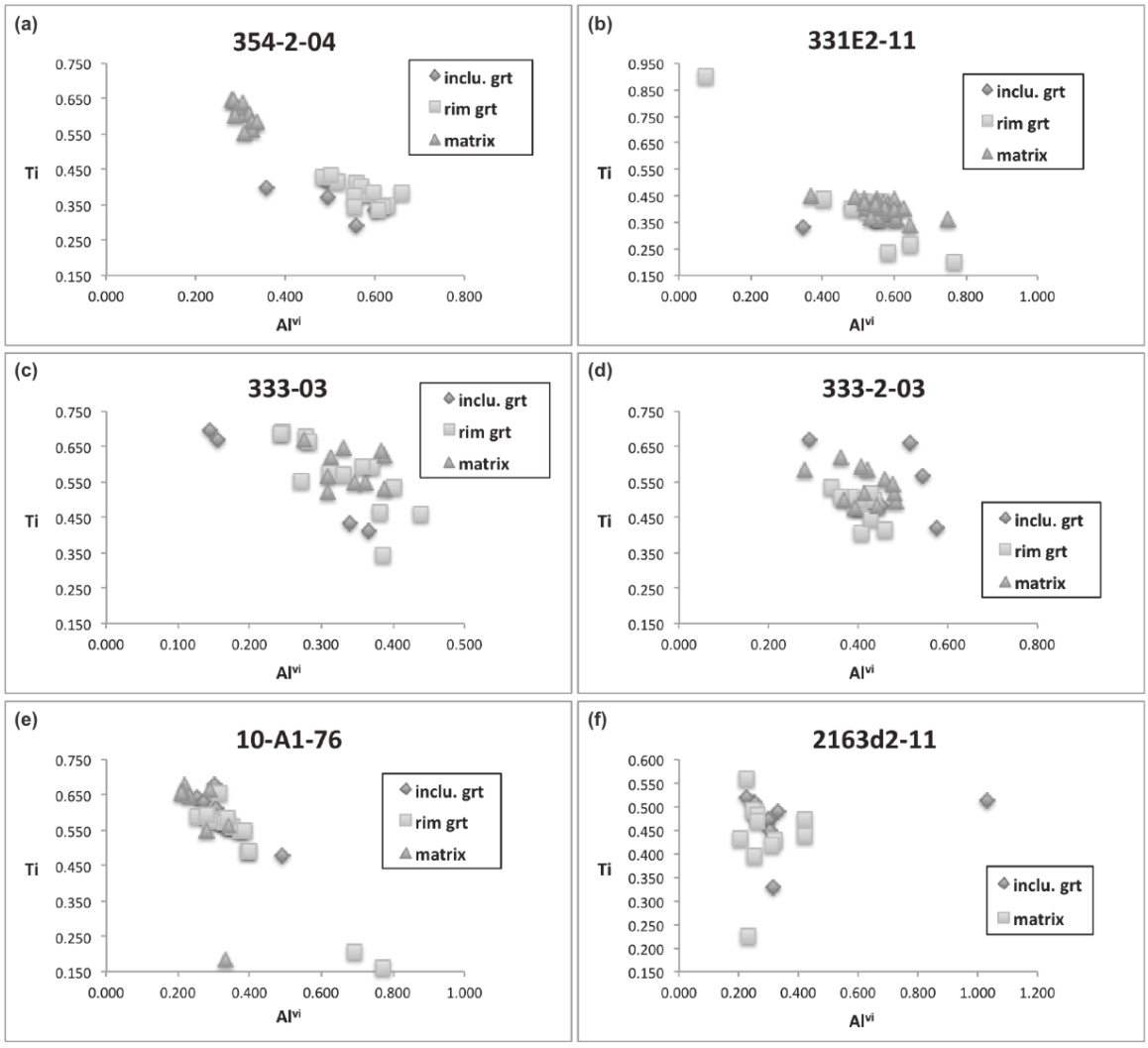

Figure 6.6: Ti vs. Al^{VI} composition plots of biotite from: **(a)** 354-2-04; **(b)** 10-A1-76; **(c)** 333-2-03; **(d)** 331E2-11; **(e)** 333-03; and **(f)** 2163d2-11.

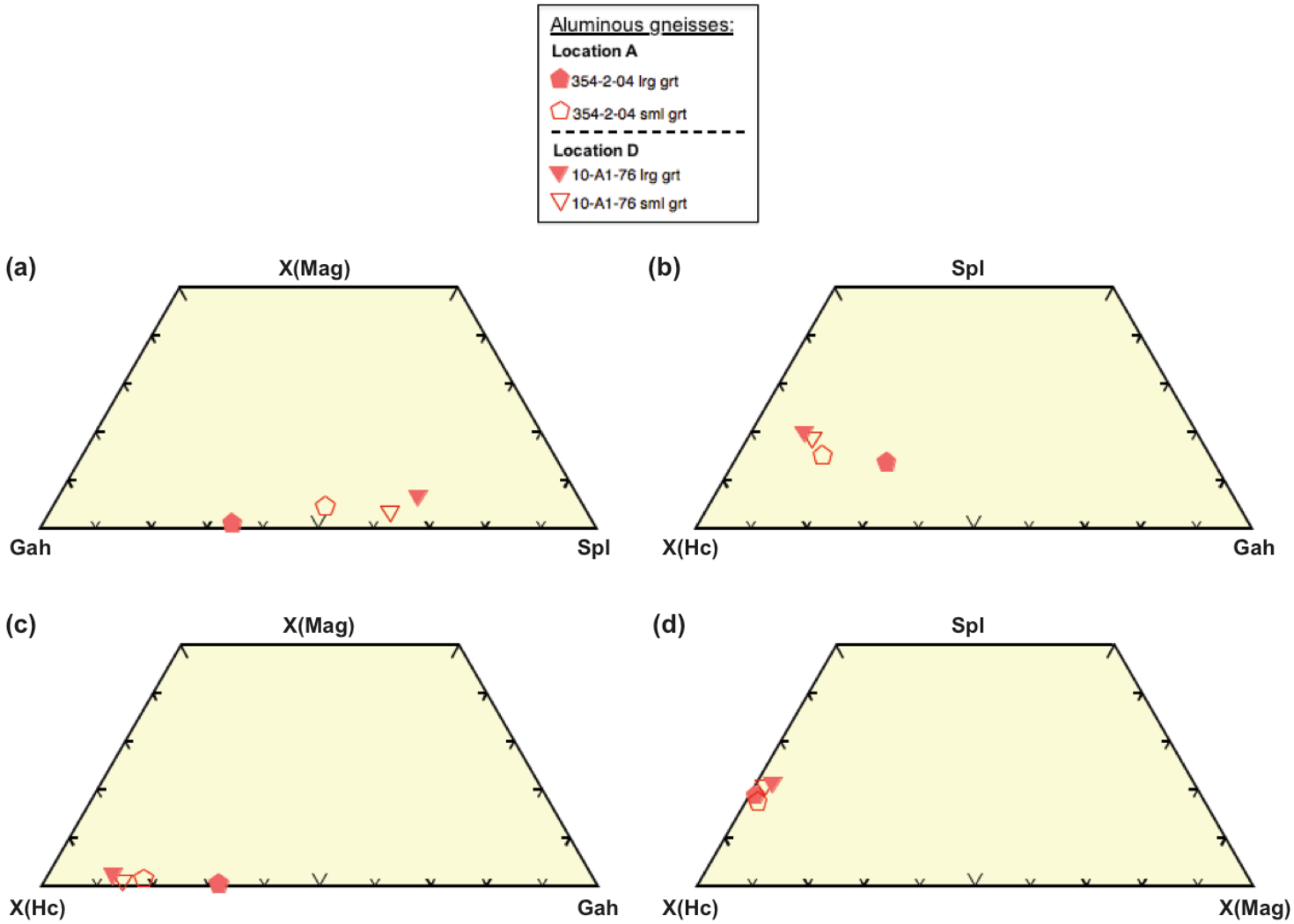

Figure 6.7: Ternary composition plots of spinel: **(a)** Gah-X(Mag)-Spl; **(b)** X(Hc)-Gah-Spl; **(c)** X(Hc)-Gah-X(Mag); and **(d)** X(Hc)-Spl-X(Mag).

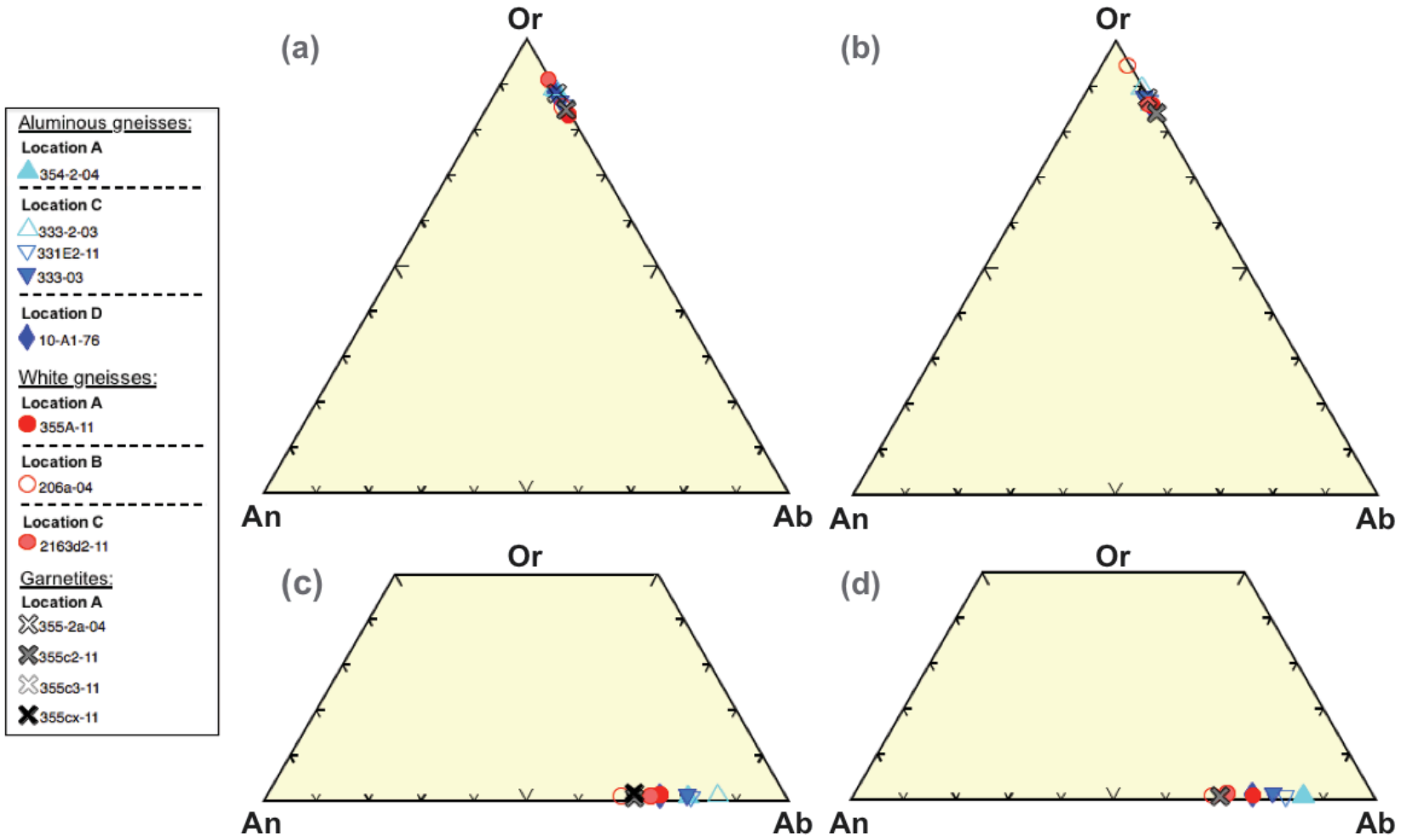

Figure 6.8: Ternary Or-An-Ab composition plots of K-feldspar and plagioclase from: **(a)** K-feldspar grains adjacent to garnet; **(b)** interstitial K-feldspar grains in the matrix; **(c)** plagioclase grains adjacent to garnet; and **(d)** interstitial plagioclase grains in the matrix.

Chapter 7: GEOCHEMISTRY

7.1 INTRODUCTION

Whole-rock major and minor/trace element contents were obtained from a selection of three aluminous gneisses, nine white gneisses, seven pink gneisses, and four garnetites to:

(i) characterize the bulk compositions of the main rock types;

(ii) infer (if possible) their protoliths and tectonic setting; and

(iii) determine the degree and type of alteration(s).

7.2 MAJOR AND MINOR/TRACE ELEMENT COMPOSITION

Major oxide data normalized to 100% using total Fe as FeO* (calculated in IgPet software) are listed in Table 7.1 (in oxide wt% including X(Mg)) and Table 7.2 (in mol %). The chemical variations among the samples are plotted in Harker diagrams as major oxides against SiO_2 and X(Mg), and shown in Figures. 7.1-7.2.

Major oxides when plotted against SiO_2 show a negative correlation with: (a) Al_2O_3 for all lithologies (Figs. 7.1a, 7.2b); (b) MgO (Fig. 7.1b), K_2O (Figs. 7.1f, 7.2e) and TiO_2 (Figs. 7.1g, 7.2f) for aluminous gneisses; (c) FeO* for aluminous gneisses and garnetites (Fig. 7.1c); and (d) TiO_2 for white and pink gneisses (Fig. 7.1g). In contrast, SiO_2 shows a positive correlation with Na_2O for the garnetites (Fig. 7.1e). X(Mg) for the white and pink gneisses show a negative correlation with K_2O (Fig. 7.2e), and a positive correlation with Al_2O_3 (Fig. 7.2b). In addition, values of FeO*, MgO, and CaO are highest, and Na_2O and K_2O lowest in the garnetite *355c3-11*. White and pink gneisses with highest values of CaO and Na_2O are the lowest in K_2O (*309-2-04*).

The chemical variation in molecular proportions (Table 7.2) for CaO-FeO*-MnO and CaO-FeO*-MgO are shown in ternary plots (Fig. 7.3), which illustrate: (a) that all samples have very low MnO (relative to FeO* and CaO), with the exception of the garnetites, which contain up to 0.3% MnO (*355c2-11*; Fig. 7.3a); (b) aluminous gneisses and garnetites have low CaO, with the exception of the homogeneous aluminous gneiss *333-03* (Fig. 7.3a); and (c) all rock types, (and more particularly the aluminous gneisses and garnetites) contain higher proportions of FeO* than MgO, except for the white gneiss *10-A1-RHY* with the highest CaO proportions (Fig. 7.3a).

The contents of trace elements Ba, Sr, and W are >1000 ppm for most of the samples from all lithologies, and highest in the white and pink gneisses (Table 7.3). In addition, traces of Zn are the highest in the garnetites and homogeneous aluminous gneiss *331E2-11*.

7.3 PROTOLITHS

The chemical protoliths of the aluminous, white, and pink gneisses are inferred from Figure. 7.4, and using so-called immobile trace element ratios Nb/Y and Zr/TiO_2. Assuming these elements were indeed immobile, all of the samples have a subalkalic Nb/Y ratio (i.e., <0.7), and moderate to high Zr/TiO_2 ratio, which is consistent with protoliths ranging from rhyolite/dacite to andesite/basalt. Most of the samples have Nb-Zr ratios >200 (Fig. 7.5), and are of a non-peralkaline affinity. These rocks show I-type to A-type affinities in terms of Yb-Ta and Nb-Y (Fig. 7.6), consistent with formation in arc to rifted arc setting. In addition, these ratios also show some samples have S-type affinities, which is consistent with formation in a syncollisional setting and attest to evidence of contamination during rifting.

Extended primitive mantle- (PM) and chondrite-normalized plots shown in Figures. 7.7-7.8 for all rock types illustrate: (a) an enrichment in light rare-earth elements (LREE); (b) a flat to slightly enriched signature for heavy rare-earth elements (HREE); (c) depletion in Nb relative to Th and La; (d) negative Eu, Ti, V, and Cr for rock/PM; and (e) both positive and negative Eu for rock/chondrite. The patterns in REE profiles for all lithologies are most consistent with a tholeiitic to calc-alkalic affinity.

7.4 ALTERATION

Ternary AFM and A'FK plots modeling the degree and type of alteration are shown in Figure. 7.9 (after Bonnet and Corriveau 2007). The AFM plot illustrates that most of the white, pink, and homogeneous aluminous gneisses (*333-03*) exhibit enrichment in Al (i.e. vector towards the A apex). Samples most enriched in Al (*448-11, 339b1-11*) also show enrichment in K (i.e. vector towards the K apex). Therefore, the high amounts of Al-silicate and K-feldspar for most of these rock types (with the exception of the garnetites), is indicative most likely the result of sericitic and argillic alteration prior to metamorphism.

7.4.1 Feldspar Alteration

The alteration of feldspars mostly occurs by weathering of the upper continental crust, and also by post-deposition processes such a K-metasomatism, and can be evaluated by the chemical index of alteration (CIA) and plagioclase index of alteration (PIA; Nesbitt and Young 1984; Taylor and McLennan 1985; McLennan *et al.* 2003). Ternary plots of CIA and PIA for feldspars are shown in Figure. 7.10. The CIA for feldspars illustrates: (a) proportions of K_2O are greatest in the white gneisses (*448-11*; Fig. 7.10a); (b) $CaO+Na_2O$ proportions are the greatest in the pink gneisses (*309-2-04*;

Fig. 7.10a); and (c) proportions of Al_2O_3 are the highest in the garnetites, which also have the greatest proportions of FeO*+MgO (Fig. 7.10b). In general, CIA values typically range 50% or less for most unaltered metamorphic rocks, 75% or greater for secondary clay minerals, and close to 100% for pure Al-silicate residues (MacLennan *et al.* 2003). Proposed by Fedo *et al.* (1995), the PIA is use to monitor the weathering of plagioclase, which is abundant in silicate rocks and tends to dissolve rapidly (Price and Velbel 2003). The PIA for feldspars (Fig. 7.10c) highlights that these rock types are mostly albitized (Ab) with higher proportions of Na_2O, except for the garnetites with highest proportions of Al_2O_3-K_2O and exhibit an anorthitic (An) composition of highest proportions in CaO (*355c3-11*).

7.4.2 Hydrothermal Alteration

Alkali mobility in all lithologies is further illustrated in Figure. 7.11. Most samples exhibit K-metasomatism in a Hughes (1973) plot (Fig. 7.11a); however, most gneisses have relatively moderate ratios of Al_2O_3/Na_2O suggesting that they are weakly altered, whereas the garnetites (*355cxA-11, 355c2-11*) show significant Na-depletion (Fig. 7.11b). Alteration indices such as Ishikawa *et al.* (1976) alteration index (AI = [(100*(K_2O+MgO))/(K_2O+MgO+Na_2O+CaO)]), used to quantify the intensity of sericite and argillic alteration of volcanic rocks from VMS environments, show most of the samples have AI values between 50 and 100 (Table 7.4), suggesting alteration by hydrothermal means (Large *et al.* 1992, 2001). Similarly, samples most enriched in Al and K have the largest AI values and are inferred the most altered. In addition, these samples also have high ratios of K/Na and Ba/Sr, which also suggest alkali mobility, most likely resulting from the influence of hydrothermal fluids (Fig. 7.11c).

7.5 SUMMARY

Whole-rock lithogeochemical data of aluminous, white, and pink gneisses, as well as garnetites of the LBS are consistent with rhyolite/dacite to andesite/basalt protoliths, and with likely tholeiitic to calc-alkaline trends that may have formed in an arc to rifted arc setting. This is consistent with the inferred emplacement of LBS in a Geon 12 intra-continental rift setting (Indares and Moukhsil 2013; Valverde *et al.* 2012). Preservation of these trends in rocks that have experienced subsequent granulite facies metamorphism and anatexis (see chapter 5) suggests that the degree of partial melting was low and that no significant amounts of melt had escaped from the source rocks.

The data also shows that aluminous, white, and pink gneisses are enriched in Al and K, and most comparable to sericitic and argillic alteration types. This is consistent with relatively high amounts of K-feldspar and/ or Al-silicates in several of these rocks. REE patterns show a range of Eu anomalies, from positive to negative that may represent different degrees of dissolution of plagioclase during alteration (e.g. Bonnet *et al.* 2005)

Alteration indices (AI) for most of these samples have values >50, and are consistent with alteration by hydrothermal fluids (Large *et al.* 1992, 2001). In general, these rocks show geochemical evidence of K-metasomatism and Na-depletion, most likely by the sericitization of K-feldspar and dissolution of plagioclase (i.e. Na-depletion) during fluid circulation (Galley 1993, 1995; Sillitoe *et al.* 1996; Gifkins *et al.* 2005). However, the Mn-rich garnetites, are the most Fe+Mg bearing and Na+Ca depleted, and show the lowest amounts of K. In addition, gneisses containing high amounts of K-feldspar and/ or Al-silicates, and low K garnetites show the highest ratios of K/Na-Ba/Sr, which is most likely correlative with being closer to the central alteration zones of the hydrothermal system (Large *et al.* 1992).

The high AI values, major element enrichments and depletions, and ratios of minor/ trace elements for most of these samples, suggests that these rocks most likely experience seafloor alteration prior to metamorphism, a setting commonly found in VMS environments (Franklin *et al.* 1981; Lydon 1988; Spry and Wonder 1989; Large *et al.* 1992; Hannington *et al*. 2005).

Table 7.1: Normalized major oxides (in terms of oxide wt%) using Fe as FeO* and including ratios of X(Mg) for all the examined lithologies of the LBS.

	Aluminous Gneisses			White Gneisses											
Sample:	331e2-11	333-03	216z-04	361A-11	355A-11	355b1-11	355cxB-11	2163d2-11	448-11	334a-04	10-AI-87B	10-AI-RHY	339b1-11	216e-11	2161b-11
SiO2	60.483	79.883	71.108	72.753	74.222	73.383	67.114	70.082	73.047	75.750	77.124	75.183	78.977	75.738	82.100
Al2O3	18.814	11.022	14.258	15.118	15.024	14.248	18.253	14.774	13.272	13.779	12.292	14.689	11.557	12.344	9.741
FeO*	5.524	1.032	4.005	1.214	0.380	2.590	2.441	4.102	3.625	0.878	1.030	0.180	0.849	2.564	0.934
MnO	0.074	0.044	0.054	0.022	0.020	0.080	0.209	0.059	0.051	0.009	0.034	0.056	0.023	0.053	0.014
MgO	3.436	0.521	2.267	0.638	0.112	0.691	0.869	2.372	0.259	0.060	0.123	0.407	0.132	0.207	0.090
CaO	0.827	1.532	1.021	1.903	1.284	1.290	1.667	1.088	1.134	1.910	0.675	1.689	0.549	1.106	0.452
Na2O	3.023	2.258	2.104	3.178	3.068	2.529	3.243	2.053	3.164	2.835	1.922	3.754	3.215	2.585	1.789
K2O	6.787	3.514	4.341	4.803	5.800	4.407	5.687	4.548	5.184	4.696	6.585	3.804	4.537	4.952	4.765
TiO2	1.011	0.189	0.738	0.331	0.030	0.640	0.457	0.818	0.205	0.014	0.103	0.187	0.149	0.400	0.104
P2O5	0.021	0.005	0.102	0.041	0.061	0.142	0.061	0.103	0.060	0.070	0.112	0.051	0.010	0.052	0.010
Total	*100.000*	*100.000*	*100.000*	*100.000*	*100.000*	*100.000*	*100.000*	*100.000*	*100.000*	*100.000*	*100.000*	*100.000*	*100.000*	*100.000*	*100.000*
X(Mg)	0.384	0.335	0.361	0.344	0.228	0.211	0.263	0.366	0.067	0.064	0.106	0.693	0.135	0.075	0.088

	Pink Gneisses							Garnetites			
Sample:	339b1-11	216e-11	2161b-11	319-1-11	305b-04	306-1-04	309-2-04	355cxA-11	355cxC-11	355c2-11	355c3-11
SiO2	78.977	75.738	82.100	72.547	71.080	66.037	61.751	67.882	78.796	64.214	51.005
Al2O3	11.557	12.344	9.741	13.976	15.092	19.140	20.799	14.113	11.573	16.103	18.330
FeO*	0.849	2.564	0.934	2.326	1.273	3.208	2.242	10.291	3.660	7.442	20.014
MnO	0.023	0.053	0.014	0.090	0.140	0.089	0.059	0.839	0.298	2.561	3.359
MgO	0.132	0.207	0.090	0.771	0.274	1.742	1.491	3.418	1.247	2.509	3.155
CaO	0.549	1.106	0.452	1.673	2.263	1.203	4.801	1.279	1.666	1.006	3.581
Na2O	3.215	2.585	1.789	3.144	3.494	3.142	6.385	1.101	2.055	1.265	0.021
K2O	4.537	4.952	4.765	4.767	5.651	4.531	1.995	0.661	0.378	4.179	0.064
TiO2	0.149	0.400	0.104	0.544	0.576	0.772	0.426	0.364	0.275	0.566	0.363
P2O5	0.010	0.052	0.010	0.162	0.158	0.135	0.051	0.052	0.051	0.156	0.107
Total	*100.000*	*100.000*	*100.000*	*100.000*	*100.000*	*100.000*	*100.000*	*100.000*	*100.000*	*100.000*	*100.000*
X(Mg)	0.135	0.075	0.088	0.249	0.177	0.352	0.399	0.249	0.254	0.252	0.136

X(Mg) = MgO/(MgO+FeO*)

Table 7.2: Calculated molecular proportions (%) of major oxides, and using Fe as FeO* for all the examined lithologies of the LBS.

	Aluminous Gneisses			White Gneisses								
Sample:	331e2-11	333-03	216z-04	361A-11	355A-11	355b1-11	355cxB-11	2163d2-11	448-11	334a-04	10-AI-87B	10-AI-RHY
SiO2	55.670	75.935	67.057	67.888	69.219	69.263	62.222	66.014	72.959	68.707	71.177	69.987
Al2O3	20.409	12.349	15.847	16.627	16.513	15.850	19.945	16.402	13.704	14.713	15.259	16.115
FeO*	4.252	0.821	3.159	0.947	0.296	2.044	1.892	3.232	0.815	2.851	0.690	0.140
MnO	0.058	0.035	0.043	0.017	0.016	0.064	0.164	0.047	0.027	0.040	0.007	0.044
MgO	4.715	0.738	3.188	0.887	0.156	0.972	1.201	3.330	0.173	0.363	0.084	0.565
CaO	0.816	1.561	1.032	1.902	1.283	1.304	1.656	1.098	0.684	1.143	1.923	1.684
Na2O	5.394	4.161	3.847	5.750	5.547	4.628	5.829	3.750	3.526	5.770	5.166	6.775
K2O	7.970	4.261	5.222	5.718	6.900	5.307	6.726	5.466	7.948	6.220	5.629	4.518
TiO2	0.700	0.135	0.524	0.232	0.021	0.454	0.318	0.580	0.073	0.145	0.010	0.131
P2O5	0.017	0.004	0.082	0.032	0.048	0.114	0.048	0.082	0.090	0.048	0.055	0.040
Total	*100.00*	*100.00*	*100.00*	*100.00*	*100.00*	*100.00*	*100.00*	*100.00*	*100.00*	*100.00*	*100.00*	*100.00*

	Pink Gneisses							Garnetites			
Sample:	339b1-11	216e-11	2161b-11	319-1-11	305b-04	306-1-04	309-2-04	355cxA-11	355cxC-11	355c2-11	355c3-11
SiO2	74.327	67.988	78.469	71.693	66.162	61.255	55.710	65.527	75.684	61.305	50.392
Al2O3	12.819	15.437	10.973	13.771	16.556	20.925	22.116	16.056	13.102	18.119	21.344
FeO*	0.668	1.823	0.746	2.030	0.991	2.489	1.692	8.308	2.940	5.942	16.536
MnO	0.019	0.072	0.011	0.042	0.110	0.070	0.045	0.686	0.242	2.071	2.811
MgO	0.186	1.077	0.129	0.292	0.380	2.409	2.005	4.919	1.786	3.571	4.646
CaO	0.554	1.680	0.463	1.122	2.257	1.195	4.641	1.323	1.715	1.029	3.790
Na2O	5.866	5.713	3.316	4.744	6.306	5.650	11.168	2.061	3.827	2.342	0.041
K2O	5.448	5.699	5.810	5.980	6.711	5.362	2.296	0.813	0.464	5.089	0.081
TiO2	0.105	0.383	0.074	0.285	0.403	0.539	0.289	0.264	0.199	0.406	0.270
P2O5	0.008	0.129	0.008	0.041	0.124	0.106	0.039	0.043	0.042	0.126	0.089
Total	*100.00*	*100.00*	*100.00*	*100.00*	*100.00*	*100.00*	*100.00*	*100.00*	*100.00*	*100.00*	*100.00*

Table 7.3: Trace elements (in terms of ppm) for all the examined lithologies of the LBS.

	Aluminous Gneisses			White Gneisses								
Sample:	331E2-11	333-03	216z-04	361A-11	355A-11	355b1-11	355cxB-11	2163d2-11	448-11	334a-04	10-A1-87B	10-A1-RHY
Co (ppm)	99	119	256	105	97	87	85	110	141	543	285	108
Cr	150	10	90	10	10	10	10	80	10	10	10	10
Cu	60	5	30	10	5	5	5	20	5	5	5	5
Ni	70	10	70	10	10	10	10	50	10	10	10	10
Sc	21	6	15	6	2	9	10	15	3	5	2	5
Be	0.5	0.5	0.5	1	1	0.5	1	0.5	0.5	1	1	2
V	165	10	110	37	6	33	39	117	8	10	0.5	15
Zn	120	15	40	15	15	30	50	40	15	15	15	30
Ba	1117	1844	639	1288	693	803	1773	687	220	1360	2296	687
Ga	24	9	18	15	13	15	17	17	14	15	11	16
Ge	2	0.5	1	1	1	1	2	1	1	1	0.5	1
As	2.5	2.5	2.5	2.5	2.5	2.5	2.5	2.5	2.5	2.5	2.5	2.5
Ag	1.2	0.25	0.25	0.5	0.25	1.6	0.6	0.25	0.25	0.25	0.25	0.25
In	0.1	0.1	0.1	0.1	0.1	0.1	0.1	0.1	0.1	0.1	0.1	0.1
Sn	0.5	0.5	1	0.5	0.5	0.5	0.5	1	0.5	3	0.5	0.5
Sb	0.25	0.25	0.25	0.25	0.25	0.25	0.25	0.25	0.25	2.1	0.25	0.25
Cs	1.3	0.25	1	0.25	0.25	0.25	0.25	1	0.7	0.25	0.25	1.1
Rb	177	81	101	103	115	90	109	103	146	102	71	94
Sr	230	198	76	250	144	119	291	78	72	248	471	128
Th	10.1	1.1	12.6	17.4	0.05	33.7	4.9	11.2	1.6	34.5	0.4	14.8
U	1.3	0.3	2.9	1.6	0.2	1.4	0.8	2.8	0.3	2.2	0.3	2.4
Zr	290	160	259	192	27	478	220	238	75	170	52	128
Hf	7.8	3.9	6.4	5	0.9	11.6	6.2	6.2	2.3	5.4	1.3	3.4
Nb	14	3	11	10	0.5	18	22	11	2	7	2	9
Mo	1	1	1	1	1	1	1	1	1	1	1	1
Ta	1.8	2	2.5	2.8	1.9	2.2	2.7	2.3	2.4	0.6	7.5	3.3
W	213	566	961	472	415	395	371	445	603	1700	1160	451
Tl	0.8	0.4	0.6	0.7	0.7	0.6	0.7	0.6	0.9	0.5	0.5	0.5
Pb	52	14	10	26	36	26	35	8	24	61	38	33
Bi	0.2	0.2	0.2	0.2	0.2	0.2	0.2	0.2	0.2	0.2	0.2	0.2
Y	31	26	23	26	11	44	32	20	30	48	4	20
La	45.4	18.3	39.4	67	10	151	37	37.7	15.4	80.6	6.3	31.8
Ce	75.7	32.7	78	130	17.8	319	63.5	77	29.8	154	10	54.6
Pr	8	2.95	9.22	14.6	1.96	36.4	6.46	9.07	3.25	15.8	1.02	5.52
Nd	28.8	9.9	36	54.5	7.1	131	22.4	34.3	11.7	52.7	3.7	19.2
Sm	5	1.3	6.6	9.8	1.3	19.7	4.3	6.2	2.6	8.1	0.7	3.2
Eu	2.1	1.07	1.33	2.73	1.76	1.59	2.79	1.27	0.6	1.2	2.24	0.72
Gd	5.2	1.3	5.2	7.2	0.9	12.1	5	4.6	2.9	5.8	0.6	2.6
Tb	0.9	0.3	0.8	1	0.2	1.6	0.9	0.7	0.7	1	0.05	0.5
Dy	5.6	3.1	4.5	4.9	1.4	8.2	5.4	3.6	4.9	6.5	0.6	3
Ho	1.2	0.9	0.9	0.9	0.4	1.5	1.1	0.8	0.9	1.6	0.1	0.6
Er	3.6	3.3	2.5	2.4	1.2	4.4	3.2	2.4	2.3	6	0.5	2
Tm	0.58	0.58	0.38	0.31	0.21	0.65	0.51	0.37	0.3	1.15	0.09	0.33
Yb	3.9	4.3	2.5	1.9	1.4	4.1	3.4	2.7	1.7	8.1	0.7	2.3
Lu	0.65	0.74	0.4	0.31	0.22	0.64	0.57	0.43	0.24	1.24	0.1	0.37

Table 7.3: *(continued)*

	Pink Gneisses							Garnetites			
Sample:	339b1-11	319-1-11	2161b-11	216e-11	305b-04	306-1-04	309-2-04	355cxA-11	355cxC-11	355c2-11	355c3-11
Co (ppm)	122	79	128	91	552	548	139	191	142	164	199
Cr	10	10	10	10	10	90	10	10	10	20	10
Cu	5	5	5	5	10	5	5	10	5	5	5
Ni	10	10	10	10	10	10	10	10	10	10	10
Sc	2	10	0.5	7	11	17	23	33	8	16	84
Be	2	3	0.5	1	2	0.5	2	0.5	1	0.5	0.5
V	8	45	11	12	7	91	44	91	34	66	66
Zn	15	60	15	70	80	60	60	130	50	110	140
Ba	191	1195	1335	1477	1880	1400	959	183	71	1214	39
Ga	13	16	10	18	26	23	26	10	12	15	16
Ge	1	1	1	2	2	1	1	5	3	4	6
As	2.5	2.5	2.5	2.5	2.5	11	2.5	2.5	2.5	2.5	2.5
Ag	0.25	0.6	0.8	1.4	0.25	0.25	1.6	0.25	0.25	0.25	0.25
In	0.1	0.1	0.1	0.1	0.1	0.1	0.1	0.1	0.1	0.1	0.1
Sn	1	2	0.5	0.5	2	0.5	2	0.5	0.5	0.5	0.5
Sb	0.25	0.25	0.25	0.25	1.4	0.25	0.25	0.25	0.25	0.25	0.25
Cs	0.25	1.5	0.25	0.25	0.25	0.25	0.25	0.25	0.25	0.25	0.25
Rb	125	147	89	106	91	140	21	12	6	98	2
Sr	29	203	304	123	140	268	1263	62	107	201	1
Th	20.8	16.7	6.7	9.5	9	16.8	0.7	8.2	18.5	11.2	32.9
U	1.6	1.7	0.7	0.6	0.6	1.8	0.3	1.1	1.6	1.3	2.7
Zr	141	232	248	453	914	240	463	166	120	183	53
Hf	4.8	6	7.7	12	21.7	7.1	9.8	4.4	3.2	4.8	1.7
Nb	13	16	1	11	40	18	6	15	9	11	12
Mo	1	1	1	1	1	1	1	2	1	1	1
Ta	2.7	1.8	2.2	1.6	1.9	1.4	0.2	3	2.8	2.3	2.6
W	541	333	579	410	1560	1670	398	846	640	612	794
Tl	0.6	0.7	0.4	0.6	0.4	0.5	0.05	0.05	0.05	0.7	0.05
Pb	16	23	16	20	36	18	17	6	7	28	2.5
Bi	0.2	0.2	0.2	0.2	0.2	0.2	0.2	0.2	0.2	0.2	0.2
Y	27	44	8	45	120	44	24	108	34	39	414
La	44.7	58.8	30.1	89.3	106	61.9	27.4	37.8	74.7	52.4	94.5
Ce	93.8	122	64.4	187	221	126	57.4	77.5	159	114	188
Pr	10.4	13.6	7.16	21.6	26.3	14.4	8.21	9.09	18.7	12.7	21.7
Nd	37.2	49.3	26.8	83	103	53.3	36.1	35.9	71	49.1	82.2
Sm	6.8	8.9	5.6	14.9	20.4	9.3	7.9	10.1	12.5	9.5	19.3
Eu	0.31	1.39	0.68	2.73	4.37	1.92	2.32	0.81	1.06	1.68	0.92
Gd	5	6.8	4	10.9	20.3	8.2	6.2	15.5	8.6	7.6	27.3
Tb	0.8	1.1	0.5	1.5	3.8	1.3	0.9	2.8	1.2	1.2	6.5
Dy	4.4	6.6	2.1	8.5	22.1	7.5	5	18.2	5.9	6.7	54.6
Ho	0.9	1.5	0.3	1.8	4.5	1.5	0.9	3.6	1.1	1.4	13.8
Er	3.1	4.8	0.7	5.6	13.7	4.6	2.5	10.5	3	4.3	42
Tm	0.55	0.83	0.1	0.87	2.11	0.75	0.36	1.66	0.43	0.66	6.36
Yb	3.9	6.1	0.7	5.7	13.6	5	2.2	10.9	2.8	4.6	40.3
Lu	0.64	1.01	0.14	0.97	2.04	0.75	0.3	1.68	0.47	0.75	6.09

Table 7.4: Alteration Index (AI) for all the examined lithologies of the LBS.

Sample:	Alteration Index (AI)
331e2-11	72.645
333-03	51.567
216z-04	67.891
361A-11	51.711
355A-11	57.597
355b1-11	57.175
355cxB-11	57.181
2163d2-11	68.776
448-11	72.088
334a-04	55.873
10-AI-87B	50.052
10-AI-RHY	43.625
339b1-11	55.368
216e-11	53.477
2161b-11	68.414
319-1-11	58.294
305b-04	50.721
306-1-04	59.082
309-2-04	23.756
355cxA-11	63.149
355cxC-11	30.402
355c2-11	74.653
355c3-11	47.188

$$AI = [(100*(K_2O+MgO))/(K_2O+MgO+Na_2O+CaO)]$$

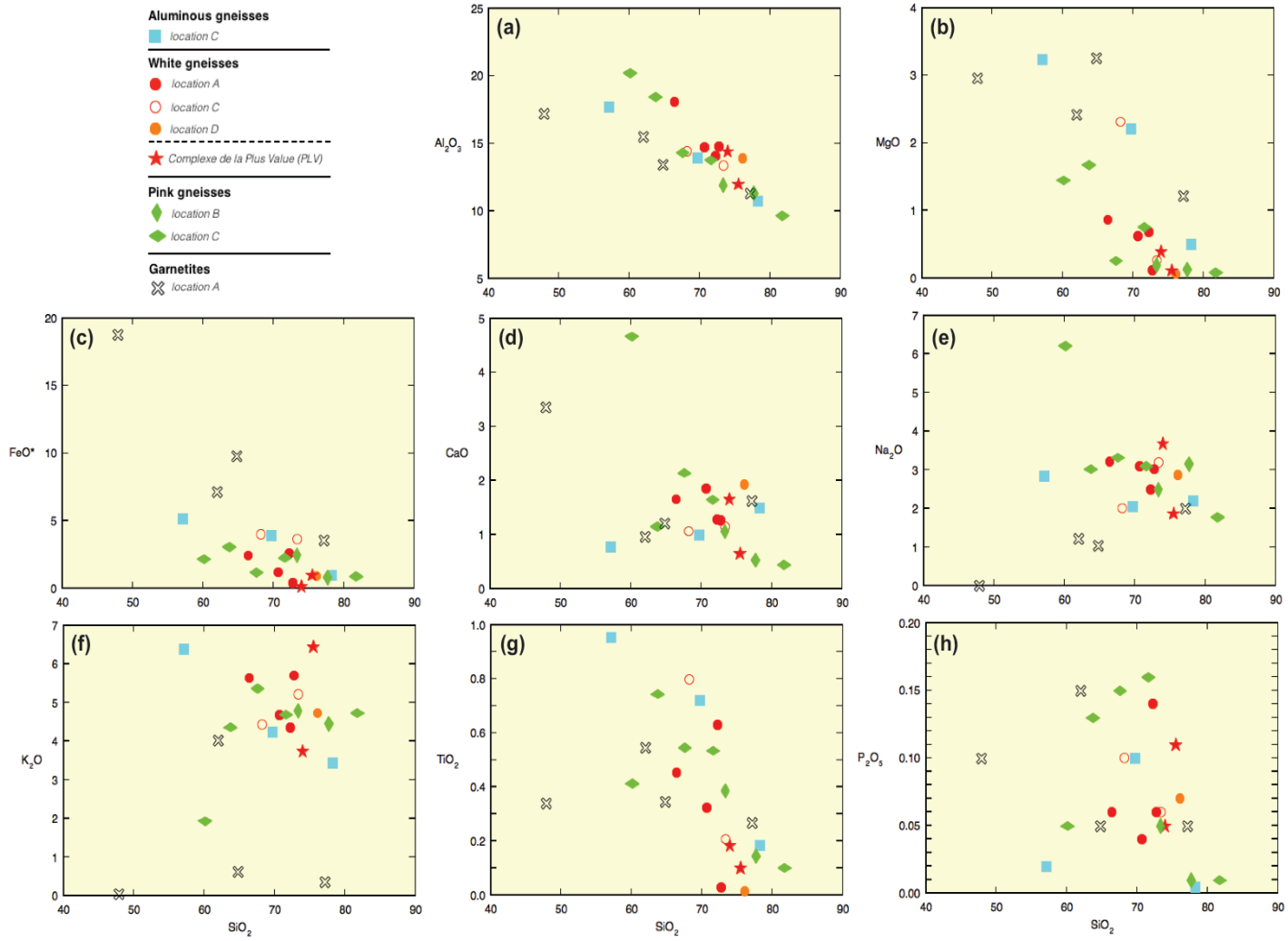

Figure 7.1: Harker plots of major oxides plotted against SiO_2 (in terms of oxide wt%).

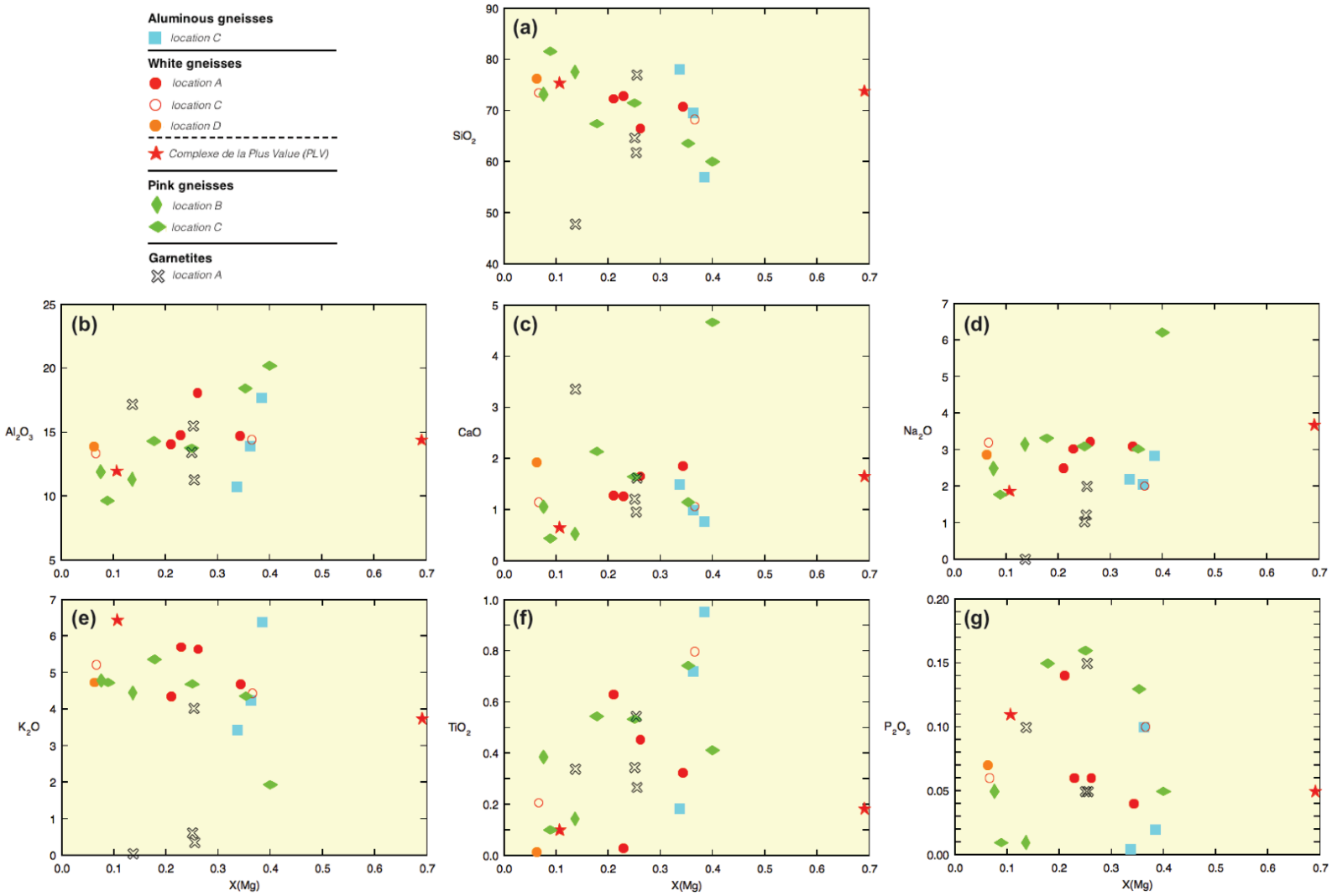

Figure 7.2: Harker plots of major oxides plotted against X(Mg; in terms of oxide wt%).

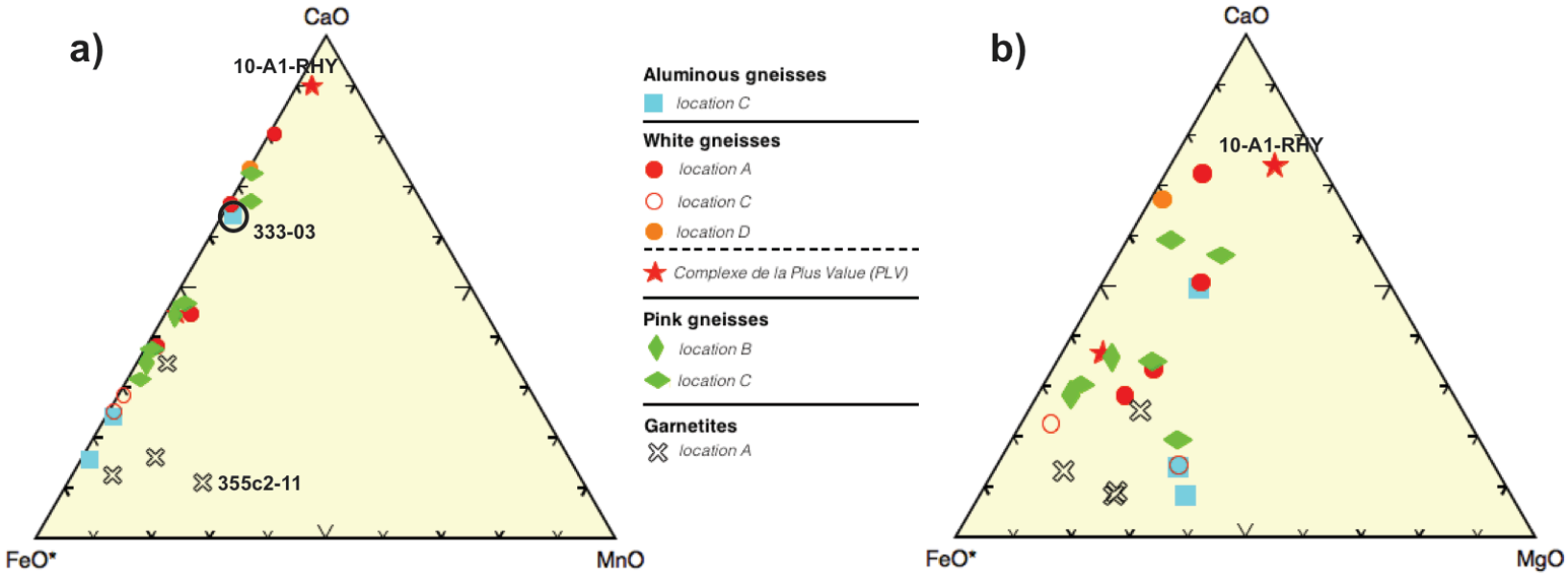

Figure 7.3: Ternary plots of major oxides (in terms of mol%): **(a)** FeO*-CaO-MnO; and **(b)** FeO*-CaO-MgO.

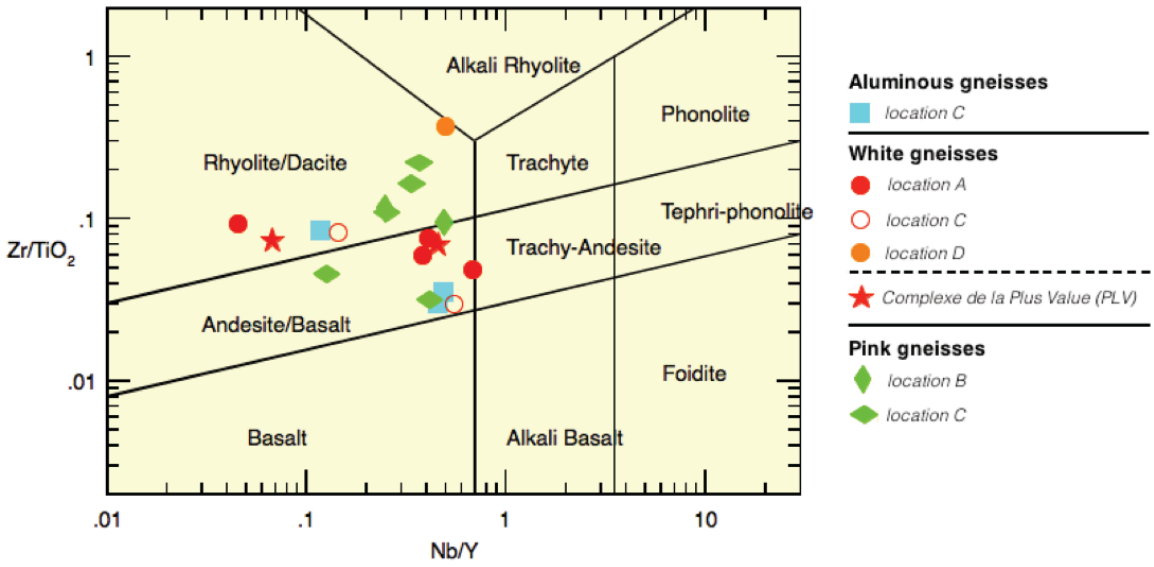

Figure 7.4: Protoliths of aluminous, white and pink gneisses, based on ratios of Nb/Y (ppm)-Zr/TiO_2 (ppm/oxide wt%; revised Winchester and Floyd 1977; Pearce 1996).

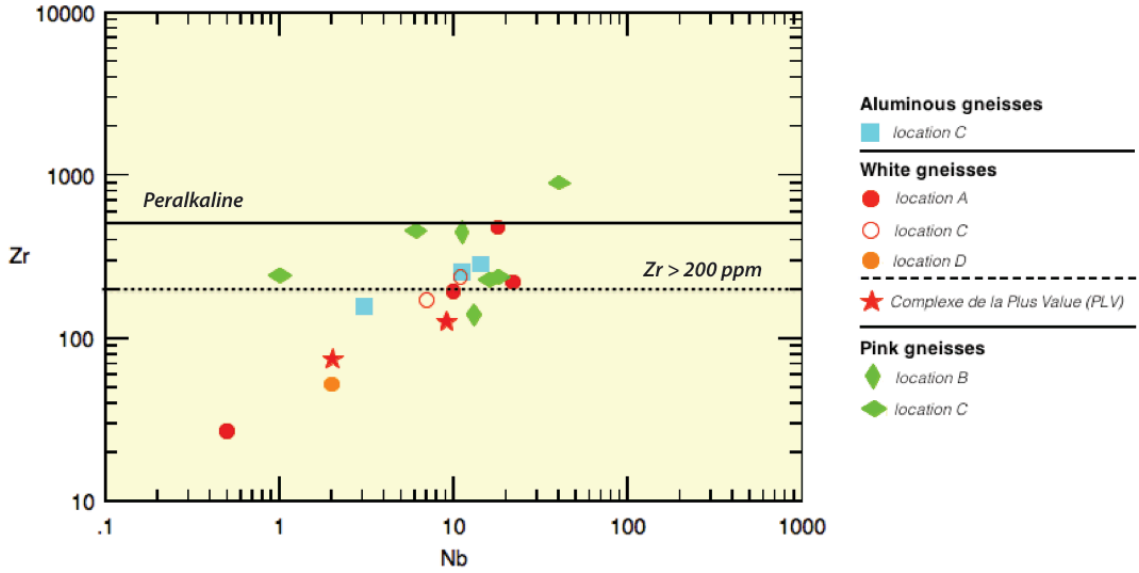

Figure 7.5: Ratios of Nb-Zr from aluminous, white, and pink gneisses (in terms of ppm; modified after Piercey 2010).

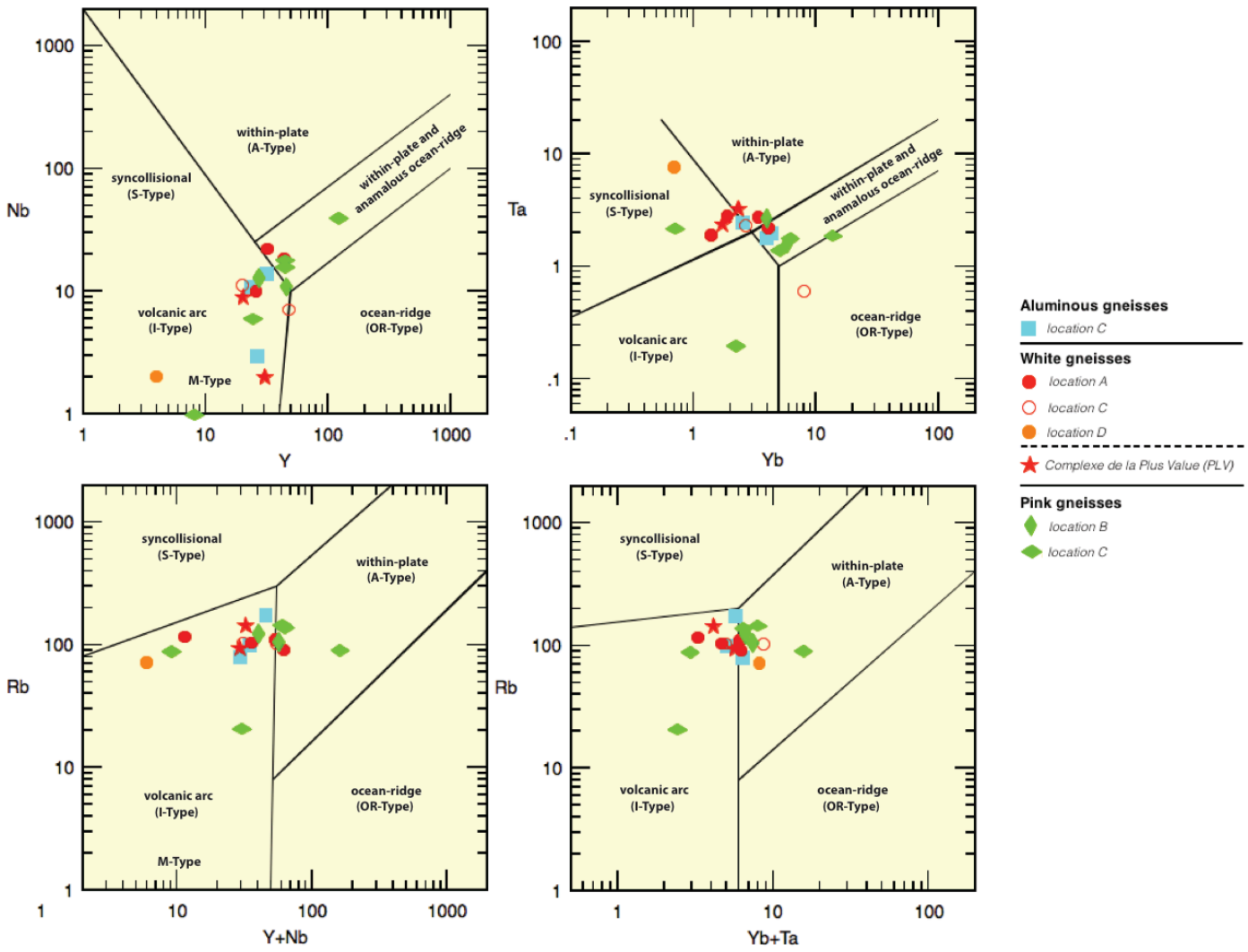

Figure 7.6: Y-Nb, Yb-Ta, Y+Nb-Rb and Yb+Ta-Rb ratios from aluminous, white, and pink gneisses (in terms of ppm; Pearce *et al.* 1984).

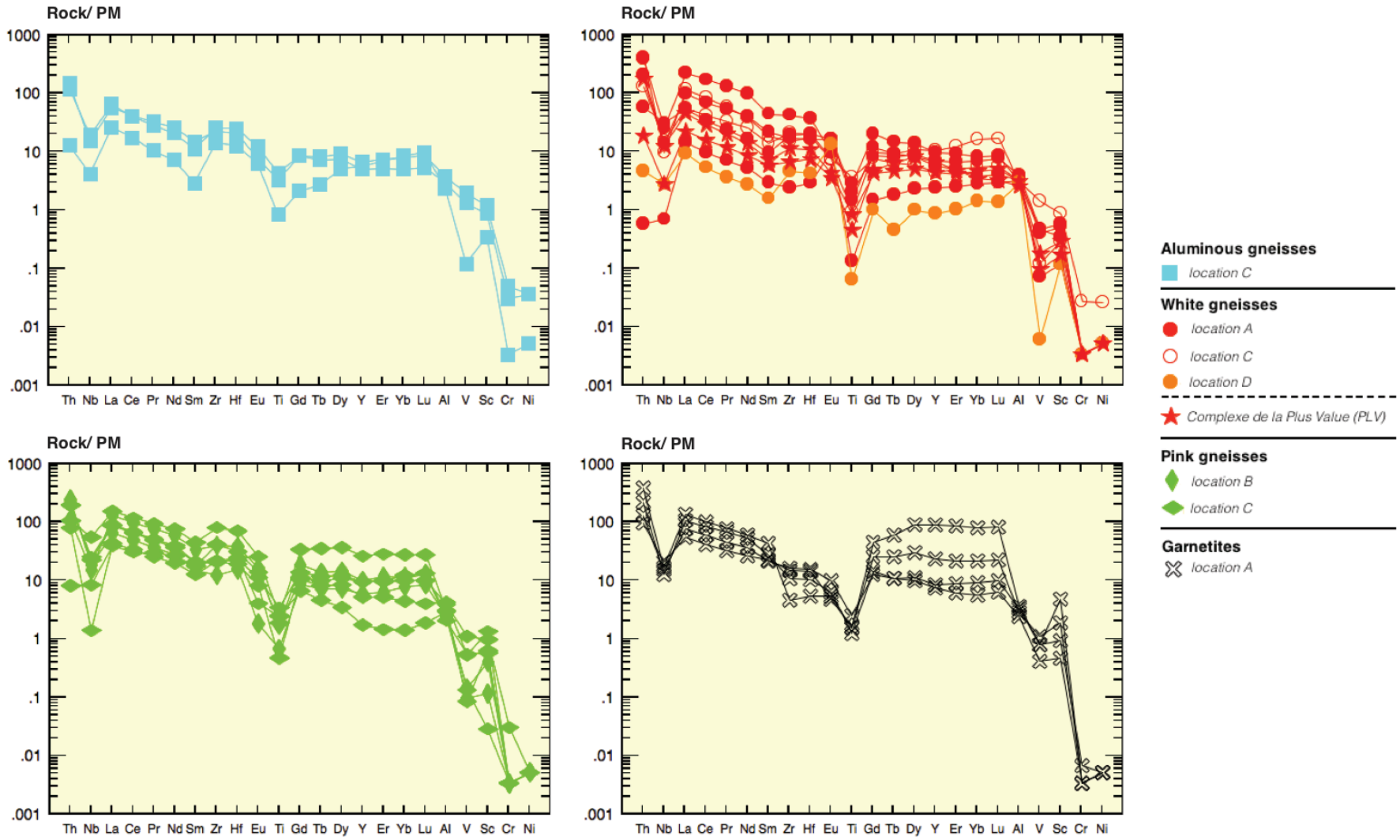

Figure 7.7: Extended primitive mantle (PM) normalized plots showing rare-earth element (REE) signatures for all the examined lithologies of the LBS (normalization after Sun and McDonough 1989).

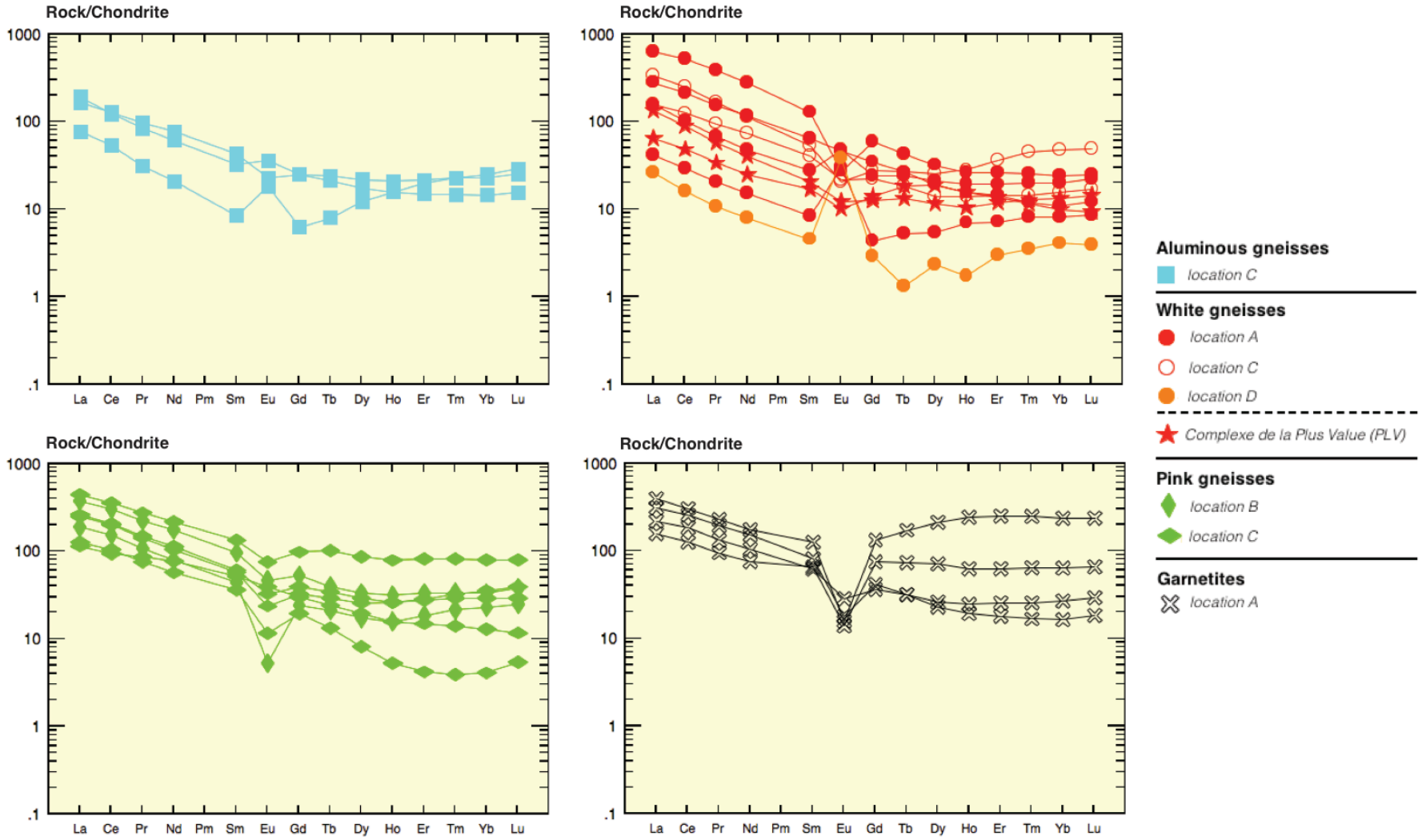

Figure 7.8: Chondrite-normalized plots showing rare-earth element (REE) signatures for all the examined lithologies of the LBS (normalization after Sun and McDonough 1989).

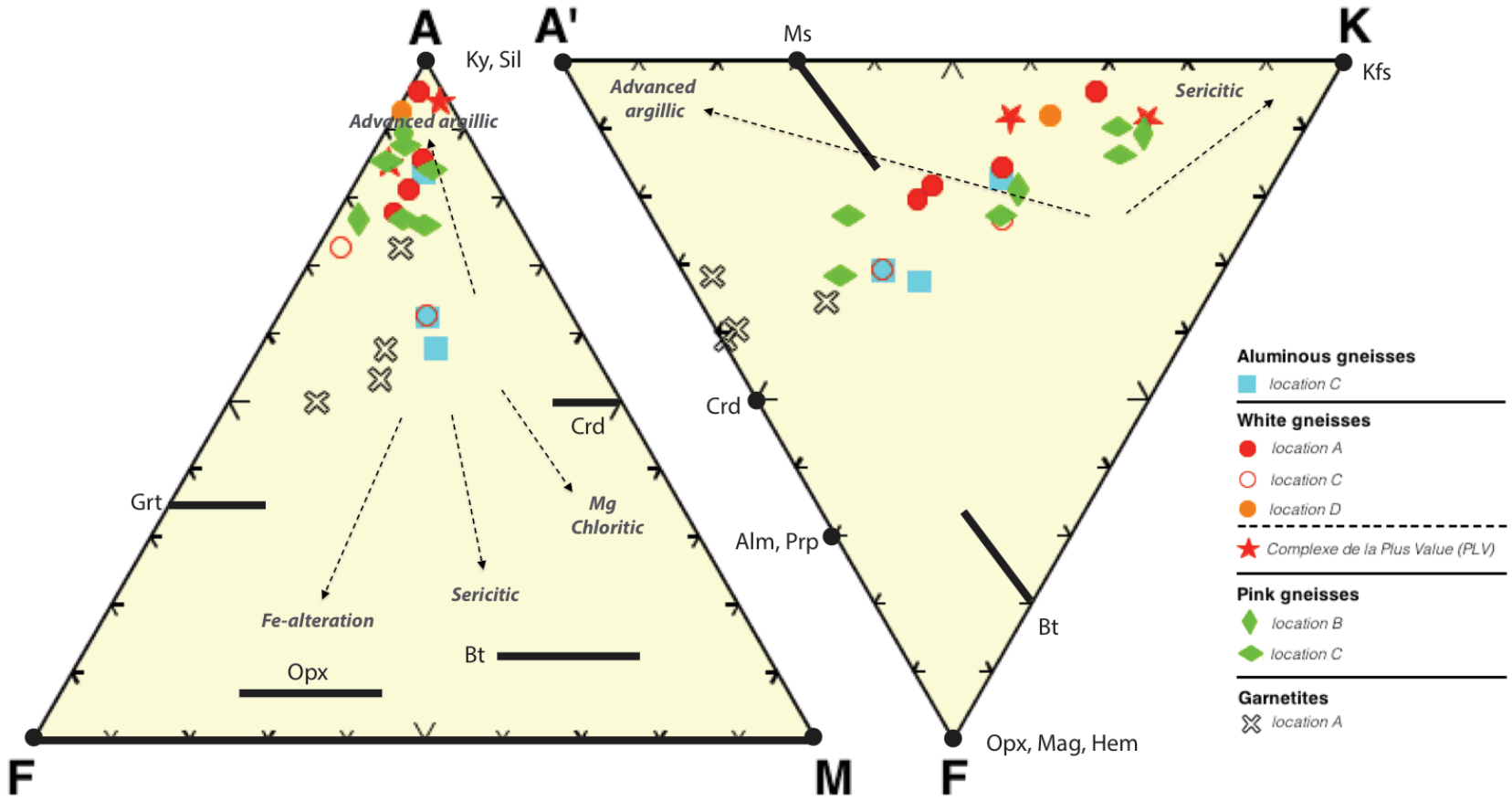

Figure 7.9: Ternary plots AFM and A'KF modeling alteration of the metamorphic mineral assemblage (in terms of mol%) for all the examined lithologies of the LBS (after Bonnet and Corriveau 2007). **AFM** ($A=Al_2O_3-K_2O$, $F=FeO^*$, $M=MgO$) and **A'KF** ($A'=Al_2O_3+FeO^*-K_2O+Na_2O+CaO$, $K=K_2O$, $F=FeO^*+MnO+MgO$).

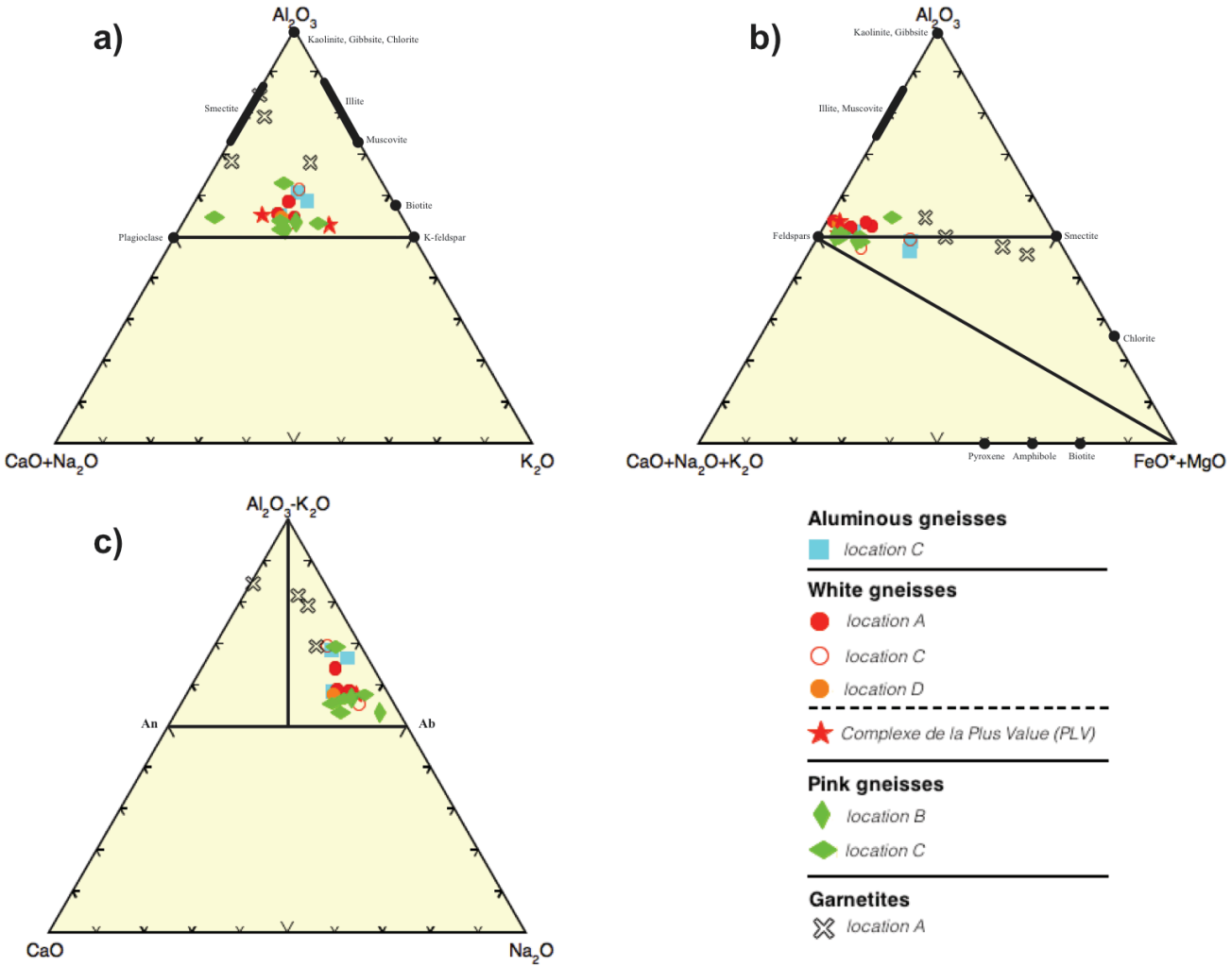

Figure 7.10: Ternary plots showing alteration of feldspars (in terms of mol%) for all the examined lithologies of the LBS (after Nesbitt and Young 1984; Fedo *et al.* 1995). **(a)** Chemical index of alteration (CIA) Al_2O_3-CaO+Na_2O-K_2O; **(b)** Al_2O_3-CaO+Na_2O+K_2O-FeO*+MgO (CIA); and **(c)** plagioclase index of alteration (PIA) $Al_2O_3K_2O$-CaO-Na_2O.

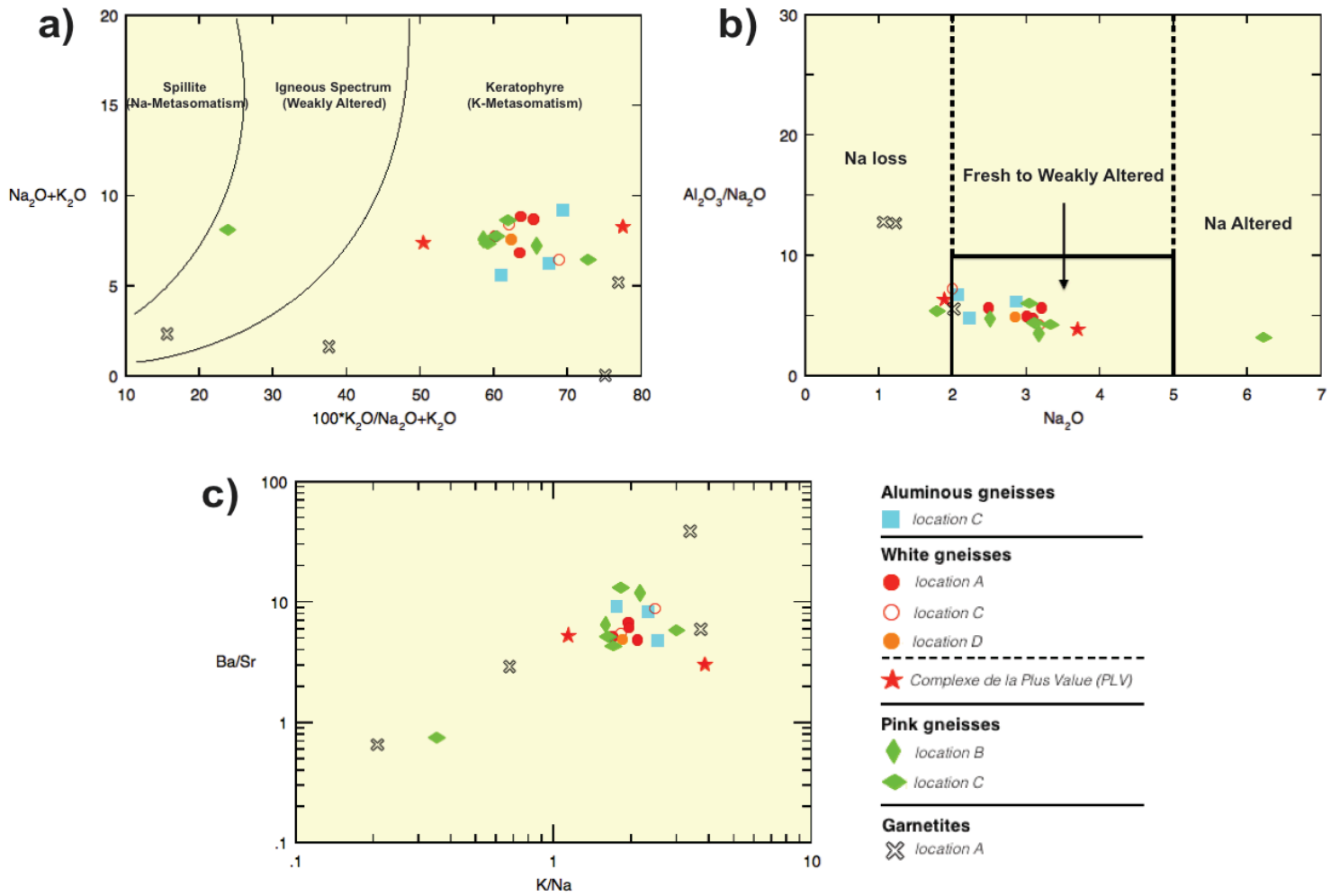

Figure 7.11: Hydrothermal alteration showing gains or losses in mobile and immobile elements for all the examined lithologies of the LBS (in terms of oxide wt%). **(a)** Hughes (1973) spillitized and keratophyric alteration of igneous protoliths; **(b)** Spitz-Darling Index (1978) deriving the losses and/ or gains in Na; and **(c)** K/Na-Ba/Sr ratios.

Chapter 8: DISCUSSION AND CONCLUSIONS

8.1 DISCUSSION

The LBS is a ~1.25 Ga layered felsic-mafic bimodal sequence recently identified in the hinterland of the central Grenville Province, which cuts across ~1.4 Ga units of the Canyon domain in the Manicouagan area. After formation, this portion of the hinterland was metamorphosed under mid-*P* granulite-facies conditions during the culmination of the Grenvillian orogeny (Dunning and Indares 2010; Lasalle *et al.* 2014). Field relations provide hints that the LBS represents the remnants of a rift-related volcanic belt (Indares and Moukhsil 2013). In addition, certain rocks types intercalated within the main sequence (e.g. nodular aluminous gneisses and garnetites), suggest that parts of this belt were subjected to hydrothermal alteration prior to metamorphism.

The detailed petrographic and geochemical study of aluminous, felsic, and pink gneisses, as well as garnetites from presumed hydrothermally altered zones within the LBS has revealed that features inherited from the protoliths, and evidence of subsequent hydrothermal alteration, were preserved despite its granulite-facies metamorphic overprint.

8.1.1 Insights from Petrography

Relict textures suggestive of the protolith are mainly those of recrystallized, resorbed and variably flattened quartz phenocrysts that preserve a bipyramidal shape, and which were observed within a finer-grained matrix in the aluminous gneisses (refer to Figs. 5.17a-5.17c). In addition, flattened aggregates of biotite may be derived from volcanic ash (refer to Figs. 5.17d-5.17e). Features such as these mentioned above have been reported from the upper-amphibolite Hores Gneiss at Broken Hill (Stevens and

Barron 2002), but this is the first time that they have been interpreted as such in rocks metamorphosed well into the granulite-facies.

Textural evidence of hydrothermal activity prior to metamorphism is most convincing in the aluminous gneisses and garnetites. The former contain aluminous nodules, seams of sillimanite, variably disconnected concordant quartz veins, and high amounts of K-feldspar most predominant in the matrix (refer to Figs. 5.18a-5.18c). In addition, the gradational garnetitization of the white gneiss is consistent with the migration of hydrothermal fluids in felsic rocks producing new garnet-rich lithologies (refer to Fig. 5.18d). Similar features reported in the literature include: (a) aluminous nodules and veins in the quartzofeldspathic and aluminous gneisses from La Romaine (Bonnet *et al.* 2005); and (b) garnetite rocks at Broken Hill (Spry and Wonder 1989).

The observed metamorphic mineral assemblage: garnet-sillimanite-biotite-quartz-K-feldspar-plagioclase, and textural evidence of partial melting in the aluminous gneisses of the LBS is consistent with a mid-*P* granulite-facies metamorphic overprint. More specifically, composite inclusions within garnet (which include sillimanite) enclosing pools of former melt, and sillimanite overgrown by garnet, are consistent with the dehydration melting of biotite by the reaction: biotite + Al-silicate + quartz → garnet + melt + K-feldspar ([R2]; Spear *et al.* 1999]), while biotite corroding garnet is consistent with the back reaction during melt crystallization. The inferred P-T path is a tight loop constrained between the kyanite-sillimanite transition and the cordierite-in line at lower-*P* (refer to Fig. 5.19 and after Spear *et al.* 1999; Lasalle *et al.* 2014).

8.1.2 Insights from Mineral Chemistry

Garnet compositions in aluminous gneisses, white gneisses, and garnetites of the LBS have contrasting proportions of Fe, Mg, and Mn (and in some cases Ca) contents.

Aluminous gneisses are the most Fe-rich, white gneisses are the most Mg-rich, and the highest proportions of Mn occurring in the garnetites (refer to Fig. 6.4), which are attributed to circulation of hydrothermal fluids (Borchert 1980; Spry and Wonder 1989; Heimann *et al.* 2011). The relatively high contents of Zn in spinel inclusions (Fig. 6.7) are slightly elevated in comparison with Fe-bearing spinel of typical granulite-facies rocks (Spry and Wonder 1989; Spry *et al.* 2007; Heimann *et al.* 2011). For instance, the most famous garnetites at Broken Hill typically have a manganoan (Mn+Ca) garnet composition and contain the highest contents of Zn, which is inferred to be the result of ore-forming fluid mixed with seawater (Spry and Wonder 1989; Spry *et al.* 2007). In addition, Ba and F in biotite of the nodular aluminous gneisses, and Ba in K-feldspar of some homogeneous aluminous gneisses, white gneisses, and garnetites are indicative of enrichment of the rock composition in these elements, most probable by hydrothermal fluids. More commonly, bulk contents of minor/ trace elements (i.e. Ba, Sr, F, or Cl) in volcanic rocks hosted in VMS settings typically increase towards the central alteration zones of the convective hydrothermal system (Large *et al.* 1992).

8.1.3 Insights from Geochemistry

Based on immobile elements, the volcanic protoliths of the aluminous, white, and pink gneisses of the LBS are inferred to be in the range of rhyolite/dacite to andesite/basalt, with non-peralkaline (i.e. calc-alkalic) affinities (refer to Figs. 7.4-7.5). The inferred chemical protoliths for these rocks is most consistent with formation in an arc to rifted arc setting, and correlative with an inferred recorded Geon 12 intra-continental rift setting in the Manicouagan area (Valverde Cardenas *et al.* 2012; Indares and Moukhsil 2013; Lasalle *et al.* 2013). Extended primitive mantle (PM) and chondrite-normalized REE profiles show that these rocks are enriched in LREE, relatively flat in

HREE, depleted in Nb relative to Th and La, and low in Eu, Ti, V, Cr, which is consistent with the rocks having tholeiitic to calc-alkalic affinities and likely having formed in an arc to rifted arc setting (refer to Figs. 7.6-7.8). Chondrite-normalized plots show positive to negative Eu anomalies, suggesting variable degrees of plagioclase dissolution during alteration. Furthermore, REE profiles of these rocks are very similar to those of massive sulfide-associated felsic volcaniclastic rocks from La Romaine (Bonnet *et al.* 2005) and garnetite rocks at Broken Hill (Spry *et al.* 2007).

Enrichment in Al and K, most notable in aluminous, white, and pink gneisses with high amounts of K-feldspar and/ or Al-silicates, is attributed to sericitic and argillic alteration types (refer to Fig. 7.9). The alteration index (AI) for most of these samples have values >50, suggesting alteration by hydrothermal fluids (Large *et al.* 1992, 2001). Such alterations have been also recognized in other granulite-facies terranes (e.g. La Romaine, Bonnet *et al.* 2005).

The hydrothermally altered rocks of the LBS exhibit evidence of K-metasomatism and depletion in Na (refer to Fig. 7.11). This is inferred from the geochemistry of these rocks, and is likely linked to the sericitization of K-feldspar and dissolution of plagioclase (i.e. Na-depletion) during fluid circulation (Galley 1993, 1995; Sillitoe *et al.* 1996; Gifkins *et al.* 2005). In addition, depletion in major elements (i.e. Ca and Na) is consistent with the negative Eu anomalies and with dissolution of plagioclase during alteration (Bonnet *et al.* 2005). However, the Mn-rich garnetites are the most Fe+Mg bearing and Na+Ca+K depleted. Furthermore, increasing ratios of K/Na-Ba/Sr in gneisses with high amounts of K-feldspar and/ or Al-silicates and the low K Mn-rich garnetites, are inferred to characterise the more proximal altered zones of the convective hydrothermal system (see Large *et al.* 1992).

More commonly, increased contents of Al, K, immobile and trace elements are attributed to seafloor alteration, common in VMS environments (Franklin *et al.* 1981; Lydon 1988; Spry and Wonder 1989; Large *et al.* 1992; Hannington *et al*. 2005). In addition, increased Al, LFSE, and trace contents in the garnetites at Broken Hill are found most proximal to orebodies in the area (Stanton 1976; Barnes *et al.* 1983; Spry and Wonder 1989), and are inferred to be the product of a Mn-rich sediment hydrothermally altered at or near the seafloor (Schwandt *et al.* 1993; Spry *et al.* 2007).

8.2 CONCLUSIONS

Recent studies have shown that hydrothermally altered volcanic belts have the potential to preserve diagnostic features, even when transformed into high-grade metamorphic terranes (e.g. Broken Hill – Spry and Wonder 1989; La Romaine – Bonnet *et al.* 2005; Bonnet and Corriveau 2007). The petrographic and geochemical study described in thesis documents a new example of granulite-facies remnants of a volcanic belt (LBS) with local hydrothermally altered zones (HAZ) from the central Grenville Province, and builds on the work above.

The highlights of this study are:

(i) the identification of relics of bipyramidal quartz phenocrysts attesting to a volcanic precursor, and the recognition of potential relict pathways of hydrothermal fluids in the form of aluminous nodules, silimanite seams, and concordant quartz veins in aluminous gneisses (imaging of these textures was highly facilitated by SEM-MLA mapping);

(ii) the slightly elevated and unusual contents of Mn, Zn, Ba, and F in the mineral chemistries of garnet, spinel, and feldspar(s), suggests alteration by hydrothermal fluid activity;

(iii) the geochemical inference of the protolith being rhyolite/dacite to basalt/andesite in composition with tholeiitic to calc-alkalic affinities, formed in an arc to rifted arc setting;

(iv) the documentation of enrichments in Al and K in aluminous, white, and pink gneisses most consistent with sericitic and argillic alteration;

(v) the geochemical constraints of hydrothermal alteration for samples having K-metasomatism, Na-depletion, and AI values >50, which suggests sericitization of K-feldspar and dissolution of plagioclase during fluid circulation; and

(vi) the increase in K (with the exception of the low K Mn-rich garnetites), Al, immobile, and trace elements, is consistent with formation via seafloor alteration most common to VMS environments.

Bibliography

Allard, G.O. and Carpenter, R.H. 1988. Mineralogical anomalies in metamorphosed terrain, a neglected but promising exploration tool. International Conference on the Geochemical Evolution of the Continental Crust, Pocos de Cladas, Brazil, pp. 229-236.

Allard, G.O. 1978. Pétrologie et potentiel économique du prolongement du sillon de roches vertes de Chibougamau dans la Province de Grenville. Ministère des Richesses naturelles, Québec, DPV-604.

Barrett, T.J., and MacLean, W.H. 1994. Chemostratigraphy and hydrothermal alteration in exploration for VHMS deposits in greenstone and younger volcanic rocks. *In* Alteration and alteration processes associated with ore-forming systems. E.R., Lentz *(eds.)*. Geological Association of Canada, Short Course Notes **11**, pp. 433-467.

Barnes, R.G., Stevens, B.P.J., Stroud, W.J., Brown, R.E., Willis, I.L., and Bradley G.M. 1983. Zinc, manganese, and iron-rich rocks and various minor rock types. Geological Survey of New South Wales Records, **21**: 289-323.

Barrie, C.T., and Hannington, M.D., 1999. Classification of volcanic-associated massive sulfide deposits based on host-rock composition. Reviews in Economic Geology, **8**: 1–11.

Blein, O., Corriveau, L., and LaFlèche, M.R., 2004. Cordierite-orthopyroxene white gneiss: A key to unveiling pre-metamorphic hydrothermal activity in the Bondy gneiss complex, Grenville Province, Québec. *In* Proterozoic Tectonic Evolution of the Grenville Orogen in eastern North America. R., Tollo, L., Corriveau, J., McLelland, and M., Bartholomew (*eds*.). Geological Society of America, Memoir **197**, pp. 19-33.

Bonnet, A.-L., and Corriveau, L. 2007. Alteration vectors to metamorphic hydrothermal systems in gneissic terranes. *In* Mineral Deposits of Canada: A Synthesis of Major Deposit-Types, District Metallogeny, the Evolution of Geological Provinces, and Exploration Methods. W.D. Goodfellow *(eds.)*. Geological Association of Canada, Mineral Deposits Division, Special Publication **5**, pp. 1035-1049.

Bonnet, A.-L., Corriveau, L., and LaFlèche, M.R. 2005. Chemical imprint of highly metamorphosed volcanic-hosted hydrothermal alternations in the Romaine Supracrustal Belt, eastern Grenville Province, Quebec. *In* The Grenville Province: a geological and mineral resource perspective derived from government and academic research initiatives. J. Greenough *(eds.)*. Canadian Journal of Earth Sciences, **42**: 1783-1814. doi: 10.1139/E05-098.

Bonnet, A.-L., and Corriveau, L. 2003. Caractérisation structural et métamorphique de la marge sud-est du Groupe de Wakeham, régions du lac Musquaro et de La Romaine, Province de Grenville (Québec, Canada). Geological Survey of Canada, Paper **2003-C17.**

Borchet, H. 1980. On the genesis of manganese ore deposits. *In* Manganese deposits on continents. Varentsov, I.M. and Grasselly, G.Y. *(eds.)*. Schweizerbart'sche Verlagsbuchhandlung, Stuttgart, pp. 45-60.

Corbett, G.J., and Leach, T.M. 1998. Southwest Pacific Rim Gold-Copper Systems: Structure, Alteration, and Mineralization. Society of Economic Geologists, Special Publication **6**, pp. 236.

Corriveau, L., and Bonnet, A.-L. 2005. Pinwarian (1.50 Ga) volcanism and hydrothermal activity at the eastern margin of the Wakeham Group, Grenville Province, Quebec. Canadian Journal of Earth Sciences, **42**: 1749-1782. doi:10.1139/E05-086.

Corriveau, L., Bonnet, A-L., van Breemen, O., and Pilote, P. 2003. Tracking the Wakeham Group volcanic rocks and associated copper-iron oxide hydrothermal activity from La Romaine eastward, eastern Grenville Province, Quebec. Geological Survey of Canada, Current Research **2003-C12**, pp. 11.

Droop 1987. A general equation for estimating Fe^{3+} concentrations in ferromagnesian silicates and oxides from microprobe analyses, using stoichiometric criteria. Mineralogical Magazine, **51**: 431-435.

Dunning, G., and Indares, A. 2010. New insights on the 1.7 – 1.0 Ga crustal evolution of the central Grenville Province form the Manicouagan – Bair Comeau transect. Precambrian Research, **180**: 204-226. doi: 10.1016/j.precamres.2010.04.005.

Fedo, C.M., Nesbitt, H.W., Young, G.M. 1995. Unraveling the effects of potassium metasomatism in sedimentary rocks and paleosoils, with implications for paleoweathering conditions and provenance. Geology, **23**: 921-924.

Franklin, J.M., Gibson, H.L., Jonasson, I.R., and Galley, A.G. 2005. Volcanogenic massive sulfide deposits. Society of Economic Geologists, **100**: 523-560.

Franklin, J.M., Lydon, J.W., and Sangster, D.F. 1981. Volcanic-Associated Massive Sulphide Deposits. Economic Geology 75th Anniversary Volume, pp. 485-627.

Galley, A.G., Hannington, M.D., and Jonasson, I.R. 2007. Volcanogenic massive sulphide deposits. *In* Mineral Deposits of Canada: A Synthesis of Major Deposit-Types, District Metallogeny, the Evolution of Geological Provinces, and Exploration Methods: Geological Association of Canada. W.D. Goodfellow *(eds.)*. Mineral Deposits Division, Special Publication, **5**, pp. 141-161.

Galley, A.G. 1995. Target vectoring using lithogeochemistry: applications to the exploration for volcanic-hosted massive sulphide deposits. Canadian Institute of Mining Bulletin, **88**: 15-27.

Galley, A.G., Watkinson, D.H., Jonasson, I.R., and Riverin, G. 1995. The subsea-floor formation of volcanic-hosted massive sulphide: Evidence from the Ansil deposit, Rouyn-Noranda, Canada. Economic Geology, **90**: 2006-2017.

Galley, A.G. 1993. Characteristics of semi-conformable alteration zones with volcanogenic massive sulphide districts. Journal of Geochemical Exploration, **48**: 175-200.

Gauthier, M., Morin, G., and Marcoux, P. 1985. Minéralisations aurifères de la partie centrale de la Province de Grenville, Bouclier Canadien. Canadian Mining and Metallurgy Bulletin, **78**: 60-69.

Gibson, H.L., Allen, R.L., Riverin, G., and Lane, T.E. 2007. The VMS Model: Advances and Application to Exploration Targeting. Ore Deposits and Exploration Technology, **49**: 713-730.

Gifkins, C., Herman, W., and Large, R. 2005. Altered volcanic rocks: a guide to description and interpretation. Centre for Ore Deposit Research (CODES), University of Tasmania, Hobart, Australia, pp. 241-246.

Gobeil, A., Brisebois, D., Clark, T., Verpaelst, P., Mador, L., Wodicka, N., and Chevé, S. 2003. Synthèse géologique de la région de Manitou–Wakeham (Moyenne-Côte-Nord). *In* Géologie et ressources minérales de la partie orientale de la Province Grenville. D. Brisebois and T. Clark (*eds*.). Ministère des Ressources naturelles de la Faune et des Parcs, Québec, DV-2002-03, pp. 9–58.

Gobeil, A., 1997a. Géologie de la région du Lac Lacoursiere. Ministère des Ressources naturelles, Québec. RG 96-03, pp. 14.

Gobeil, A., 1997b. Géologie de la région du Lac Grandmesnil. Ministère des Ressources naturelles, Québec. RG 96-04, pp. 10.

Gu, Y. 2003. Automated scanning electron microscope based mineral liberation analysis. Journal of Minerals & Materials Characterization & Engineering, **2**: 33-41.

Hannington, M.D., Jamieson, J., Monecke, T., Petersen, S., and Beaulieu, S. 2011. The abundance of seafloor massive sulfide deposits. Geological Society of America, **39**(2): 1155-1158. doi: 10.1130/G32468.1.

Hannington, M.D. 2009. Modern Submarine Hydrothermal Systems – A Global Perspective on Distribution, Size, and Tectonic Settings. *In* Submarine Volcanism and Mineralization: Modern through Ancient. B. Cousens and S. J., Piercey (*eds*.). Short course 29-30 May 2008, Quebec City, Canada, **19**: 1189-6094.

Hannington, M.D., de Ronde, C.E.J., and Petersen, S., 2005. Sea-floor tectonics and submarine hydrothermal systems. Economic Geology 100th Anniversary Volume, Society of Economic Geologists, pp. 111–141.

Hannington, M.D., Kjarsgaard, I.M., Galley, A.G., and Taylor, B. 2003. Mineral-chemical studies of metamorphosed hydrothermal alteration in the Kristineberg volcanogenic 668 massive sulfide district, Sweden. Mineralium Deposita, **38**: 423-442.

Hannington, M.D. 1999. Volcanogenic gold in the massive sulfide environment volcanic-associated massive sulfide deposits: Processes and examples in modern and ancient settings. Reviews in Economic Geology, **8**: 325-356.

Hannington, M.D., Tivey, M.K., Larocque, A.C.L., Petersen, S., and Rona, P.A. 1995. The occurrence of gold in sulfide deposits of the TAG hydrothermal field, mid-Atlantic ridge. The Canadian Mineralogist, **33**: 1285-1310.

Hawkins, B.W. 1968. A quantitative chemical model of the Broken Hill lead-zinc deposit (with discussion). Australasian Institute of Mining and Metallurgy, **227**: 11-15.

Heimann, A., Spry, P., Teale, G.S., Conor, C.H.H., and Pearson, N.J. 2011. The composition of garnet in garnet-rich rocks in the southern Proterozoic Curnamona Province, Australia: an indicator of the premetamorphic physicochemical conditions of formation. Mineralogy and Petrology, **101**(1-2): 49-74. doi:10.1007/s00710-010-0130-x.

Hedenquist, J.W., Arribas, A., and Gonzalez-Urien, E. 2000. Exploration for epithermal gold deposits. Reviews in Economic Geology, **13**: 245-277.

Hodges, D.J., and Manojlovic, P.M. 1993. Application of lithogeochemistry to exploration for deep VMS deposits in high-grade metamorphic rocks, Snow Lake, Manitoba. Journal of Geochemical Exploration, **48**: 201-224.

Hodych, J.P., and Dunning, G.R. 1992. Did the Manicouagan impact trigger end-of-Triassic mass extinction? Geology, **20**: 51–54.

Holness, M.B., Cesare, B., and Sawyer E.W. 2011. Melted Rocks under the Microscope: Microstructures and Their Interpretation. Elements, **7**: 247-252.

Hughes, C.J. 1973. Spilites, keratophyres, and the igneous spectrum. Geological Magazine, **109**: 513-527.

Hynes, A., Indares, A., Rivers, T. and Gobeil, A. 2000. Lithoprobe line 55: integration of out-of phase seismic results with surface structure, metamorphism and geochronology, and the tectonic evolution of the eastern Grenville Province. Canadian Journal of Earth Sciences, **37**: 341–358.

Indares, A., and Moukhsil, A. 2013. Ca. 1.2 Ga crustal extension in the central Grenville Province, implications for the orogenic architecture and potential influence on the emplacement of anorthosites. Canadian Journal of Earth Sciences, (***in press)***.

Indares A., White, R.W., and Powell, R. 2008. Phase equilibria modelling of kyanite-bearing anatectic paragneisses from the central Grenville Province**.** Journal of Metamorphic Geology, **26**: 815–836.

Indares, A., and Dunning, G. 2004. Crustal architecture above the high-pressure belt of the Grenville Province in the Manicouagan area: new structural, petrologic and U–Pb age constraints. Precambrian Research, **130**: 199-208. doi: 10.1016/j.precamres.2003.11.005.

Indares, A., Dunning, G., and Cox, R. 2000. Tectono-thermal evolution of deep crust in a Meso-proterozoic continental collision setting: the Manicouagan example. Canadian Journal of Earth Sciences, **37**: 325-340.

Ishikawa, Y., Sawaguchi, T., Iwaya, S., and Horiuchi, M. 1976. Delineation of prospecting targets for Kuroko deposits based on modes of volcanism of underlying dacite and alteration halos. Mining Geology, **26**: 105-117.

Johnson, I.R., and Klingner, G.D. 1975. The Broken Hill ore deposit and its environment. *In* Economic geology of Australia and Papua New Guinea. C.L. Knight (*eds.*). Australasian Institute of Mining and Metallurgy Monograph **5**, pp. 476-495.

Laing, W.P. 1996. Volcanic related origin of the Broken Pb+Zn+Ag deposit, Australia. *In* New Developments in Broken Hill Type Deposits CODES, Special Publication **1**, pp. 53-66.

Laing, W.P., Sun, S-S., and Nesbitt, R.W. 1984. Acid volcanic precursor to Potosi Gneiss at Broken Hill and its implication for ore genesis. Seventh Australian Geological Convention, Sydney, Geological Society of Australia, Abstracts, **12**: 318-321.

Lasalle, S., and Indares, A. 2014. Anatextic record and contrasting *P-T* paths from aluminous gneisses in the central Grenville Province. Journal of Metamorphic Geology, ***in press***.

Lasalle, S., Fisher, C.M., Indares, A., and Dunning, G. 2013. Contrasting types of Grenvillian granulite facies aluminous gneisses: Insights on protoliths and metamorphic events from zircon morphologies and ages. Precambrian Research, **228**: 117-130.

Large, R.R. 1992. Australian volcanic-hosted massive sulphide deposits: Features, styles, and genetic models. Economic Geology, **87**: 469–968.

Large, R.R., Gemmell, J.B., Paulick, H. 2001. The Alteration Box Plot: A simple approach to understanding the relationship between alteration mineralogy and lithogeochemistry associated with volcanic-hosted massive sulfide deposits. Economic Geology, **96**: 957-971.

Large, R.R., Allen, R.L., Blake, M.D., and Herrmann, W. 2001a. Hydrothermal alteration and volatile element halos for the Rosebery K Lens volcanic-hosted massive sulphide deposit, western Tasmania. Economic Geology, **96**: 1055–1072.

Large, R.R., McPhie, J., Gemmell, J.B., Herrmann, W., and Davidson, G.J. 2001b. The spectrum of ore deposit types, volcanic environments, alteration halos, and related exploration vectors in submarine volcanic successions: Some examples from Australia. Economic Geology, **96**: 1037–1054.

Lydon, J.W. 1988. Ore deposit models: Volcanogenic massive sulfide deposits. Part 2: Genetic models. Geoscience Canada, **15**: 43–65.

Lydon, J.W. 1984. Ore deposit models: Volcanogenic massive sulfide deposits. Part 1: A descriptive model. Geoscience Canada, **11**: 195–202.

McLennan, S.M., Bock, B., Hemming, S.R., Hurowitz, J.A., Lev., S.M., and McDaniel, D.K. 2003. The roles of provenance and sedimentary processes in the geochemistry of sedimentary rocks. *In* Geochemistry of Sediments and Sedimentary Rocks: Evolutionary Considerations to Mineral Deposit-Forming Environments. D.R. Lentz (*eds*.). Geological Association of Canada, GeoText **4**: 7-38.

Moore, J.M. 1986. Introduction: The "Grenville Problem" Then and Now. *In* The Grenville Province. J.M. Moore, A. Davidson, and A.J. Baer *(eds.)*. Geological Association of Canada, Special Paper, **31**: 1-12.

Moukhsil, A., Solgadi, F., Clark, T., Blouin, S., Indares, A., and Davis D.G. 2013. Géologie du nord-ouest de la région du barrage Daniel-Johnson (Manic 5), Côte-Nord. Ministere des Ressources naturelles**, RG 2013-01**, pp. 31.

Moukhsil, A., Fabien, S., Pierre, L,, Marianne, G., and Jean, D. 2012. Géologie de la région du lac du Milieu (SNRC 22O03, 22O04, 22O06, 22J13 et 22J14). Ministère des Ressources naturelles et de la Faune, **RG 2012-01**, pp. 31.

Nesbitt, H.W., and Young, G.M. 1984. Prediction of some weathering trends of plutonic and volcanic rocks based on thermodynamic and kinetic considerations. Geochimica et Cosmochimica Acta, **48**: 1523-1534.

Page, R.W. and Laing, W.P. 1992. Felsic metavolcanic rocks related to the Broken Hill Pb-Zn-Ag orebody, Australia: geology, depositional age, and timing of high-grade metamorphism. Economic Geology, **87**: 2138-2168.

Page, R.W., Stevens B.P.J., and Gibson G.M. 2005a. Geochronology of the sequence hosting the Broken Hill Pb-Zn-Ag orebody: Economic Geology, **100**: 633-661.

Parr, J.M., and Pilmer, I.R. 1993. Models for Broken Hill-type lead-zinc-silver deposits. Geological Association of Canada Special Paper, **40**: 253-288.

Pearce, J.A. 1996. Sources and Settings of Granitic Rocks. Episodes, **19**(4): 120-125.

Pearce, J.A., Harris, N.B.W., and Tindle, A.G. 1984. Trace element discrimination diagrams for the tectonic interpretation of granitic rocks. Journal of Petrology, **25**(4): 956-983. doi: 10.1093/petrology/25.4.956.

Piercey, S.J. 2011. The setting, style and role of magmatism in the formation of volcanogenic massive sulfide deposits. Miner Deposita, **46**: 449-471. doi: 10.1007/s00126-011-0341-z.

Piercey, S.J. 2010. An overview of petrochemistry in regional exploration for volcanogenic massive sulphide (VMS) deposits. Geochemistry: Exploration. Environment, Analysis, **10**: 119-136. doi: 10.1144/1467-7873/09-221.

Piercey, S.J. 2009. Lithogeochemistry of volcanic rocks associated with volcanogenic massive sulphide deposits and applications to exploration. *In* Submarine Volcanism and Mineralization: Modern Through Ancient. B. Cousens and S. Piercey *(eds.)*. Geological Association of Canada, Short Course 29-30 May 2008, Quebec City, Canada, pp. 15-40.

Pidgeon. R.T. 1967. A rubidium-strontium geochronological study of the Willyama Complex, Broken Hill, Australia. Journal of Petrology, **8**: 283-324.

Pilmer, I.R. 2006. Manganoan garnet rocks associated with the Broken Hill Pb-Zn-Ag orebody, Australia. Mineralogy and Petrology, **88**: 443-478. doi: 10.1007/s00710-006-0122-z.

Pilmer, I.R. 1979. Sulphide rock zonation and hydrothermal alteration at Broken Hill, Australia. Trans. Inst. Min. Metall, **88**: B161-176.

Price, J.R., and Velbel, M.A. 2003. Chemical weathering indices applied to weathering profiles developed on heterogeneous felsic metamorphic parent rocks. Chemical geology, **202**: 397-416.

Ohmoto, H. 1996. Formation of volcanogenic massive sulfide deposits: the Kuroko perspective. Ore Geology Reviews, **10**: 135-177.

Riverin, G., and Hodgson, J. 1980. Wall-rock alteration at the Millenbach Cu-Zn Mine, Noranda, Quebec. Economic Geology, **75**: 424-444.

Rivers, T. 2012. Upper-crustal orogenic lid and mid-crustal core complexes: signature of a collapsed orogenic plateau in the hinterland of the Grenville Province. Canadian Journal of Earth Sciences, **49**: 1-42. doi: 10.1139/e11-014.

Rivers, T. 2009. The Grenville Province as a large hot long-duration collisional orogen – insights from the spatial and thermal evolution of it orogenic fronts. *In* Ancient Orogens and Modern Analogues. J.B. Murphy, J.D. Keppie, and A.J. Hynes *(eds.)*. Geological Society of London, Special Publications, **327**: 405-444.

Rivers, T. 2008. Assembly and preservation of lower, mid, and upper orogenic crust in the Grenville Province – Implications for the evolution of large hot long-duration orogens. Precambrian Research, **86**: 117-154.

Rivers, T., Ketchum, J., Indares, A., and Hynes, A. 2002. The High Pressure belt in the Grenville Province: architecture, timing, and exhumation. Canadian Journal of Earth Sciences, **39**(5): 867-893.

Rivers, T. 1997. Lithotectonic elements of the Grenville Province: review and tectonic implications. Precambrian Research, **86**: 117-154.

Rivers, T., Martignole, J., Gower, C.F., and Davidson, A. 1989. New tectonic divisions of the Grenville province, southeast Canadian Shield. Tectonics, **8**(1): 63-84.

Roberts, M.D., Oliver, N.H.S., Fairclough, M.C., Höltta, P.S., and Lahtinen, R., 2003. Geochemical and oxygen isotope signature of sea-floor alteration associated with a polydeformed and highly metamorphosed massive sulfide deposit, Ruostesuo, Central Finland: Economic Geology, **98**: 535-556.

Sawyer, E.W. 1999. Criteria for the recognition of partial melting. Physics and Chemistry of the Earth, **24**: 269-279.

Schwandt, C.S., Papike, J.J., Shearer, C.K., and Brearley, A.J. 1993. Crystal chemical control of REE incorporation in garnets from the Broken Hill Pb-Zn-Ag orebodies, Australia. Canadian Mineralogist, **31**: 371-379.

Shaffer, M. 2009. Discrimination of hematite and magnetite and quantifying their associations using the JKTECH Mineral Liberation Analyzer^{TM}. *In* The 48th Annual Conference of Metallurgists, Laurentian University, Sudbury, Ontario **73**.

Shaffer, M., Gu, Y., and Rohde, M. 2008. Practical Applications for the Silicon Drift X-ray Detector in SEM-Platformed Image Analysis: The Bruker-MLA in Practice. *In* SME Annual Meeting 2007 and CMS 109th National Western Conference 2007 The Power of Mining: Energy's Influence, Denver, CO, U.S.A., 25-28 February, 2007, **1**(Preprint 07-029): 1-6.

Shanks, W.C.I. 2012. Volcanogenic Massive Sulfide Occurrence Model: 11. Hydrothermal Alteration. U.S. Geological Survey, Reston, Virginia. Scientific Investigations Report **2010-5070-C**, pp. 169-178.

Shaw, S.E. 1968. Rb-Sr isotopic studies of the mine sequence at Broken Hill. *In* Broken Hill Mines – 1968. M. Radmanovich and J.T. Woodcock (*eds*.). Australian I.M.M. Melbourne, **3**: 185-198.

Sillitoe, R.H. 2003. Iron oxide-copper-gold deposits: An Andean view. Mineralium Deposita, **38**: 799-815.

Sillitoe, R.H. 2000. Gold-rich porphyry deposits: Descriptive and genetic models and their role in exploration. Reviews in Economic Geology, **13**: 315-345.

Sillitoe, R.H., Hannington, M.D., and Thompson, F.H. 1996. High Sulphidation Deposits in the Volcanogenic Massive Sulfide environment. Economic Geology, **91**: 204-212.

Spear, F.S., Kohn, M.J., and Cheney, J.T. 1999. *P-T* paths from anatextic pelites. Contribution to Mineral Petrology, **134**: pp. 17-32.

Spitz, G., and Darling, R. 1978. Major and minor element lithogeochemical anomalies surrounding the Louvem copper deposit, Val d'Or, Quebec. Canadian Journal of Earth Sciences, **15**: 1161-1169.

Spry, P.G., and Heimann, A. 2007. Discrimination of Metamorphic and Metasomatic Processes at the Broken Hill Pb-Zn-Ag Deposit, Australia: Rare Earth Element Signatures of Garnet-Rich Rocks. Economic Geology, **102**: 471-494.

Spry, P.G., Peter, J.M., and Slack, J.F., 2000, Meta-exhalites as exploration guides to ore: Reviews in Economic Geology, **11**: 163–201.

Spry, P.G., and Wonder, J.D. 1989. Manganese-rich garnet rocks associated with The Broken Hill Lead-Zinc-Silver Deposit, New South Wales, Australia. Canadian Mineralogist, **27**: 275-292.

Stephens, M.B., Swinden, H.S., and Slack, J.F. 1984. Correlation of massive sulfide deposits in the Appalachian-Caledonian orogen on the basis of paleotectonic setting. Economic Geology, **79**: 1442-1478.

Stevens, B.P.J., and Barron, L.M. 2002. Volcanic textures in the Palaeoproterozoic Hores Gneiss, Broken Hill, Australia. Geological Survey of New South Wales Quarterly Notes, **113**: 1-22.

Stanton, R.L., 2004. Exhalative metasediments - clues to the real nature of regional metamorphic processes. Mineralogy and Petrology, **80**: 111-122.

Stanton, R.L. 1976. Petrochemical studies of ore environment at Broken Hill, New South Wales: 3. Banded iron formation and sulfide orebodies constitutional genetic ties. Inst. Min. Metall. Trans., **B85**: 132-141.

Sun, S-S., and McDonough, W.F. 1989. Chemical and isotopic systematics of oceanic basalts: implications for mantle composition and processes. *In* Magmatism in the Ocean Basins. A.D., Saunders, and M.J., Norry (*eds.*). Geological Society Special Publication, **8**: 313-345.

Taylor, S.R., and McLennan, S.M. 1985. The continental crust: It's composition and evolution. Blackwell, Oxford, pp. 312.

Thompson, P.H., Russell, I., Paul, D., Kerswill, J.A., and Froese, E. 1997. Regional geology and mineral potential of the Winter Lake-Lac de Gras area, central Slave Province, Northwest Territories. Geological Survey of Canada, **Paper 1995-C**, pp. 107-119.

Tivey, M.K. 2007. Generation of Seafloor Hydrothermal Vent Fluids and Associated Mineral Deposits. Oceanography, **20**(1): 50-65.

Tollo, R.P., Corriveau, L., McLelland, J., and Bartholemew, M.J., 2004. Proterozoic evolution of the Grenville orogen in North America: An introduction. *In* Proterozoic Tectonic Evolution of the Grenville Orogen in North America. R.P. Tollo, L., Corriveau, J., McLelland, and M.J., Bartholomew (*eds.*). Geological Society of America Memoir, **197**, pp. 1–18.

Trägårdh, J. 1991. Metamorphism of magnesium-altered felsic volcanic rocks from Bergslagen, central Sweden: A transition from Mg-chlorite to cordierite-rich rocks: Ore Geology Reviews, **6**: 485-497.

Valverde Cardenas, C., Indares, A., and Jenner, J. 2012. Mafic and ultrapotassic rocks from the Canyon domain (central Grenville Province): geochemistry and tectonic implications. Canadian Journal of Earth Sciences, **49**: 412–433.

van Breemen, O., and Corriveau, L. 2005. U-Pb age constraints on arenaceous and volcanic rocks of the Wakeham Group, eastern Grenville Province. Canadian Journal of Earth Sciences, **42**: 1677-1697.

van Gool, J.A.M., Rivers, T., and Calon, T. 2008. Grenville Front zone, Gagnon terrane, south-western Labrador: Configuration of a midcrustal foreland fold-thrust belt. Tectonics, **27**: 1–35.

Willis, I.L., Brown R.E., Stroud, W.J. and Stevens B.P.J. 1983. The Early Proterozoic Willyama Supergroup: stratigraphic subdivision and interpretation of high to low-grade metamorphic rocks in the Broken Hill Block, New South Wales. Journal of Geological Society of Australia, **30**: 195-224.

Winchester, J.A., and Floyd, P.A. 1977. Geochemical discrimination of different magma series and their differentiation products using immobile elements. Chemical Geology, **20**: 325-343.

Zaleski, E., and Peterson, V.L. 1995. Depositional setting and deformation of massive sulphide deposits, iron-formation, and associated alteration in the Manitouwadge Greenstone Belt, Superior Province, Ontario. Economic Geology, **90**: 2244-2261.

APPENDICES

(see spreadsheets A-C)

APPENDIX A: EPMA ANALYSES

EPMA data (discussed in Chapter 4):

a) composition of analyzed standards; and

b) composition of garnet, biotite, spinel, K-feldspar and plagioclase analyzed in the studied rocks.

APPENDIX B: SEM-MLA MAPS

SEM-MLA maps showing the location of spots analyzed by EPMA for garnet, biotite, spinel, K-feldspar and plagioclase.

APPENDIX C: WHOLE-ROCK ANALYSES

Whole-rock analyses (discussed in Chapter 4) of major oxide and minor/trace elements for the 23 samples selected from the studied rocks. Both the raw and corrected values of the datum are included. In addition, the precision of detection limit for fusion ICP (%) and trace element ICP-MS (ppm) selected from the combination package at Actlabs used for analyses is included.

Almandine	
Grossular	

Cations on a basis mol prop i e i Al Ca	
Almandine	
Grossular	

B A A A A A

ide er enta e t	
Biotite	

Cations on a basis mol prop K e	
Biotite	

A A A A A

ide er enta e t	
Chromite	

Cations on a basis mol prop i e n Cr n	
Chromite	

K-feldspar	
Albite	
Anorthite	

Cations on a basis mol prop	***a***	***Ca***	***e***	***i***	***K***	***Al***
K-feldspar						
Albite						
Anorthite						

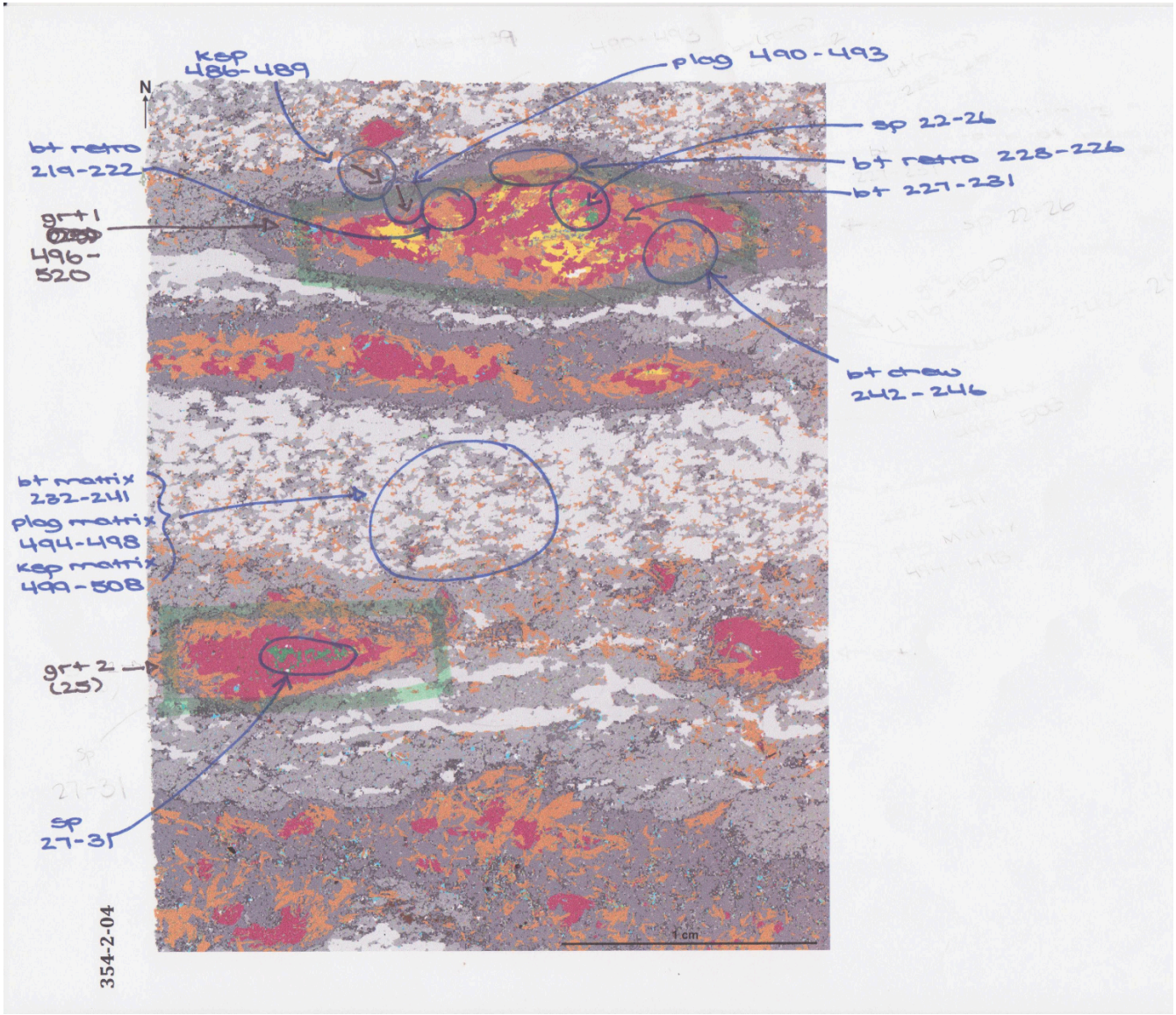
kep 486-489
plag 490-493
sp 22-26
bt retro 228-226
bt 227-231
bt retro 219-222
gr+1 496-520
bt drew 242-246
bt matrix 232-241
plag matrix 494-498
kep matrix 499-508
gr+2 (25)
sp 27-31
N
1 cm
354-2-04

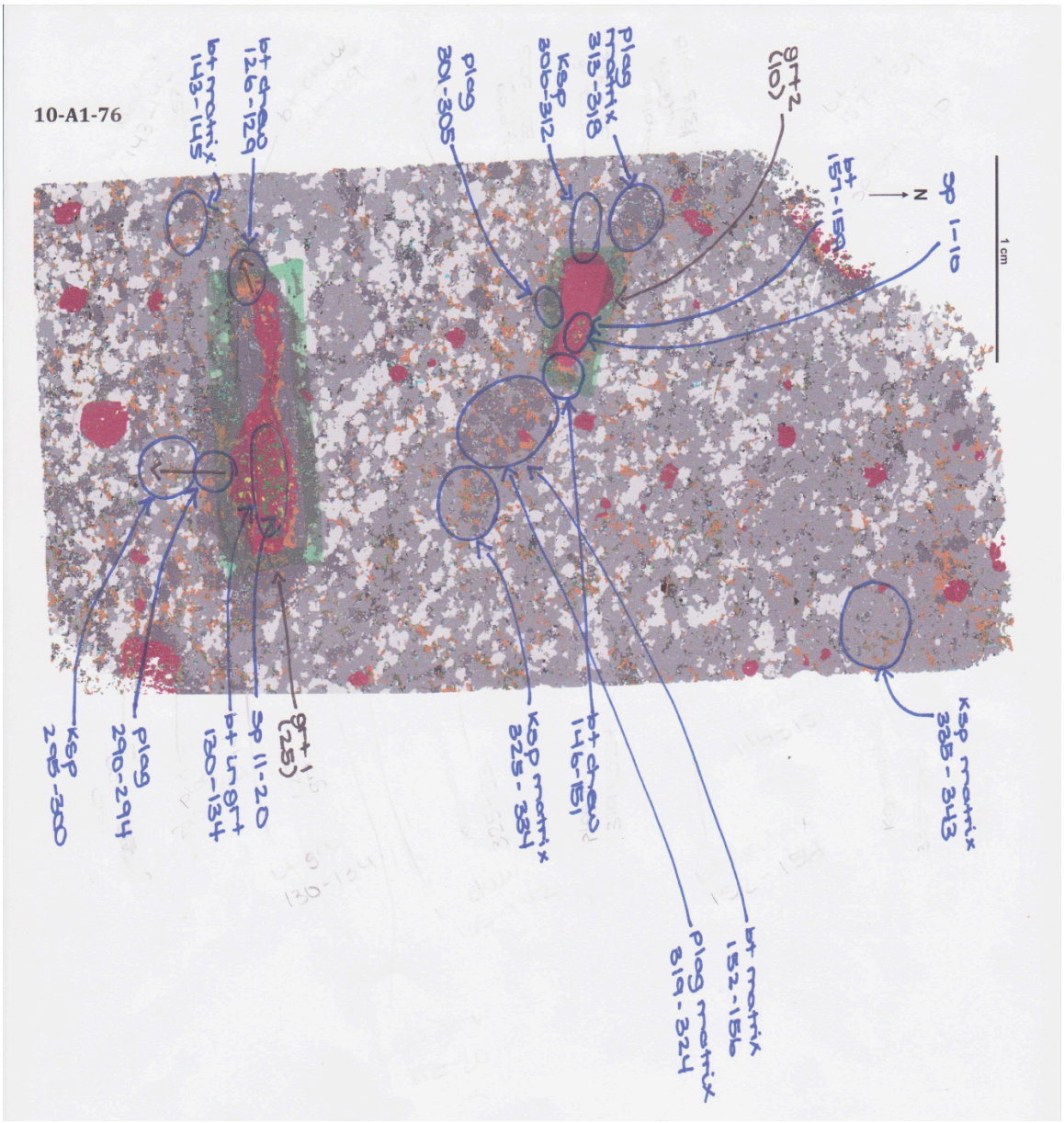
10-A1-76
N
1 cm
sp 1-10
bt 151-158
grt 2 (10)
plag matrix 313-318
ksp 306-312
plag 301-305
bt matrix 143-145
bt phen 126-129
ksp 290-300
plag 290-294
bt matrix 120-134
grt 1 (25)
sp 11-20
ksp matrix 325-343
bt phen 119-151
ksp matrix 825-334
bt matrix 152-156
plag matrix 319-324

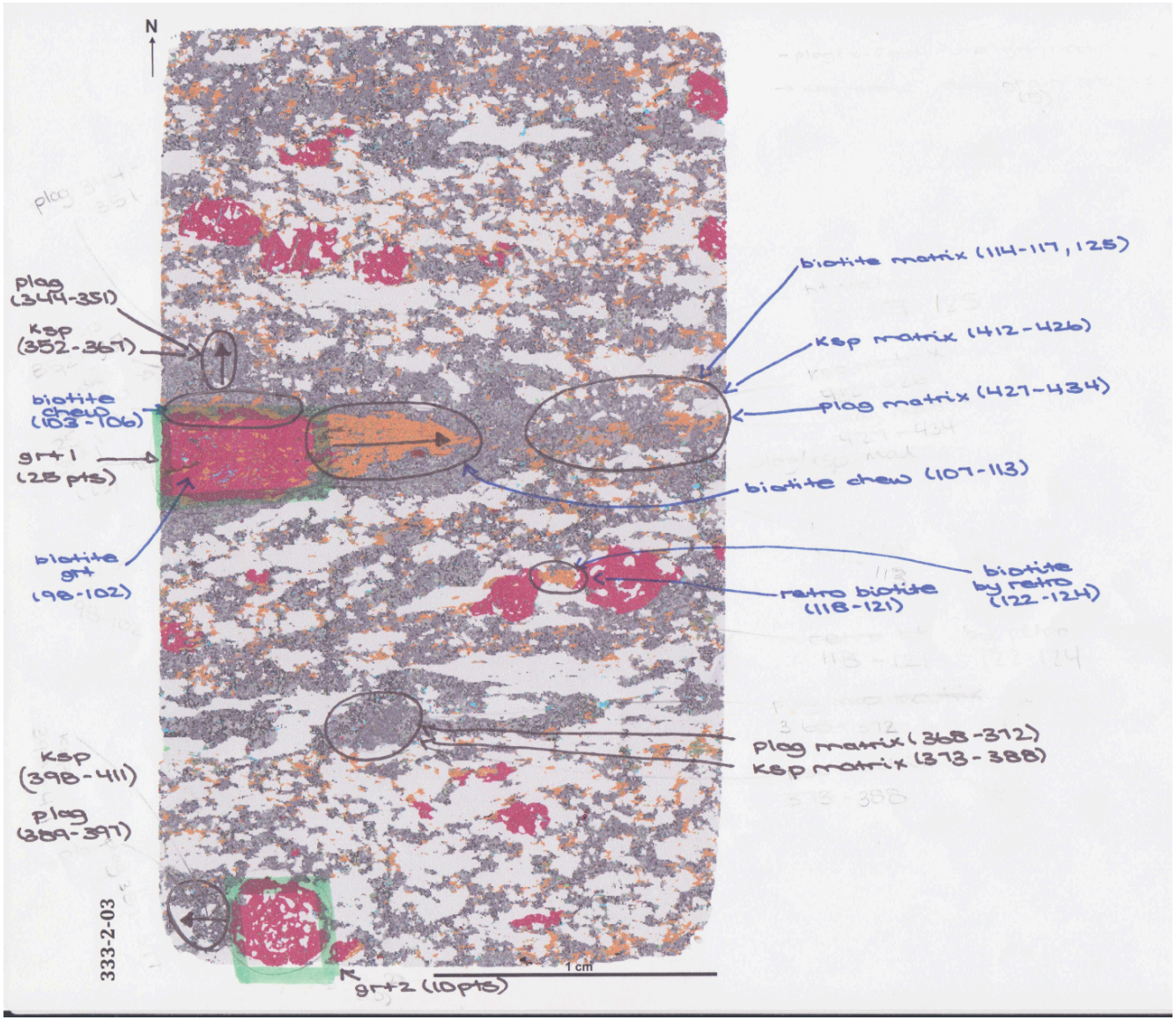
N
plag (344-351)
ksp (352-367)
biotite chew (103-106)
grt 1 (25 pts)
biotite grt (98-102)
ksp (398-411)
plag (389-397)
333-2-03
1 cm
grt 2 (10pts)
biotite matrix (114-117, 125)
ksp matrix (412-426)
plag matrix (427-434)
biotite chew (107-113)
biotite by retro (122-124)
retro biotite (118-121)
plag matrix (368-372)
ksp matrix (373-388)

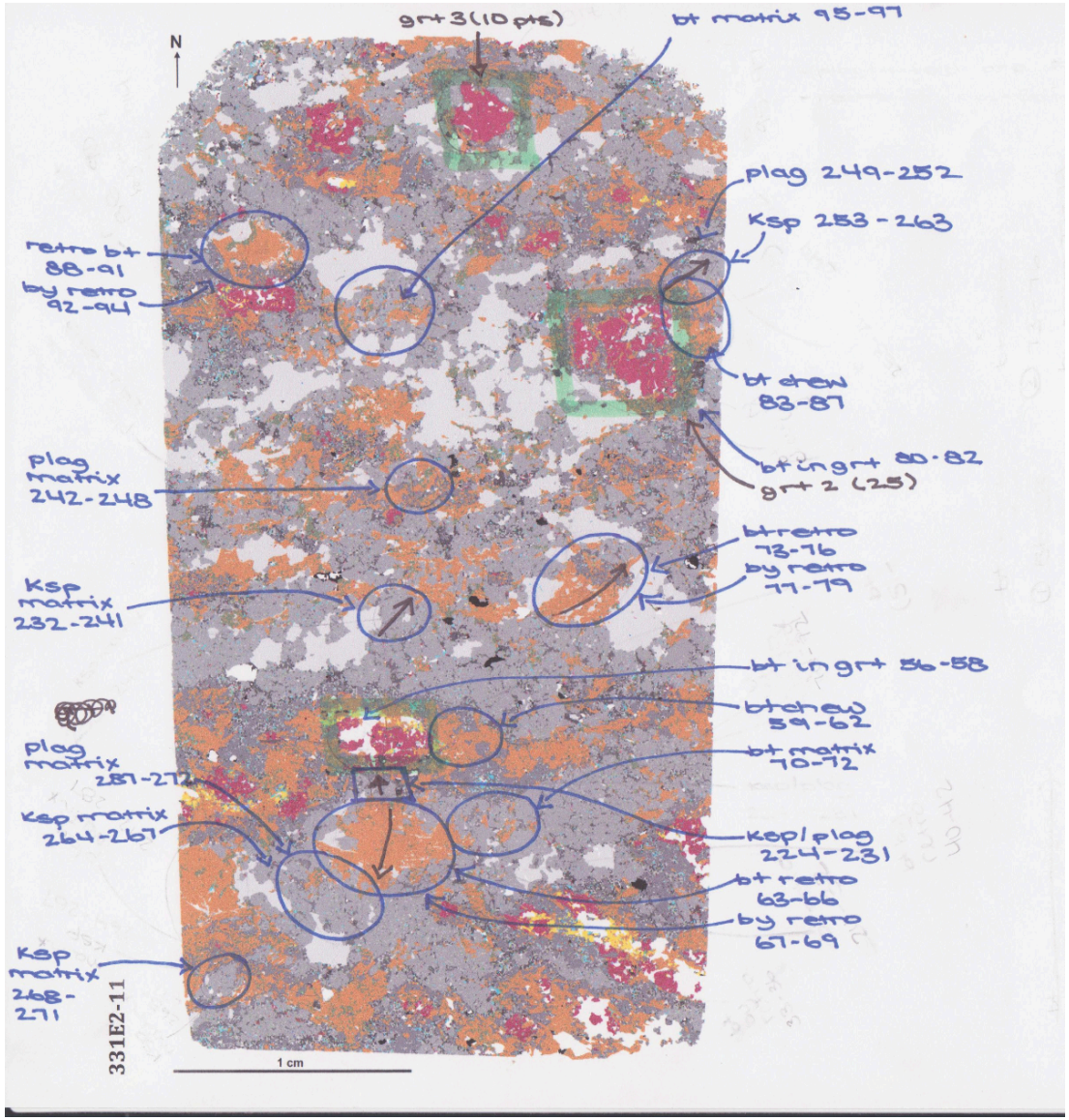
grt 3 (10 pts)
bt matrix 95-97
N
plag 249-252
Ksp 253-263
retro bt 88-91
by retro 92-94
bt drew 83-87
bt in grt 80-82
grt 2 (25)
plag matrix 242-248
bt retro 73-76
by retro 77-79
Ksp matrix 232-241
bt in grt 56-58
bt drew 59-62
plag matrix 281-272
bt matrix 70-72
Ksp matrix 264-267
Ksp/plag 224-231
bt retro 63-66
by retro 67-69
Ksp matrix 268-271
331E2-11
1 cm

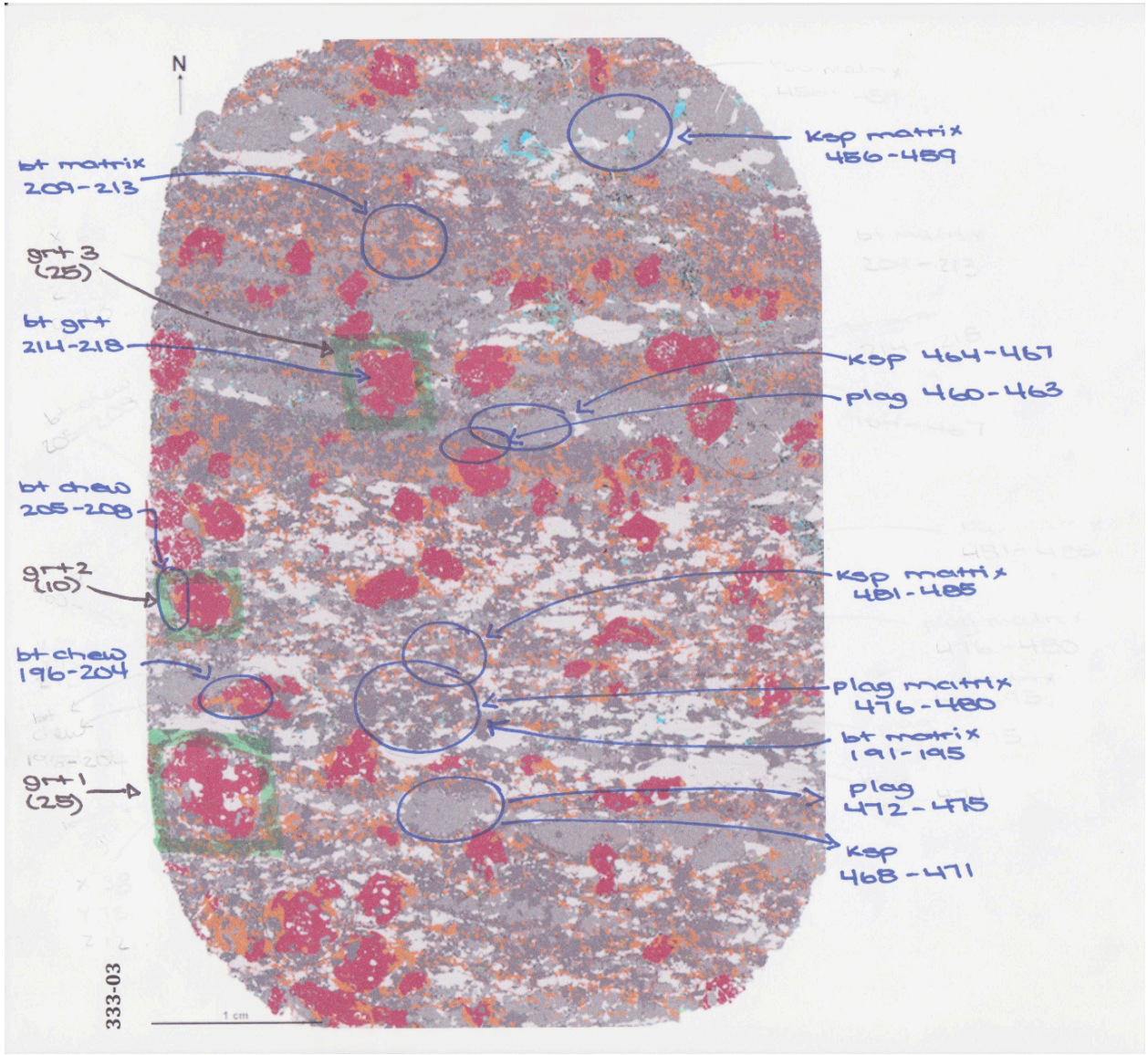
N
bt matrix
209-213
grt 3
(25)
bt grt
214-218
bt chew
205-208
grt 2
(10)
bt chew
196-204
grt 1
(25)
ksp matrix
486-489
ksp 464-467
plag 460-463
ksp matrix
481-485
plag matrix
476-480
bt matrix
191-195
plag
472-475
ksp
468-471
333-03
1 cm

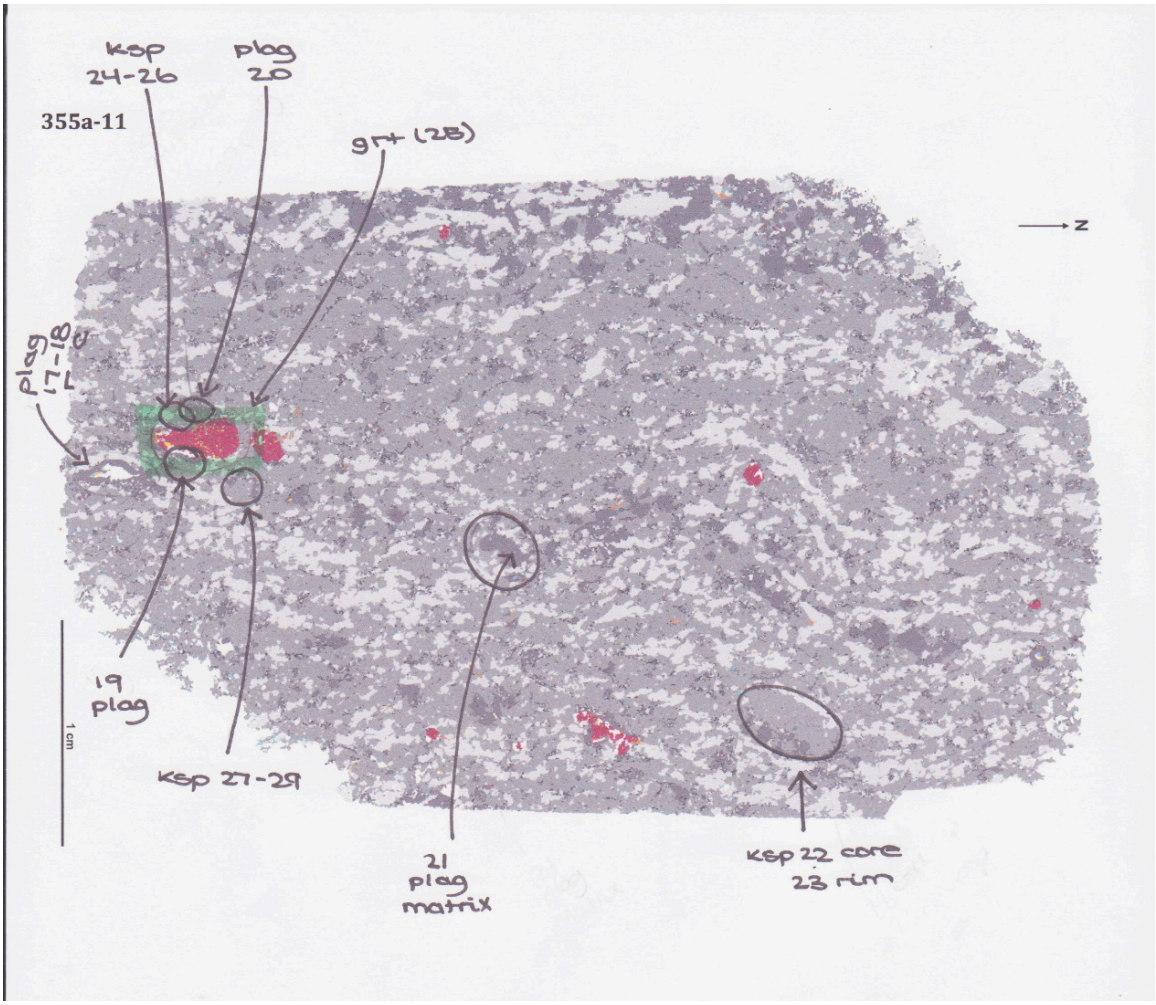
ksp
24-26
plag
20
355a-11
grt (28)
z
plag
17-18
19
plag
1 cm
ksp 27-29
21
plag
matrix
ksp 22 core
23 rim

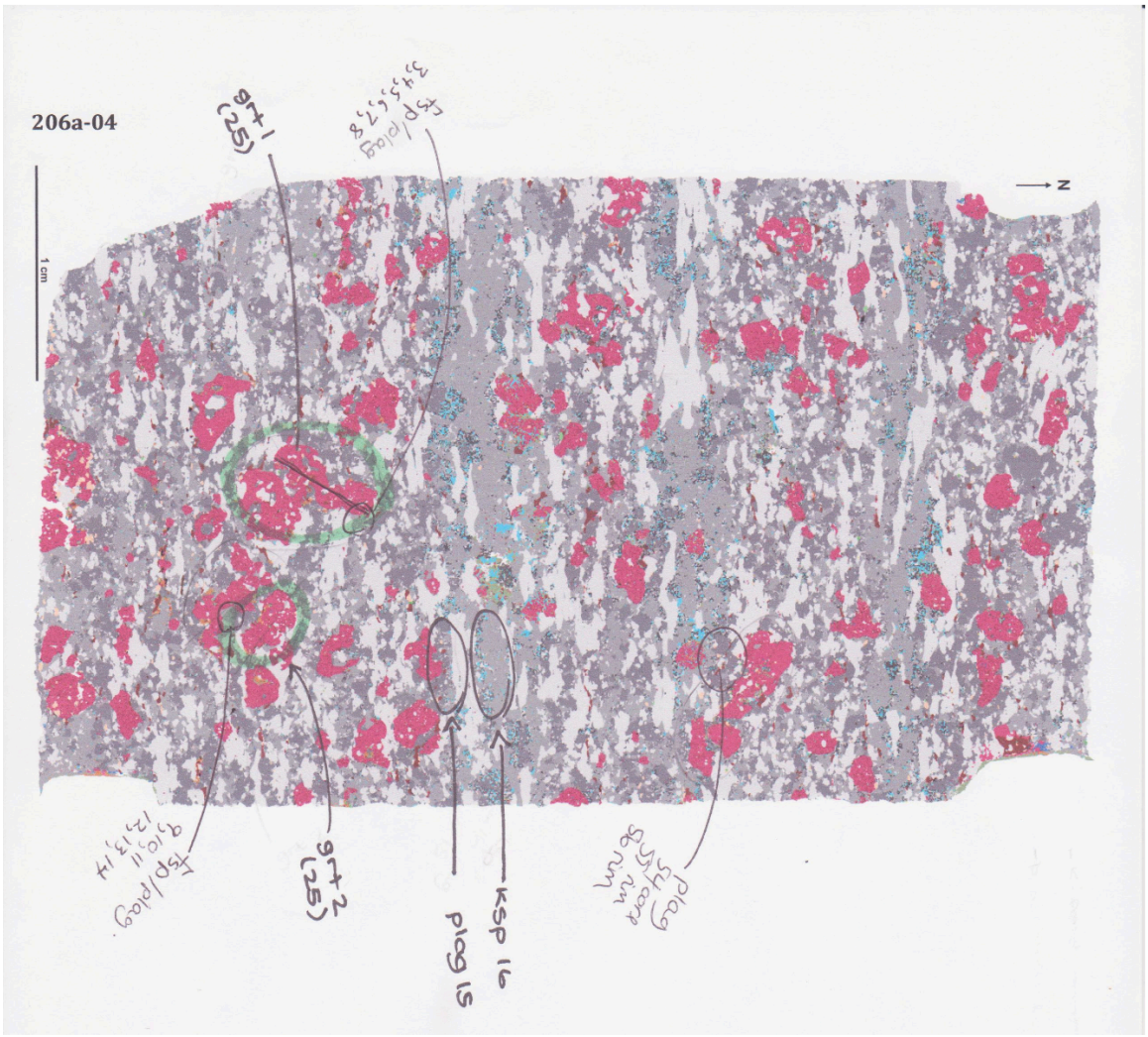
206a-04
1 cm
z
grt 1 (25)
ksp/plag 3,4,5,7,8
ksp/plag 9,10,11 12,13,14
grt 2 (25)
plag 15
ksp 16
plag symplectite

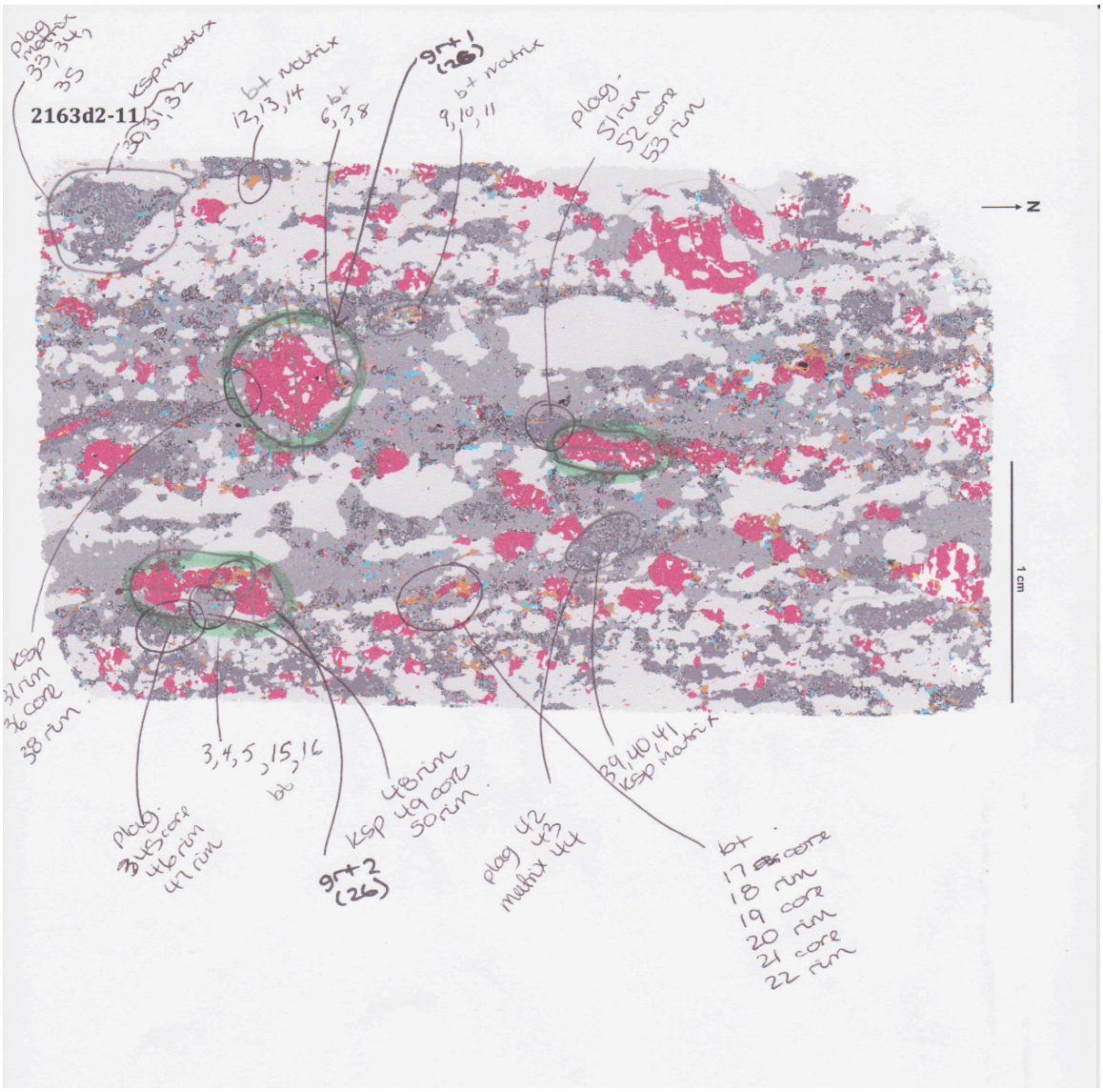
2163d2-11
plag matrix 33, 34, 35
ksp matrix 30, 31, 32
bt matrix 12, 13, 14
bt 6, 7, 8
grt 1 (26)
bt matrix 9, 10, 11
plag. 51 rim 52 core 53 rim
N
1 cm
ksp 37 rim 36 core 38 rim
3, 4, 5, 15, 16 bc
plag. 45 core 46 rim 47 rim
ksp 48 rim 49 core 50 rim
grt 2 (26)
plag 42 43 matrix 44
39, 40, 41 ksp matrix
bt 17 core 18 rim 19 core 20 rim 21 core 22 rim

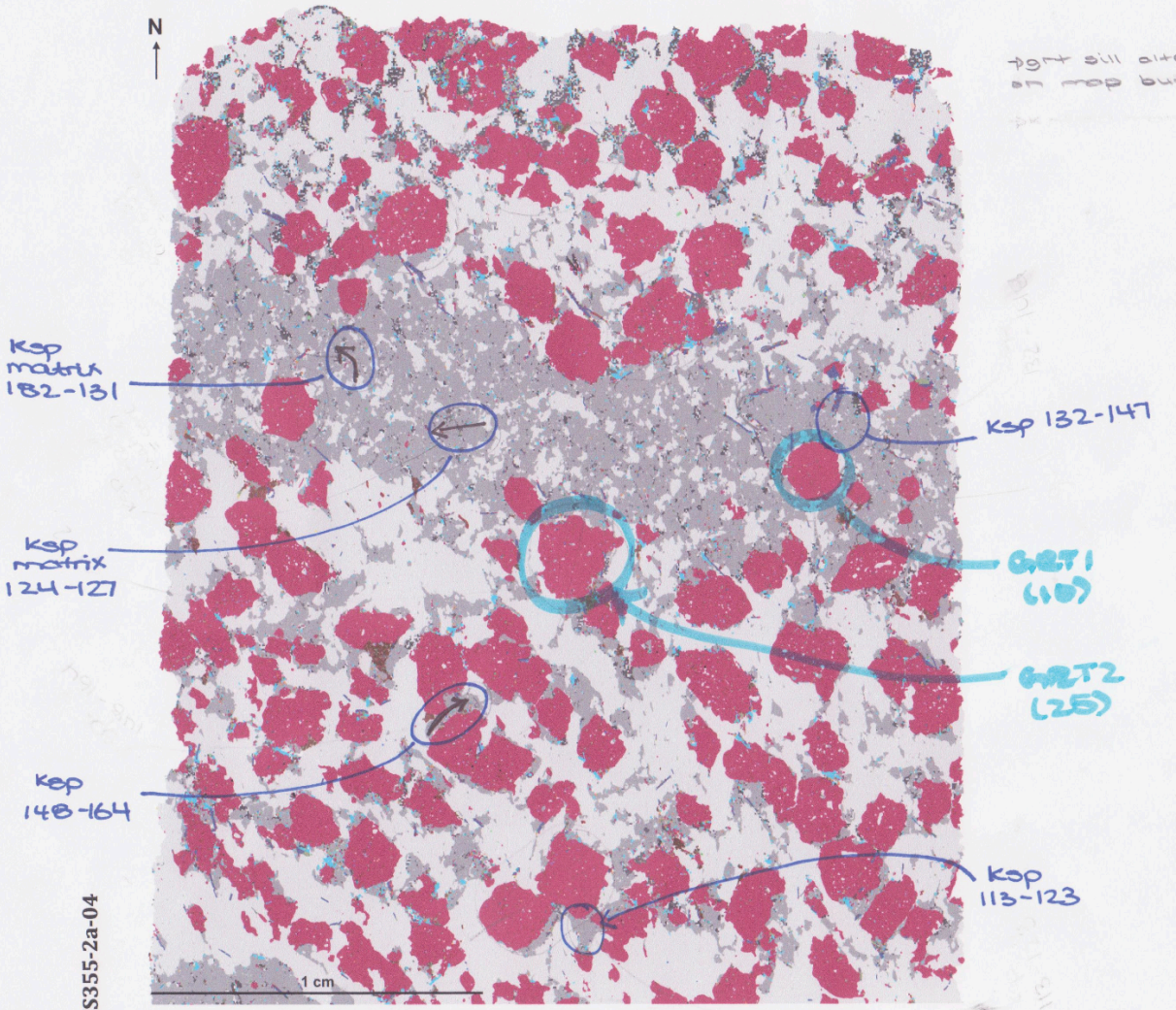

grt sill alteration is not on map but more south

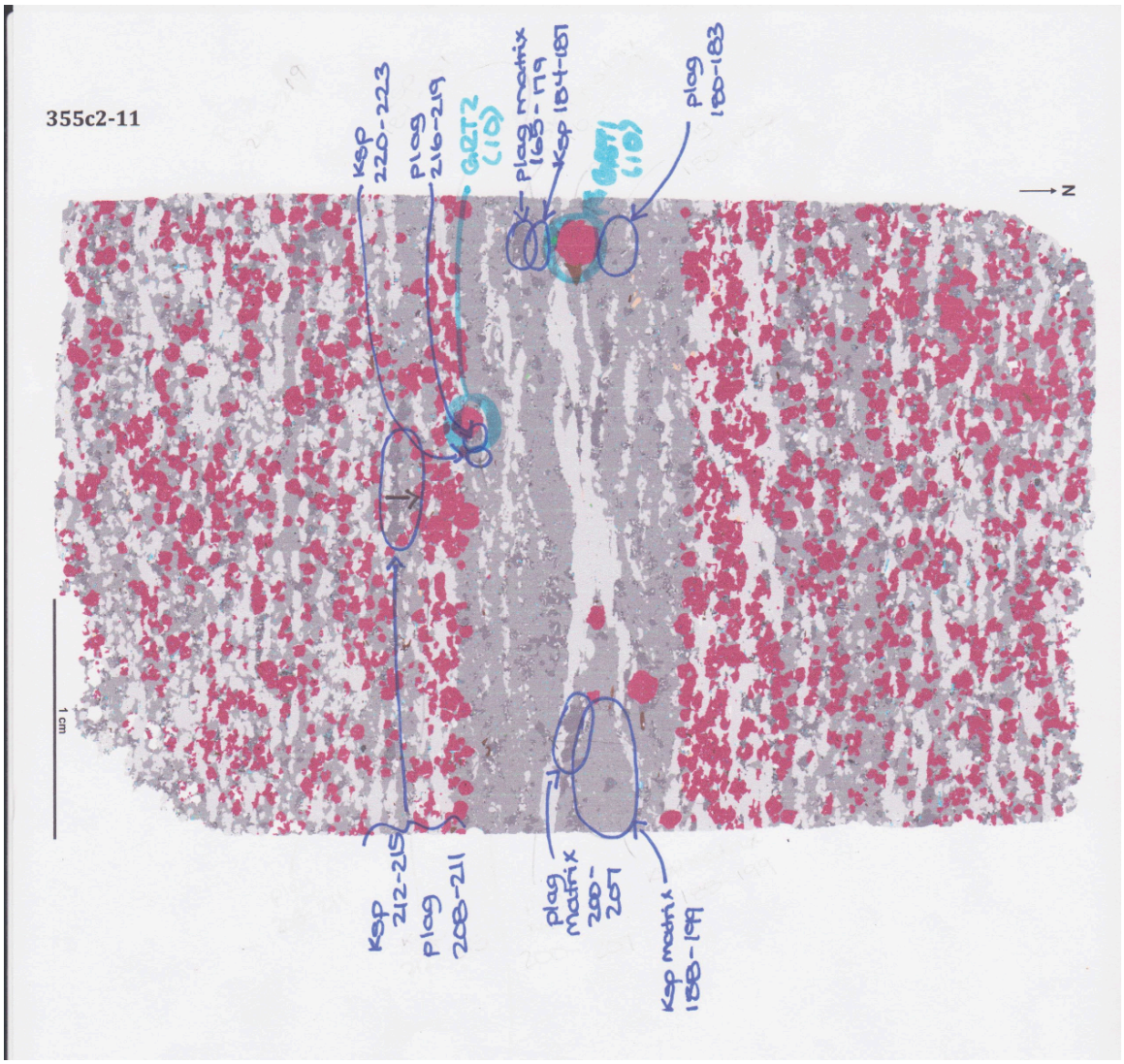
355c2-11
Ksp 220-223
Plag 216-219
QRTZ (10)
Plag matrix 169-179
Ksp 184-187
Plag 180-183
N
1 cm
Ksp 212-215
Plag 208-211
Plag matrix 200-207
Ksp matrix 188-199

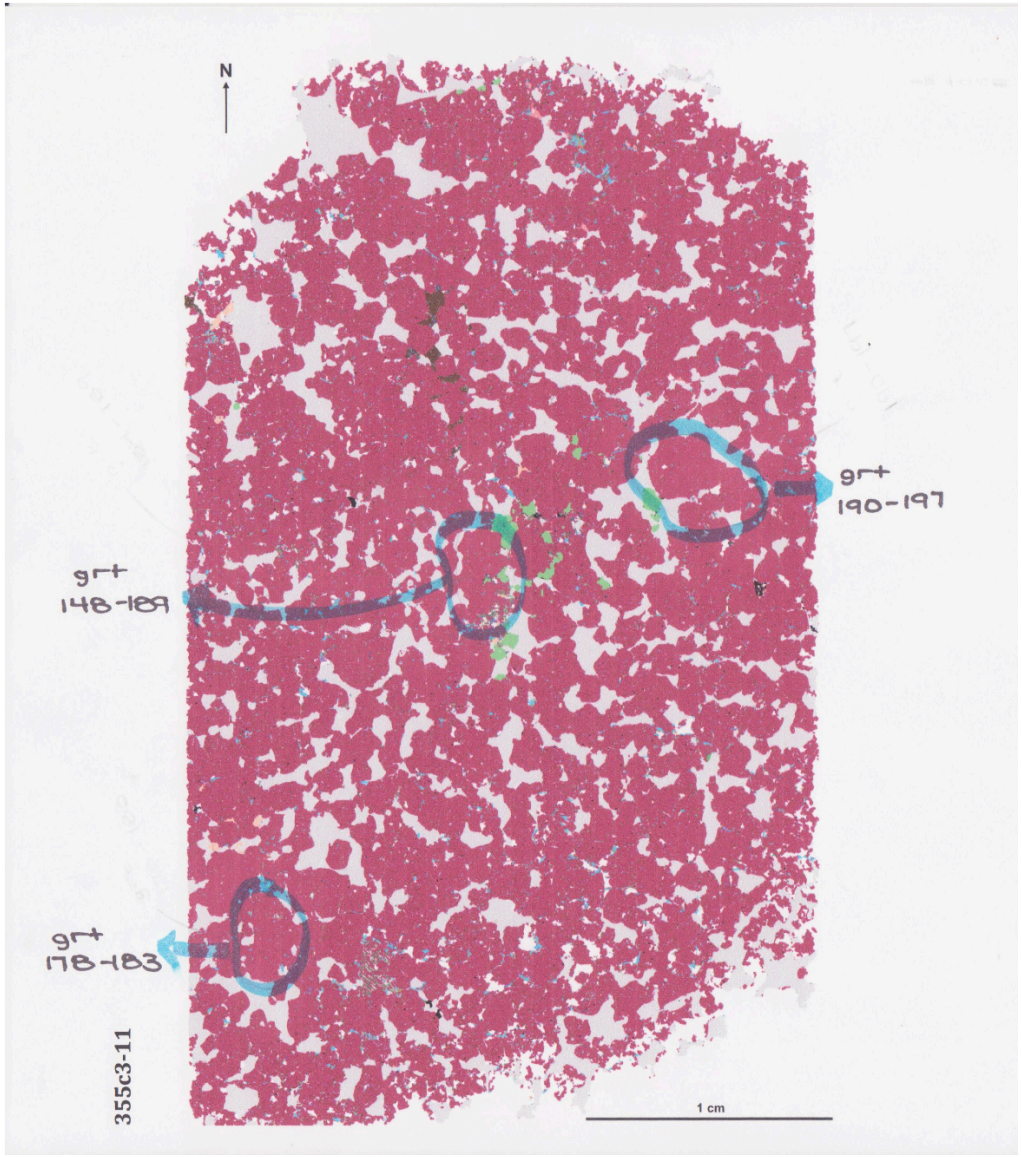
N
grt
190-197
grt
148-169
grt
178-183
355c3-11
1 cm

355cx-11

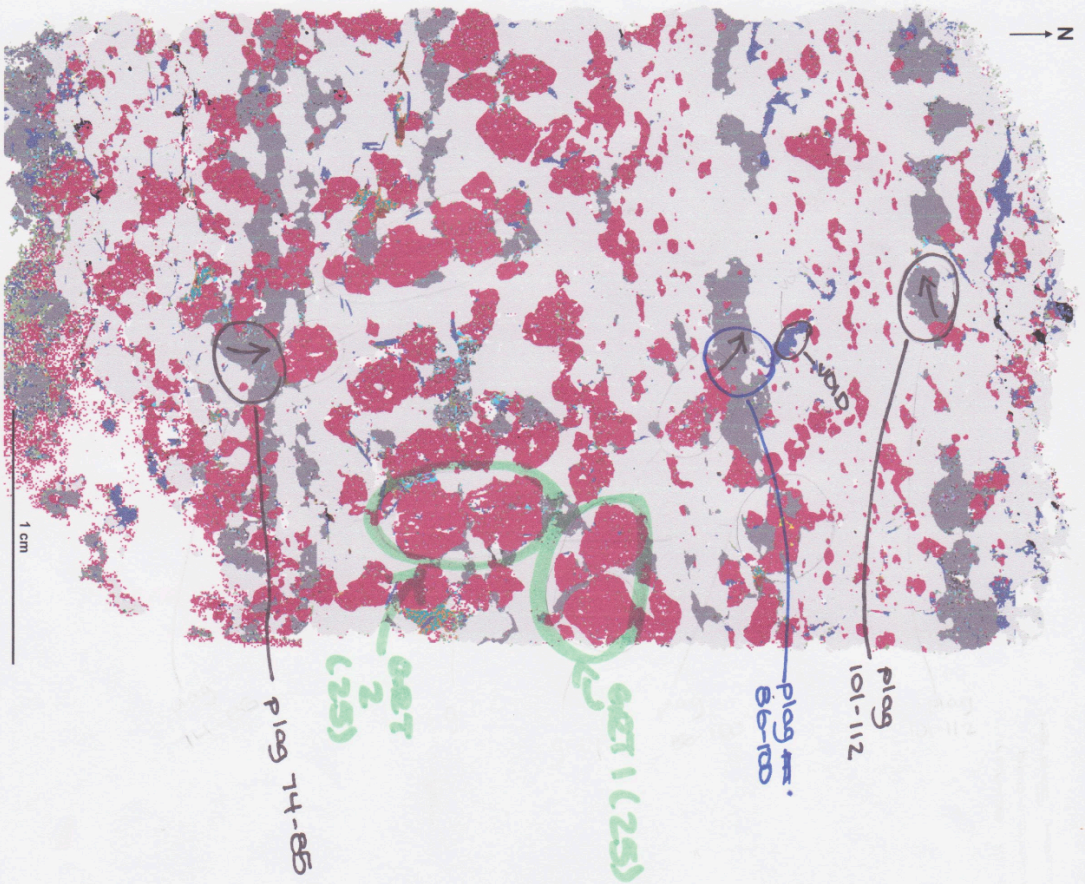
N
1 cm
plag 74-85
SHEET 2 (25)
SHEET 1 (25)
plag 86-88
WOLD
plag 101-112

R

MAJOR OXIDES (wt%):	Aluminous Gneisses				
Sample	331E2-11	333-03	216z-04	361A-11	355A-11
SiO_2	57.03	78.2	69.62	70.74	72.82
TiO_2	0.953	0.185	0.723	0.322	0.029
Al_2O_3	17.74	10.79	13.96	14.7	14.74
Fe_2O_3 (T)	7.96	1.54	6.06	1.82	0.58
MnO	0.07	0.043	0.053	0.021	0.02
MgO	3.24	0.51	2.22	0.62	0.11
CaO	0.78	1.5	1	1.85	1.26
Na_2O	2.85	2.21	2.06	3.09	3.01
K_2O	6.4	3.44	4.25	4.67	5.69
P_2O_5	0.02	< 0.01	0.1	0.04	0.06
LOI	1.29	0.29	0.84	0.31	0.16
To al	98.35	98.71	100.9	98.18	98.47

MINOR/TRACE (ppm):	Aluminous Gneisses				
Sample	331E2-11	333-03	216z-04	361A-11	355A-11
Co	99	119	256	105	97
Cr	150	< 20	90	< 20	< 20
Cu	60	< 10	30	10	< 10
Ni	70	< 20	70	< 20	< 20
Sc	21	6	15	6	2
Be	< 1	< 1	< 1	1	1
V	165	10	110	37	6
Zn	120	< 30	40	< 30	< 30
Ba	1117	1844	639	1288	693
Ga	24	9	18	15	13
Ge	2	< 1	1	1	1
As	< 5	< 5	< 5	< 5	< 5
Ag	1.2	< 0.5	< 0.5	0.5	< 0.5
In	< 0.2	< 0.2	< 0.2	< 0.2	< 0.2
Sn	< 1	< 1	1	< 1	< 1
Sb	< 0.5	< 0.5	< 0.5	< 0.5	< 0.5
Cs	1.3	18.3	1	< 0.5	< 0.5
Rb	177	81	101	103	115
Sr	230	198	76	250	144

Th	10.1	1.1	12.6	17.4	< 0.1
U	1.3	0.3	2.9	1.6	0.2
Zr	290	160	259	192	27
Hf	7.8	3.9	6.4	5	0.9
Nb	14	3	11	10	< 1
Mo	< 2	< 2	< 2	< 2	< 2
Ta	1.8	2	2.5	2.8	1.9
W	213	566	961	472	415
Tl	0.8	0.4	0.6	0.7	0.7
Pb	52	14	10	26	36
Bi	< 0.4	< 0.4	< 0.4	< 0.4	< 0.4
Y	31	26	23	26	11
La	45.4	18.3	39.4	67	10
Ce	75.7	32.7	78	130	17.8
Pr	8	2.95	9.22	14.6	1.96
Nd	28.8	9.9	36	54.5	7.1
Sm	5	1.3	6.6	9.8	1.3
Eu	2.1	1.07	1.33	2.73	1.76
Gd	5.2	1.3	5.2	7.2	0.9
Tb	0.9	0.3	0.8	1	0.2
Dy	5.6	3.1	4.5	4.9	1.4
Ho	1.2	0.9	0.9	0.9	0.4
Er	3.6	3.3	2.5	2.4	1.2
Tm	0.58	0.58	0.38	0.31	0.21
Yb	3.9	4.3	2.5	1.9	1.4
Lu	0.65	0.74	0.4	0.31	0.22

AW WHOLE-ROCK LITHOGEOCHEMICAL ANALYSES

White Gneisses						
355b1-11	355cxB-11	2163d2-11	448-11	RS334a-04	10-A1-87B	10-A1-RHY
72.26	66.44	68.26	75.42	73.42	76.14	73.91
0.63	0.452	0.797	0.101	0.206	0.014	0.184
14.03	18.07	14.39	12.02	13.34	13.85	14.44
3.95	3.83	6.15	1.54	1.37	0.28	1.91
0.079	0.207	0.057	0.033	0.051	0.009	0.055
0.68	0.86	2.31	0.12	0.26	0.06	0.4
1.27	1.65	1.06	0.66	1.14	1.92	1.66
2.49	3.21	2	1.88	3.18	2.85	3.69
4.34	5.63	4.43	6.44	5.21	4.72	3.74
0.14	0.06	0.1	0.11	0.06	0.07	0.05
0.15	0.28	0.87	0.15	0.42	0.22	0.08
100	100.7	100.4	98.46	98.66	100.1	100.1

White Gneisses						
355b1-11	355cxB-11	2163d2-11	448-11	RS334a-04	10-A1-87B	10-A1-RHY
87	85	110	141	543	543	285
< 20	< 20	80	< 20	< 20	< 20	< 20
< 10	< 10	20	< 10	< 10	< 10	< 10
< 20	< 20	50	< 20	< 20	< 20	< 20
9	10	15	3	5	2	5
< 1	1	< 1	< 1	1	1	2
33	39	117	8	10	< 5	15
30	50	40	< 30	< 30	< 30	30
803	1773	687	220	1360	2296	687
15	17	17	14	15	11	16
1	2	1	1	1	< 1	1
< 5	< 5	< 5	< 5	< 5	< 5	< 5
1.6	0.6	< 0.5	< 0.5	< 0.5	< 0.5	< 0.5
< 0.2	< 0.2	< 0.2	< 0.2	< 0.2	< 0.2	< 0.2
< 1	< 1	1	< 1	3	< 1	< 1
< 0.5	< 0.5	< 0.5	< 0.5	2.1	< 0.5	< 0.5
< 0.5	< 0.5	1	0.7	< 0.5	< 0.5	1.1
90	109	103	146	102	71	94
119	291	78	72	248	471	128

33.7	4.9	11.2	1.6	34.5	0.4	14.8
1.4	0.8	2.8	0.3	2.2	0.3	2.4
478	220	238	75	170	52	128
11.6	6.2	6.2	2.3	5.4	1.3	3.4
18	22	11	2	7	2	9
< 2	< 2	< 2	< 2	< 2	< 2	< 2
2.2	2.7	2.3	2.4	0.6	7.5	3.3
395	371	445	603	1700	1160	451
0.6	0.7	0.6	0.9	0.5	0.5	0.5
26	35	8	24	61	38	33
< 0.4	< 0.4	< 0.4	< 0.4	< 0.4	< 0.4	< 0.4
44	32	20	30	48	4	20
151	37	37.7	15.4	80.6	6.3	31.8
319	63.5	77	29.8	154	10	54.6
36.4	6.46	9.07	3.25	15.8	1.02	5.52
131	22.4	34.3	11.7	52.7	3.7	19.2
19.7	4.3	6.2	2.6	8.1	0.7	3.2
1.59	2.79	1.27	0.6	1.2	2.24	0.72
12.1	5	4.6	2.9	5.8	0.6	2.6
1.6	0.9	0.7	0.7	1	< 0.1	0.5
8.2	5.4	3.6	4.9	6.5	0.6	3
1.5	1.1	0.8	0.9	1.6	0.1	0.6
4.4	3.2	2.4	2.3	6	0.5	2
0.65	0.51	0.37	0.3	1.15	0.09	0.33
4.1	3.4	2.7	1.7	8.1	0.7	2.3
0.64	0.57	0.43	0.24	1.24	0.1	0.37

Pink Gneisses						
339b1-11	319-1-11	2161b-11	216e-11	RS305b-04	RS306-1-04	RS309-2-04
77.63	73.26	81.67	71.53	67.54	63.69	60.06
0.146	0.387	0.103	0.536	0.547	0.745	0.414
11.36	11.94	9.69	13.78	14.34	18.46	20.23
1.29	3.76	1.43	3.58	4.99	5.33	3.49
0.023	0.051	0.014	0.089	0.133	0.086	0.057
0.13	0.2	0.09	0.76	0.26	1.68	1.45
0.54	1.07	0.45	1.65	2.15	1.16	4.67
3.16	2.5	1.78	3.1	3.32	3.03	6.21
4.46	4.79	4.74	4.7	5.37	4.37	1.94
0.01	0.05	0.01	0.16	0.15	0.13	0.05
0.16	0.25	0.21	0.22	0.28	-0.04	0.79
98.92	98.27	100.2	100.1	99.08	98.66	99.38

Pink Gneisses						
339b1-11	319-1-11	2161b-11	216e-11	RS305b-04	RS306-1-04	RS309-2-04
122	91	< 20	79	552	548	139
< 20	< 20	< 20	< 20	< 20	90	< 20
< 10	< 10	< 10	< 10	10	< 10	< 10
< 20	< 20	< 20	< 20	< 20	< 20	< 20
2	7	< 1	10	11	17	23
2	1	< 1	3	2	< 1	2
8	12	11	45	7	91	44
< 30	70	< 30	60	80	60	60
191	1477	1335	1195	1880	1400	959
13	18	10	16	26	23	26
1	2	1	1	2	1	1
< 5	< 5	< 5	< 5	< 5	11	< 5
< 0.5	1.4	0.8	0.6	< 0.5	< 0.5	1.6
< 0.2	< 0.2	< 0.2	< 0.2	< 0.2	< 0.2	< 0.2
1	< 1	< 1	2	2	< 1	2
< 0.5	< 0.5	< 0.5	< 0.5	1.4	< 0.5	< 0.5
< 0.5	< 0.5	< 0.5	1.5	< 0.5	< 0.5	< 0.5
125	106	89	147	91	140	21
29	123	304	203	140	268	1263

20.8	9.5	16.7	16.7	9	16.8	0.7
1.6	0.6	1.7	1.7	0.6	1.8	0.3
141	453	248	232	914	240	463
4.8	12	6	6	21.7	7.1	9.8
13	11	1	16	40	18	6
< 2	< 2	< 2	< 2	< 2	< 2	< 2
2.7	1.6	1.8	1.8	1.9	1.4	0.2
541	410	333	333	1560	1670	398
0.6	0.6	0.7	0.7	0.4	0.5	< 0.1
16	20	23	23	36	18	17
< 0.4	< 0.4	< 0.4	< 0.4	< 0.4	< 0.4	< 0.4
27	45	8	44	120	44	24
44.7	89.3	30.1	58.8	106	61.9	27.4
93.8	187	64.4	122	221	126	57.4
10.4	21.6	7.16	13.6	26.3	14.4	8.21
37.2	83	26.8	49.3	103	53.3	36.1
6.8	14.9	5.6	8.9	20.4	9.3	7.9
0.31	2.73	0.68	1.39	4.37	1.92	2.32
5	10.9	4	6.8	20.3	8.2	6.2
0.8	1.5	0.5	1.1	3.8	1.3	0.9
4.4	8.5	6.6	6.6	22.1	7.5	5
0.9	1.8	1.5	1.5	4.5	1.5	0.9
3.1	5.6	4.8	4.8	13.7	4.6	2.5
0.55	0.87	0.83	0.83	2.11	0.75	0.36
3.9	5.7	6.1	6.1	13.6	5	2.2
0.64	0.97	1.01	1.01	2.04	0.75	0.3

Garnetites			
355cxA-11	355cxC-11	355c2-11	355c3-11
64.74	77.07	61.93	47.86
0.347	0.269	0.546	0.341
13.46	11.32	15.53	17.2
14.56	5.42	10.85	27.07
0.8	0.291	2.47	3.152
3.26	1.22	2.42	2.96
1.22	1.63	0.97	3.36
1.05	2.01	1.22	0.02
0.63	0.37	4.03	0.06
0.05	0.05	0.15	0.1
-0.03	0.09	-0.45	-1.49
100.1	99.73	99.66	100.6

Garnetites			
355cxA-11	355cxC-11	355c2-11	355c3-11
191	142	164	199
< 20	< 20	20	< 20
10	< 10	< 10	< 10
< 20	< 20	< 20	< 20
33	8	16	84
< 1	1	< 1	< 1
91	34	66	66
130	50	110	140
183	71	1214	39
10	12	15	16
5	34	6	
< 5	< 5	< 5	< 5
< 0.5	< 0.5	< 0.5	< 0.5
< 0.2	< 0.2	< 0.2	< 0.2
< 1	< 1	< 1	< 1
< 0.5	< 0.5	< 0.5	< 0.5
< 0.5	< 0.5	< 0.5	< 0.5
12	6	98	2
62	107	201	< 2

8.2	18.5	11.2	32.9
1.1	1.6	1.3	2.7
166	120	183	53
4.4	3.2	4.8	1.7
15	9	11	12
2	< 2	< 2	< 2
3	2.8	2.3	2.6
846	640	612	794
< 0.1	< 0.1	0.7	< 0.1
6	7	28	< 5
< 0.4	< 0.4	< 0.4	< 0.4
108	34	39	414
37.8	74.7	52.4	94.5
77.5	159	114	188
9.09	18.7	12.7	21.7
35.9	71	49.1	82.2
10.1	12.5	9.5	19.3
0.81	1.06	1.68	0.92
15.5	8.6	7.6	27.3
2.8	1.2	1.2	6.5
18.2	5.9	6.7	54.6
3.6	1.1	1.4	13.8
10.5	3	4.3	42
1.66	0.43	0.66	6.36
10.9	2.8	4.6	40.3
1.68	0.47	0.75	6.09